
Electronic Thesis and Dissertation Repository

8-12-2016 12:00 AM

Magnetic Resonance Imaging of Breast Cancer Brain Metastasis Progression and Responses to Radiotherapy

Donna H. Murrell
The University of Western Ontario

Supervisor
Dr. Paula Foster
The University of Western Ontario

Graduate Program in Medical Biophysics
A thesis submitted in partial fulfillment of the requirements for the degree in Doctor of Philosophy
© Donna H. Murrell 2016

Follow this and additional works at: <https://ir.lib.uwo.ca/etd>



Part of the [Medical Biophysics Commons](#)

Recommended Citation

Murrell, Donna H., "Magnetic Resonance Imaging of Breast Cancer Brain Metastasis Progression and Responses to Radiotherapy" (2016). *Electronic Thesis and Dissertation Repository*. 3961.
<https://ir.lib.uwo.ca/etd/3961>

This Dissertation/Thesis is brought to you for free and open access by Scholarship@Western. It has been accepted for inclusion in Electronic Thesis and Dissertation Repository by an authorized administrator of Scholarship@Western. For more information, please contact wlsadmin@uwo.ca.

Abstract

Introduction: The incidence of brain metastasis due to breast cancer is increasing and prognosis is poor. Treatment is challenging for this disease because systemic therapy has limited efficacy due to the presence of the blood-brain barrier. In addition, it is thought that disseminated dormant cancer cells persist in metastatic organs and may evade treatment, thereby facilitating a mechanism for later recurrence. **Methods:** In this thesis, we use contrast-enhanced MRI and high resolution anatomical MRI to characterize blood-brain barrier integrity associated with the development of metastases in the mouse brain due to HER2+ breast cancer in the SUM-190-BR3, JIMT-1-BR3, and MDA-MB-231-BR-HER2 experimental models. We further use these imaging techniques along with novel micro-irradiation technology to investigate the impact of whole brain radiotherapy on the growth and blood-brain barrier permeability of brain metastases in the MDA-MB-231-BR-HER2 model. Finally, we employed MRI cell tracking in this model to study the fate of proliferative and non-proliferative cancer cells after early radiotherapy. Histology and immunohistochemistry was performed on brain sections corresponding to MRI to validate and further investigate radiological findings. **Results:** Herein, we show substantial heterogeneity in tumor permeability across three models of brain metastasis due to HER2+ breast cancer. We also demonstrate that whole brain radiotherapy following diagnosis of brain metastasis in mice can mitigate, but not eliminate, tumor growth in the MDA-MB-231-BR-HER2 model. Furthermore, radiotherapy did not impact blood-brain barrier permeability associated with metastases. In comparison, early WBRT was used successfully in mice as a preventative treatment against brain metastatic growth. Still, cellular MRI revealed the persistence of non-proliferative cancer cells in the brain regardless of treatment time point or efficacy against metastasis. **Conclusions:** Consideration of tumor permeability in brain metastasis models is important when investigating novel therapeutics as blood-brain barrier integrity varies substantially across models of the same disease. Radiotherapy did not increase tumor permeability; however, other strategies should be investigated. Whole brain radiotherapy is effective as a

preventative treatment against brain metastasis, but is not curative when delivered after MRI-detectable tumors have developed. The persistence of iron-retaining non-proliferative cancer cells after prophylactic radiotherapy suggests these dormant cells may be able to evade treatment and later could contribute to cancer recurrence.

Keywords

MRI, breast cancer, brain metastasis, tumor permeability, dormancy, radiotherapy, cell tracking, micron-size particles of iron oxide (MPIO), bSSFP, gadolinium

Co-Authorship Statement

Chapter 1 contains material from 1 previously published paper, 1 paper under review, and 2 book chapters in press. The first paper is DH Murrell, PJ Foster, and AF Chambers (2014) *Brain metastases from breast cancer: lessons from experimental magnetic resonance imaging studies and clinical implications* Journal of Molecular Medicine 92(1):5-12 and is included with permission of Springer. DHM performed the literature review and wrote the majority of manuscript. PJF and AFC also contributed to writing and editing the manuscript. Chelsey Gareau designed Figure 1 for this paper. The second paper is AV Makela*, DH Murrell*, KM Parkins, J Kara, JM Gaudet, and PJ Foster (2016) *Cellular Imaging with MRI* under review at Topics in Magnetic Resonance Imaging. For this paper, AVM, DHM, and PJF wrote the majority of the manuscript. KMP, JK, and JMG also assisted with manuscript preparation. The first book chapter is DH Murrell, F Perera, AF Chambers, and PJ Foster, *Brain metastasis: basic biology, clinical management, and insight from experimental model systems* Introduction to Cancer Research, 1st edition edited by Aamir Ahmad, Elsevier, in press June 24, 2016. DHM wrote this chapter and FP, AFC, and PJF assisted with editing. Chelsey Gareau created Figure 2 for this chapter. The second book chapter is M Bazalova-Carter, DH Murrell, K Parkins, J Ronald, PJ Foster, E Graves, P Granton, and E Wong. *Small Animal Radiotherapy and Imaging* Advances in Medical Physics, edited by Shiva Das and Jacob Van Dyk, Medical Physics Publishing, in press March 17, 2016. DHM and PJF wrote a subsection on Magnetic Resonance Imaging. MBC, KP, JR, EG, PG were authors of additional subsections. EW edited and prepared the chapter.

Chapter 2 is reprinted from: DH Murrell, AM Hamilton, CL Mallett, R van Gorkum, AF Chambers, and PJ Foster (2015) *Understanding heterogeneity and permeability of brain metastases in murine models of HER2-positive breast cancer through magnetic resonance imaging: implications for detection and therapy* Translational Oncology 8(3):176-184. DHM contributed to experimental design, data collection and analysis, and drafted the manuscript. AMH performed most of the histology and

immunohistochemistry. CLM contributed to image acquisition. RvG assisted with data collection and analysis. AFC and PJF contributed to experimental design and drafting the manuscript.

Chapter 3 is reprinted from: DH Murrell, N Zarghami, MD Jensen, AF Chambers, E Wong, and PJ Foster (2016) *Evaluating changes to blood-brain barrier integrity in brain metastasis over time and after radiation treatment* Translational Oncology 9(3): 219-227. DHM participated in study design, performed the experiments and data analysis, and wrote the manuscript. NZ carried out the γ -H2AX staining and participated in animal irradiation. MDJ carried out the dosimetry and participated in animal irradiation. AFC, EW, and PJF contributed to experimental design and manuscript preparation.

Chapter 4 has been submitted and is under review at Magnetic Resonance in Medicine: DH Murrell, N Zarghami, MD Jensen, F Dickson, AF Chambers, E Wong, and PJ Foster. *MRI surveillance of cancer cell fate in a brain metastasis model after early radiotherapy*. DHM carried out the experiments and data analysis, participated in study design, and drafted the manuscript. NZ and MDJ participated in animal irradiation. FD participated in signal void quantification. AFC, EW, and PJF contributed to experimental design and writing the manuscript.

Acknowledgments

I have been very fortunate to study in the Department of Medical Biophysics at Western University and develop as a young researcher in the Imaging Laboratories at Robarts Research Institute. I have so many thank yous to extend to the people who offered support and influenced my thinking over the past four years.

First, I am very thankful to my supervisor, Dr. Paula Foster, for taking a chance on me four years ago and providing me with so many opportunities for success. Your passion for research is contagious and I loved every moment I spent in the lab. Thank you for taking me around the world to present our findings – from Salt Lake City, to Savannah, Milan, Austin, and Singapore – and for helping me to build relationships with the scientists in our field. I consider myself extremely lucky to have had the opportunity to work and learn in your lab. My personal growth as a researcher has been highly influenced by your incredible mentorship. Thank you Paula.

I would like to express my sincere appreciation to the members of my advisory committee, Drs. Ann Chambers and Eugene Wong. Thank you for your genuine interest in these experiments, for taking the time to provide thoughtful feedback, and for providing me with special opportunities to write review papers and book chapters. I am so grateful for your involvement and support through my PhD.

I would like to thank Dr. Michael Jensen and Niloufar Zarghami in the Wong lab for their contributions to the radiotherapy aspects of this project. I appreciate your willingness to accommodate difficult experiment schedules and for lending your expertise to these projects. I would also like to thank Trevor Szekeres, and Drs. Trevor Wade and Paco Martinez, for their technical support at the 3T and for answering all of my questions about gradient inserts and pulse sequences. Thank you to the grad students in Medical Biophysics for being excellent friends and colleagues. I especially want to thank Dr. Damien Pike, as well as Tom Hrinivich and Justin Peterson who have been on this

journey with me since undergrad, for chatting physics with me and for the great memories over the years.

Thank you to Drs. Rob Stodilka and Jerry Battista for your guidance in the CAMPEP Program. I owe an especially big thank you to Dr. Jerry Battista for career advice and taking the time to prepare me for residency interviews. Thank you to Dr. Savita Dhanvantari for organizing the Molecular Imaging Group and stimulating interesting discussion at our meetings, which I looked forward to every month. I am grateful to Dr. Grace Parraga for her leadership during my position as a graduate teaching assistant and for support in her role as Graduate Chair. I would also like to thank Wendy Hough for organizing the administrative side of my graduate career and for taking care of me over the past nine years as a student in MBP.

A tremendous thank you is owed to my fellow Foster lab members, who have become my lab family over the years. It was a pleasure staying “up all night to get data” with you. Thank you to Dr. Amanda Hamilton for training me in most aspects of my project and helping me to hit the ground running from the very start. I really appreciate your expertise and willingness to share it with me. Thank you to Dr. Christiane Mallett for helping me to overcome my fear of mice; I certainly wouldn’t have been able to complete this project without your extreme patience and kindness in my first weeks. I would like to thank Yuhua Chen and Carmen Simedrea for their help with cell culture, immunohistochemistry, and intracardiac injections. I appreciate insight and constant support from Dr. Emie Ribot, Dr. Vas Economopoulos, and Dr. Matt Fox. Thank you to Chelsey Gareau for her artistic talent and creating amazing figures for presentations and publications. Thank you to Ashley Makela, Katie Parkins, and Jenna Kara for all the discussions at lab meeting, chats in the bullpen, and drinks at Grad Club. To (soon to be Dr.) Jeff Gaudet: thank you for setting an incredible pace and running beside me since day 0. I’m not sure what grad school would have looked like without you by my side. I am so lucky to have had you to learn from, argue with, and share in all the frustrating and exciting moments of this degree. Thank you Foster lab for celebrating this achievement with me; it has been an honour to work with all of you.

A special thank you to my family for fostering my curiosity and providing endless support through my PhD journey. Thank you Dad for teaching me healthy skepticism and always guiding me toward logical conclusions; these have perhaps been my greatest strengths throughout my PhD. Thank you Mom for your constant encouragement and reassurance at exactly the times when I needed it. Thank you Emily for sharing this grad school journey with me and for teaching me more about tyrosine isomers than I ever thought I would want to know! Thank you Nicole and Andrew for celebrating the small successes with me along the way. Thank you Brad for being a wonderful partner in this life of ours, for often carrying more than your fair share during experiments and thesis preparation, and for cheering me on the whole way. I hope I have made all of you proud.

Finally, I appreciate the financial support that was generously given to me throughout my graduate career from the Canadian Breast Cancer Foundation, the Translational Breast Cancer Research Unit at the London Regional Cancer Program, CIHR Strategic Training Program in Cancer Research and Technology Transfer, and the Schulich School of Medicine and Dentistry.

Table of Contents

Abstract.....	i
Co-Authorship Statement.....	iii
Acknowledgments.....	v
Table of Contents.....	viii
List of Tables.....	xii
List of Figures.....	xiii
List of Appendices.....	xv
List of Abbreviations.....	xvi
Chapter 1.....	1
1 Introduction.....	1
1.1 Motivation and Overview.....	1
1.2 Metastatic Breast Cancer.....	3
1.2.1 Brain Metastasis.....	4
1.2.2 Metastatic Colonization.....	4
1.2.3 The Unique Brain Microenvironment.....	7
1.2.4 Dormancy.....	8
1.2.5 Experimental Models for Breast Cancer Brain Metastasis.....	9
1.3 Magnetic Resonance Imaging in Oncology.....	13
1.3.1 Generating Image Contrast.....	14
1.3.2 Relevant Pulse Sequences.....	17
1.3.3 Contrast Agents.....	18
1.3.4 Neuroimaging in Neuro-Oncology.....	19

1.3.5	Pre-clinical Imaging of Blood-Brain Barrier Integrity	24
1.3.6	Cellular MRI	26
1.4	Treatment for Brain Metastasis.....	31
1.4.1	Oligometastatic Disease (1 – 3 metastases).....	33
1.4.2	Multiple Metastatic Lesions (>3 metastases).....	34
1.4.3	Preventative Treatment.....	34
1.5	Purpose of Thesis.....	34
1.5.1	Hypotheses.....	35
1.6	References.....	37
Chapter 2	52
2	Understanding Heterogeneity and Permeability of Brain Metastases in Murine Models of HER2-positive Breast Cancer through Magnetic Resonance Imaging: Implications for Detection and Therapy	52
2.1	Introduction.....	53
2.2	Methods.....	55
2.2.1	Cell Culture.....	55
2.2.2	Cell Labeling.....	55
2.2.3	Animal Preparation.....	56
2.2.4	Experimental Endpoint	56
2.2.5	Magnetic Resonance Imaging.....	57
2.2.6	Histology and Immunohistochemistry	57
2.2.7	Data Analysis	58
2.3	Results.....	59
2.4	Discussion.....	72
2.5	References.....	76

Chapter 3.....	82
3 Evaluating changes to blood-brain barrier integrity in brain metastasis over time and after radiation treatment	82
3.1 Introduction.....	82
3.2 Methods.....	84
3.2.1 Cell Culture.....	84
3.2.2 Animal Preparation	85
3.2.3 Radiotherapy	85
3.2.4 Magnetic Resonance Imaging.....	86
3.2.5 Data Analysis	86
3.2.6 Histology and Immunohistochemistry	87
3.3 Results.....	88
3.3.1 Radiation Therapy Planning and Verification	88
3.3.2 WBRT Experiment	94
3.4 Discussion.....	104
3.5 References.....	107
Chapter 4.....	112
4 MRI surveillance of cancer cell fate in a brain metastasis model after early radiotherapy	112
4.1 Introduction.....	112
4.2 Methods.....	113
4.2.1 Cell Culture.....	113
4.2.2 Animal Preparation	114
4.2.3 Radiotherapy	114
4.2.4 Magnetic Resonance Imaging.....	115

4.2.5	Data Analysis	115
4.2.6	Histology and Immunohistochemistry	116
4.3	Results.....	116
4.4	Discussion.....	129
4.5	References.....	131
Chapter 5	133
5	Summary and Future Work.....	133
5.1	Discussion and Conclusions	133
5.1.1	Chapter 2 – HER2+ Breast Cancer Brain Metastasis Models	133
5.1.2	Chapter 3 – Brain Metastasis Response to Radiotherapy	134
5.1.3	Chapter 4 – Cell Tracking and Impact of Early Radiotherapy	135
5.2	Limitations	136
5.3	Future Work	138
5.3.1	Clinical Translation of bSSFP for Tumor Detection	138
5.3.2	Bioluminescence Imaging.....	139
5.3.3	Ex Vivo Brain Metastasis Assay.....	139
5.4	References.....	141
Appendices	143
Curriculum Vitae	149

List of Tables

Table 1.1: Brain-tropic ('BR') breast cancer cell lines.....	12
Table 1.2: T1 and T2 relaxation times	15
Table 1.3: General MRI protocols for brain metastasis detection and evaluation.....	23
Table 2.1: Tumor incidence and burden at endpoint for each brain metastasis model....	62
Table 3.1: Quantification tumor incidence, burden, and mean tumor volume from MRI in the traditional WBRT experiment.....	97

List of Figures

Figure 1.1: Schematic of brain metastases due to breast cancer in a mouse model.	2
Figure 1.2: Brain colonization by metastatic cancer cells	6
Figure 1.3: A breast cancer patient with brain metastasis.	21
Figure 1.4: T1-weighted SE images of approximately the same slice in a mouse brain acquired pre (left) and post (right) Gd contrast agent administration.....	25
Figure 1.5: Visualization of cancer cell fate during metastatic development using cellular MRI.....	30
Figure 2.1: Representative images showing metastases resulting from SUM190-BR3, JIMT-1-BR3, or MDA-MB-231-BR-HER2 human brain metastatic breast cancer.....	60
Figure 2.2: Quantification of mean volume per tumor (\pm SEM) at endpoint in SUM190- BR3, JIMT-1-BR3 and MDA-MB-231-BR-HER2 models.....	63
Figure 2.3: Quantification of the mean percentage of Gd-permeable (black) and Gd- impermeable (white) tumors (\pm SEM).	65
Figure 2.4: <i>In vivo</i> visualization of heterogeneous BTB permeability in the same animal.	67
Figure 2.5: The mean proliferation index (\pm SEM) for Gd-permeable and Gd-impermeable brain metastases in the MDA-MB-231-BR-HER2 model.....	69
Figure 2.6: Representative images of CD31 (top) and CD105 (bottom) staining in SUM190-BR3, JIMT-1-BR3, and MDA-MB-231-BR-HER2 models.....	71
Figure 3.1: Micro-CT/RT targeting for mouse WBRT.....	89

Figure 3.2: Response to radiation-induced DNA DSB was visualized by fluorescent γ -H2AX immunohistochemistry.....	91
Figure 3.3: Representative MRI with correlative histology and immunohistochemistry of metastases in the MDA-MB-231-BR-HER2 brain metastasis model.....	93
Figure 3.4: Representative images of metastases due to MDA-MB-231-BR-HER2 human brain metastatic breast cancer on day 36.	95
Figure 3.5: Treatment response was heterogeneous after traditional WBRT.....	99
Figure 3.6: Tumor permeability visualized and quantified over time by contrast-enhanced MRI.....	101
Figure 3.7: Enhancing and non-enhancing tumors respond differently to WBRT.....	103
Figure 4.1: Visualization of iron-labeled cancer cell delivery with cellular MRI.....	118
Figure 4.2: Monitoring cancer cell fate over time by dilution or retention of the iron oxide label.....	120
Figure 4.4: Early WBRT was able to prevent the growth of tumors.....	124
Figure 4.5: Signal void analysis suggests non-proliferative cancer cells persist after early WBRT.....	126
Figure 4.6: Long-term surveillance of outcome after early radiotherapy.....	128

List of Appendices

Appendix A: Permissions	143
Appendix B: Animal Use Protocol	148

List of Abbreviations

BBB	blood-brain barrier
BLI	bioluminescence imaging
bSSFP	balanced steady state free precession
BTB	blood-tumor barrier
CEST	chemical exchange saturation transfer
CNS	central nervous system
CT	computed tomography
DCE-MRI	dynamic contrast enhanced magnetic resonance imaging
DSB	double stranded breaks
DSC-MRI	dynamic susceptibility contrast-enhanced magnetic resonance imaging
DWI	diffusion weighted imaging
EORTC	European Organization for Research and Treatment of Cancer
FFE	fast field echo
FIESTA	fast imaging employing steady-state acquisition
FISP	fast imaging with steady-state precession
FSL	fractional signal loss
Gd	gadolinium

GE	gradient echo
HER2	human epidermal growth factor receptor 2
ip	intraperitoneal
iv	intravenous
MPIO	micron-sized particle of iron oxide
MRI	magnetic resonance imaging
MRS	magnetic resonance spectroscopy
PCI	prophylactic cranial irradiation
PD	proton density
PPB	Perl's Prussian Blue
RTOG	Radiation Therapy Oncology Group
SCLC	small cell lung cancer
SE	spin echo
SPIO	superparamagnetic particle of iron oxide
SRS	stereotactic radiosurgery
USPIO	ultrasmall superparamagnetic particle of iron oxide
WBRT	whole brain radiotherapy

Chapter 1

1 Introduction

This thesis employs magnetic resonance imaging (MRI) for detection of brain metastasis due to breast cancer in animal models and investigates metastatic response to radiotherapy. This introductory chapter discusses the concepts of brain metastasis, cancer dormancy, neuroimaging in neuro-oncology, cellular MRI, and treatment options for brain metastasis in order to provide background and motivation for the research presented in this thesis.

1.1 Motivation and Overview

True metastatic burden in the brain may be substantially underestimated by clinical imaging protocols (Figure 1.1A). Contrast-enhanced MRI is the gold standard for cancer imaging in the brain; however, there may be tumors that do not take up the contrast agent and therefore would go undetected. Furthermore, there may be a population of dormant, solitary cancer cells present in the brain (Figure 1.1B). These two categories of cancer metastasis represent distinct therapeutic targets and may be spared by therapies that target permeable metastases and actively dividing cancer cells, leading to later disease recurrences. This poses a challenge for effective cancer detection and therapy.

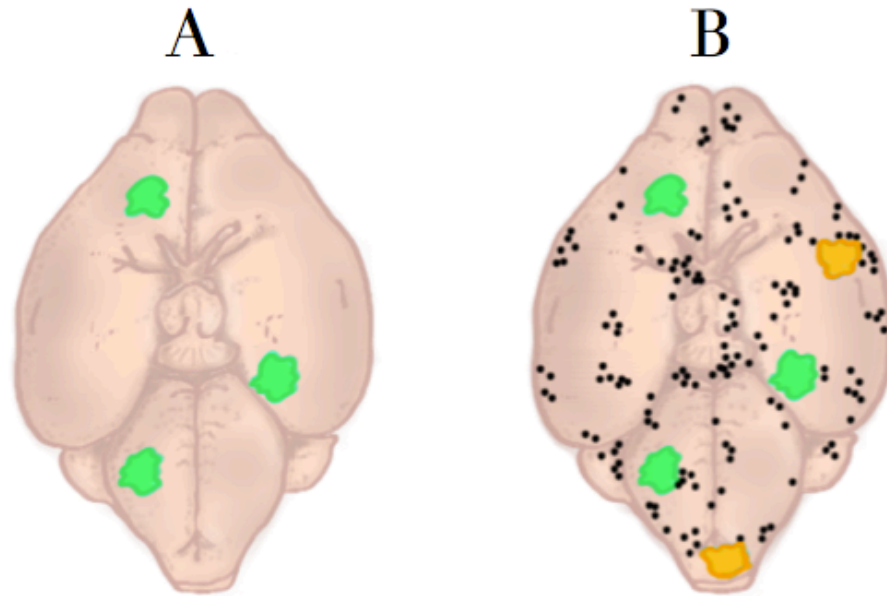


Figure 1.1: Schematic of brain metastases due to breast cancer in a mouse model.

In A the green-colored brain tumors represent those brain metastases that are detected by gadolinium-enhanced MRI; these metastases take up contrast agent. In B these metastases are again shown in green along with (i) orange-colored brain tumors that are detectable by MRI using another sequence that exploits endogenous tumor contrast; these metastases do not take up contrast agent, and therefore are not detected by gadolinium-enhanced MRI, and (ii) black regions of signal void that represent non-proliferative or dormant cancer cells which may be present in the brain but which also would go undetected by conventional MRI techniques.

In this thesis, experimental imaging techniques are presented to identify tumors in mouse brains that do not take up MRI contrast and to monitor the fate of individual cancer cells in animal models of metastatic breast cancer. Chapter 2 investigates contrast agent uptake by tumors in three experimental models and demonstrates substantial heterogeneity between tumors and between models. In chapter 3, mice are treated with radiotherapy to investigate treatment response between tumors that uptake the contrast agent and those that do not; further, this work seeks to understand if it is possible to increase tumor permeability with irradiation, thereby allowing increased contrast agent uptake within the tumor. In chapter 4, radiotherapy is delivered early in metastatic progression and cell tracking techniques are employed to monitor the fate of cancer cells over time and to understand how different cancer cell subpopulations respond to treatment. Finally, chapter 5 summarizes the conclusions and significance of this thesis, discusses experimental limitations, and presents ideas for future work to build on the results presented in this thesis.

1.2 Metastatic Breast Cancer

Breast cancer is the most common cancer in Canadian women and is expected to affect 1 in 9 women in her lifetime [1]. Most deaths due to this disease are a result of breast tumors spreading to regional and distant sites – commonly liver, lung, bone, and brain – by a process called metastasis [2,3,4]. Early detection of metastasis is challenging and current therapies ultimately fail in the metastatic setting.

Breast cancer is a complex and heterogeneous disease that can be classified several ways, including by histopathology, molecular subtype, and grade. Brain metastases can occur in patients with all types of breast cancer; however, this thesis focuses on breast cancer that overexpresses the human epidermal growth factor receptor 2 (HER2+ subtype) as these patients are at high risk for developing brain metastasis [4, 5]. Historically, brain metastases were a late complication in metastatic disease; however, advances in systemic anti-HER2 therapies have significantly improved extra-cranial disease control and the brain is increasingly becoming a first site of relapse in HER2+ breast cancer patients.

1.2.1 Brain Metastasis

Three large studies using population-based cohorts have estimated the incidence of brain metastasis due to breast cancer to range from 5.0 – 32.6% [6, 7, 8]. Still, this is likely an underestimation of true brain metastasis incidence; some metastases may be overlooked because patients are asymptomatic, or already too sick and a diagnosis would be irrelevant to their care. Historically, autopsy studies have reported substantially higher proportions of patients with brain metastasis than what was diagnosed clinically [5].

The incidence of brain metastasis is increasing in the clinic. This is partially because the ability to detect small tumors has improved as better neuroimaging techniques have become available. Furthermore, brain metastases often manifest later in cancer progression; recent advances in treatment options for breast cancer has resulted in longer patient survival and better control of extra-cranial disease thereby allowing the brain and central nervous system (CNS) to become a sanctuary site for metastases. Thus the prevalence of brain metastasis is expected to rise further as systemic therapy improves. For example, HER2+ breast cancer patients treated with trastuzumab develop CNS metastases in 31-48% of cases and 33-50% of those women are responding to therapy or have stable disease at other sites when diagnosed with CNS involvement [10-13].

1.2.2 Metastatic Colonization

Cancer metastasis is an inefficient process [2]. Blood samples from cancer patients may show high numbers of circulating cancer cells; however, few actual metastatic tumors result [14]. This suggests that cancer cell survival during the metastatic cascade must be low, or conditions for cell proliferation in the microenvironment are highly specific. To achieve the first steps of the metastatic cascade, a cell must escape the primary tumor, invade local tissue, and intravasate into the vasculature [15]. It must then survive in the blood and disseminate via the circulation. Many cancer cells will reach the brain in this way and some will arrest in the microcirculation. Initially, cells arrest at blood vessel branches where the cell to vessel diameter ratio approaches one and eventually single cancer cells may then extravasate into the surrounding tissue [16]. Cancer cells can execute these steps with relatively high efficiency [15]. Once the metastatic cancer cell

arrives in the brain, it may experience one of three fates (Figure 1.2): (1) it may die; (2) it may remain viable but dormant; or (3) it may proliferate and form a brain metastasis. Many cells do not survive the required steps for brain colonization [15, 17]. This relies on cancer cell survival outside of the vasculature and invasion of the surrounding tissue, both of which are inefficient steps in the metastatic cascade [15]. Subsequent development or recruitment of tumor-associated vasculature is required for macrometastatic growth; until this vasculature develops, surviving extravasated cancer cells adhere to the outer vessel wall to migrate and access oxygen and nutrients [16, 18].

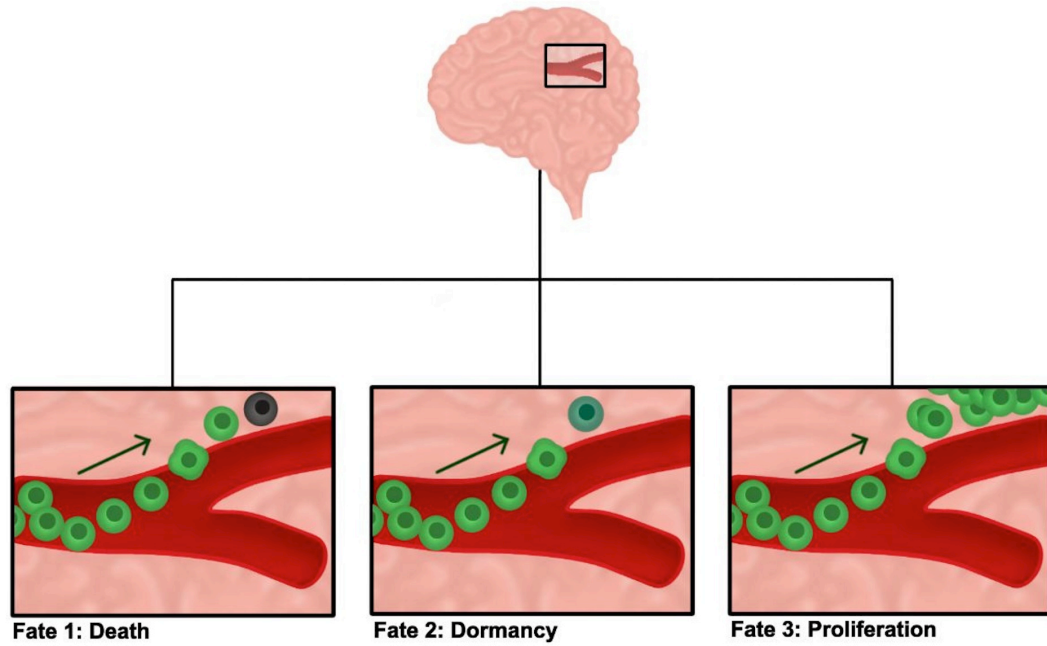


Figure 1.2: Brain colonization by metastatic cancer cells requires that cells survive in the vasculature and arrest in the microcirculation. Single cancer cells may then extravasate out of the vasculature and into the brain where they will experience one of three fates: (1) death, (2) dormancy, where the cell remains viable but non-proliferative, or (3) proliferation to form brain metastases.

1.2.3 The Unique Brain Microenvironment

The brain microenvironment offers a unique metastatic site with vasculature that differs from most other organs. Extra-cranial capillaries are thin and composed of a single endothelial cell layer with various combinations of fenestra, clefts, and pores [19]. Structurally, this allows for uncomplicated exchange of oxygen, carbon dioxide, nutrients, and waste between the blood and surrounding tissue. In contrast, a highly selective barrier surrounds capillaries in the brain. It is comprised of endothelial cells connected by tight junctions, a basement membrane, pericytes, and astrocytes [19]. Together, these components form the blood-brain barrier (BBB), which serves to protect the brain by tightly regulating the diffusion of substrates from the blood into the brain parenchyma. The BBB has very low passive permeability and high levels of efflux transporters, which maintain the internal brain microenvironment and prevent neurotoxicity [19-21]. Under normal conditions, the BBB is extremely exclusive and prevents most traditional systemically administered chemo- and molecular therapeutics from entering the brain in sufficient concentrations for cytotoxicity.

As a cancer cell extravasates from a brain capillary, it penetrates the BBB and the protective cells surrounding the vasculature are displaced. This compromises BBB integrity and a new barrier, known as the blood-tumor barrier (BTB), is formed in its place around the growing tumor. Relatively little is known about the BTB in patients, but its patency appears to vary substantially. For example, tumor detection by clinical imaging relies on extravasation of contrast agents across the BBB/BTB; yet, breast cancer therapeutics such as paclitaxel, doxorubicin, and trastuzumab, which have been highly successful for treating extra cranial metastases, do not cross the BBB/BTB well and are ineffective against brain metastases [10, 22, 23]. Notably, newer therapeutics, such as capecitabine and lapatinib, appear to penetrate the BTB; however, drug uptake within individual brain metastases and among patients is highly variable [24]. It is presumed that partial exclusion from the brain causes these and other chemotherapies to fail, thus rendering the brain a 'sanctuary site' for metastatic growth.

The development of a brain metastasis creates an increasingly high demand for oxygen and nutrients. For most tumors, this need is typically met by the promotion of tumor-associated neovasculature in a process called angiogenesis. The brain is a unique metastatic site because it is the most highly vascularized organ in the human body and, for this reason, cerebral metastases may grow without inducing angiogenesis. Instead, tumors can exploit the rich pre-existing vasculature of the brain through alternative vascularization mechanisms. Tumors may co-opt the innate dense capillary bed in the brain by growing alongside pre-existing microvessels and invading the surrounding brain tissue [25-27]. Co-opted vessel density is lower within brain metastases compared to normal brain; however, dilated vessels within tumors compensate to meet increased metabolic demands [27]. The role of angiogenesis in brain metastasis development was studied by Leenders and colleagues; they investigated the outcome of anti-angiogenic drugs on the development of brain metastasis and found that although angiogenesis was blocked, tumors continued to progress via co-option of the pre-existing vasculature [25]. Thus, brain tumors may develop without angiogenesis.

1.2.4 Dormancy

If cancer cells survive in the metastatic organ, they may co-exist in three forms. Solitary cells may remain in a state of quiescence whereby they remain viable but non-proliferative for an extended period of time; this process of dormancy is likely responsible for clinical recurrence. If solitary cells begin to proliferate, they may form ‘dormant’ micrometastases – proliferative tumors where net tumor size is unchanged due to balanced proliferation and apoptosis – or, they may become actively growing and recruit vasculature by either angiogenic or vessel co-option strategies. These three states of existence represent vastly different cancer biology with significant implications for detection, therapy, and patient outcomes. The factors that control the balance between dormancy and proliferation are poorly understood, but are subject of much ongoing research and discussion [28-34].

Notably, no unique markers have been discovered to identify dormant cancer cells. As a consequence, studying their nature in animal models is limited to assessing lack of

proliferation and apoptosis by histology *ex vivo* or by tracking non-proliferative cells via retention of imaging markers *in vivo*. An important study by Naumov and colleagues investigated dormancy using intravital video microscopy to image fluorescent nanosphere-labeled mammary carcinoma cells (D2.0R and D2A1 cell lines) over time in the mouse liver [35]. They reported large proportions of solitary cells observed *in vivo* and in histology. These apparently dormant cancer cells were then recovered from the liver tissue and re-grown *in vitro* where they regained their proliferative phenotype. Importantly, these cells also uniformly grew primary tumors when re-injected into the mammary fat pad of mice, suggesting dormant cancer cells are viable and their growth arrest is reversible. Recent studies have employed MRI-based cell tracking to monitor dormant cancer cells *in vivo* over time and this is further discussed in the subsection “Cellular MRI” [17, 36-38].

Dormancy, both at the single cell level as well as at the micrometastasis stage, is believed to provide a reservoir of cells that lie in wait until some elusive trigger causes them to proliferate and progress into clinically relevant tumors. This phenomenon presents a significant treatment challenge because its biology deviates from traditional understanding of malignant cancer growth. Current chemotherapies target highly proliferating cells and therefore dormant cells persist, unaffected [38, 39].

1.2.5 Experimental Models for Breast Cancer Brain Metastasis

Laboratory mouse models are most commonly used to study brain metastasis *in vivo*. Few experimental model systems specific for brain metastases due to breast cancer exist [40-43]. These models provide insight into brain metastatic development and enable investigation that is not possible in the clinic.

Both syngeneic and xenograft transplant models exist. Syngenic transplant models introduce murine cancer cells into mouse recipients of the same genetic background. An example of this type of model is the murine 4T1-BR5 brain metastatic breast cancer cell line injected into BALB/c mice [43, 44]. This type of model offers the opportunity to investigate tumor development in the presence of a fully functioning immune system;

however it lacks specificity to human cancer and may not reflect human disease heterogeneity. Xenograft transplant models inoculate immune-compromised hosts with human cancer cell lines that are derived from patient tissue samples, such as in the MDA-MB-231-BR model [40, 41]. Several mouse strains are available for this research with varying degrees of immune-deficiency. This approach lacks functioning immune response, but allows for the direct metastasis modeling that is relevant to human cancer development.

Syngenic and xenograft transplant models can be initiated in similar ways; cancer cells or tumor fragments can be delivered ectopically or hematogenously for brain metastasis development. Some experimental models involve brain metastases that can form spontaneously from a primary tumor. This can be advantageous because the metastatic cascade develops naturally; however, spontaneous models are not frequently reported in breast cancer research. In ectopic injection models, breast tumor cells or tumor fragments are implanted directly into the brain parenchyma or cerebrospinal fluid space for metastasis development. This model is the simplest to initiate and can be useful because it develops only a single tumor in a known location. Moreover, it does not require the use of specific metastatic or brain-tropic cell lines. Though simple, implantation models are limiting because they bypass natural brain colonization and therefore may not adequately model all aspects of metastatic growth. Hematogenous delivery of cancer cells mimics parts of natural metastatic spread by transport of cancer cells via the circulation and therefore creates a more physiologically relevant model. A cancer cell suspension can be injected into the beating left ventricle of the mouse heart (intra-cardiac injection) or into the internal carotid artery (intra-arterial injection) for delivery to the brain. Intra-cardiac injection results in 3.5 – 9.5% of cells delivered to the mouse brain by cardiac output [45, 46]. This model is relatively straightforward, but technically challenging and cancer cells also disseminate to other sites and may cause unwanted tumor growth. Intra-arterial injection improves direct cell delivery to the brain and decreases the potential for extra-cranial metastatic growth [47, 48]. This model is difficult to initiate and advanced microsurgical skill is required to successfully execute inoculation procedures.

Cell lines that preferentially grow in the brain have been developed to use in breast cancer brain metastasis models, such as MDA-MB-231-BR, MDA-MB-231-BR-HER2, JIMT-1-BR3, SUM-190-BR3, and 4T1-BR5 (Table 1.1) [40-43, 49]. These brain metastatic cell lines are derived from primary breast cancer cell lines by repeated rounds of selection. A parental primary cancer cell line that is known to be metastatic is grown in culture and introduced hematogenously into mice. Metastases will develop into various organs over time, including in the brain. Brain tumors are isolated and harvested; these cells are then re-grown in culture [40]. This is referred to as a ‘brain derivative’ of the parental cell line. Biased tropism for the brain is improved by several sequential rounds of re-injection of the ‘brain derivative’ cell line, isolation of brain tumors, and re-growth in culture. These cells lines then inherently prefer the brain microenvironment, which is advantageous in hematogenous delivery models to mitigate metastatic growth in other organs.

Table 1.1: Brain-tropic ('BR') breast cancer cell lines derived from parental cell lines by successive selection rounds for use in preclinical model systems

Cell Line	Origin
MDA-MB-231-BR	Human breast carcinoma; ER-/PR-/HER2-
MDA-MB-231-BR-HER2	Above, transfected with HER2
JIMT-1-BR3	Human breast carcinoma previously isolated from a Herceptin-resistant patient; ER-/PR-/HER2+
SUM-190-BR3	Human inflammatory breast cancer; ER-/PR-/HER2+
4T1-BR5	Murine breast cancer

Complete research models that accurately reflect clinical disease are rare. The MDA-MB-231-BR cell line delivered by intra-cardiac injection has been well characterized and produces a model that is similar to resected human brain metastases from breast cancer in many ways, including proliferation and apoptosis rates [50]. For this reason, the ‘231BR’ model has been used extensively to study brain metastases from triple-negative breast cancer [17, 40, 50-56]. Moreover, the 231BR cell line was transduced with HER2 cDNA (MDA-MB-231-BR-HER2) to create a brain metastasis model for the HER2 subtype of breast cancer [41]. This resulted in the formation of greater numbers of large metastases (>50 μm) compared with the non-HER2 version, but was irrelevant to the development of micrometastases [41, 51]. This thesis employs intracardiac injections of the SUM-190-BR3, JIMT-1-BR3, and MDA-MB-231-BR-HER2 cell lines to initiate experimental models of brain metastasis due to HER2+ breast cancer in nude mice.

1.3 Magnetic Resonance Imaging in Oncology

MRI is a non-invasive and non-ionizing imaging modality that can provide excellent soft tissue contrast with a wide range of contrast mechanisms; it is therefore an ideal method to diagnose cancer and longitudinally monitor progression and treatment responses. MRI relies on the properties of hydrogen atoms (protons) to generate an image. In MRI, protons within a subject are exposed to a strong main magnetic field (B_0) that causes them to align and precess about B_0 . A radiofrequency (RF) excitation pulse is then applied temporarily to change the orientation of the net magnetization vector away from alignment with B_0 . Once the RF is turned off, the protons both dephase and also relax back into alignment with B_0 , emitting energy that produces a signal that can be detected and translated into an image by advanced computer processing. Protons in different tissues and biological states will dephase and realign at different rates. Image contrast in MRI can be generated in many different ways by exploiting these differences. A brief overview of image contrast formation, pulse sequences, and contrast agents is given in the following sections; further discussion of basic MRI physics and image formation can be found in several textbooks, including an excellent overview by McRobbie *et al.*, “MRI from Picture to Proton” [57].

1.3.1 Generating Image Contrast

In general, MR images have contrast that is ‘weighted’ by proton density (PD), spin-lattice relaxation time (T1), or spin-spin relaxation time (T2). PD-weighted images create regions of brightness where there are higher numbers of hydrogen atoms within a given volume. T1-weighted images illustrate contrast that reflects how quickly protons realign with the main magnetic field after RF excitation. Fat-based tissues have a short T1 and appear bright in a T1-weighted image, whereas fluids, such as blood, have long T1 values and appear dark. T2-weighted images depict rates of dephasing after RF excitation. Contrary to T1-weighted images, in T2-weighted images, fat appears dark due to short T2 values and fluid appears bright due to long T2. Sample tissue relaxation times at clinically relevant magnetic field strengths are shown in Table 1.2 [57, 58]. For most tissues T1 relaxation times increase significantly as field strength increases and T2 relaxation times stay close to the same.

Table 1.2: T1 and T2 relaxation times for various tissue types at 1.5 T and 3 T magnetic field strengths.

Tissue type	Animal	1.5 T		3 T	
		T1 (ms)	T2 (ms)	T1 (ms)	T2 (ms)
Liver	mouse	576	46	812	42
Skeletal muscle	mouse	1008	44	1412	50
Heart	mouse	1030	40	1471	47
Kidney	rat	690	55	1194	56
White matter	cow	884	72	1084	69
Gray matter	cow	1124	95	1820	99
Spinal cord	rat	745	74	993	78
Blood	human	1441	290	1932	275
Fat	human	200	-	382	68

The contrast of an MR image is controlled by the pulse sequence, which contains programmed manipulations of the timing and duration of RF and gradient pulses. The combination of pulse timing and duration can exploit the different PD, T1, or T2 in tissues of interest. There are two fundamental types of pulse sequences for MR imaging: spin echo (SE) and gradient echo (GE). Both SE and GE sequences can create images with PD, T1, or T2 weighting. SE sequences produce excellent quality images, but take a relatively long time to acquire. GE sequences are much faster; however, they are affected by main magnetic field inhomogeneity, which causes T2 values to be shorter. Pure T2 contrast is not possible in GE sequences and the contrast is created by the combination of T2 plus magnetic field inhomogeneity, which together is known as T2* [57].

In cancer research, MRI contrast can be manipulated to highlight malignant tissue in anatomical images and derive additional information about tumor biology, function, or treatment response using several different image acquisition techniques. Conventional MRI in oncology includes analysis of T2-weighted images as well as pre- and post-contrast T1-weighted images. In addition to these, many additional novel contrasts are being investigated and translated to application in the clinic. Tumor perfusion and vascularity can be studied using dynamic susceptibility contrast-enhanced MRI (DSC-MRI) or dynamic contrast-enhanced MRI (DCE-MRI) [59-61]. Cellularity of cancers can also be studied by a technique called diffusion-weighted imaging (DWI) [61-63]. Magnetic resonance spectroscopy (MRS) can be employed to investigate cancer biochemistry, and hyperpolarized MRI can be used to study tumor metabolism [59, 63-65]. Chemical exchange saturation transfer MRI (CEST MRI) can measure tumor pH and multinuclear MRI can image other nuclei that are abundant in cancer growth [66, 67]. Finally, cell tracking can be used in preclinical models to monitor cancer cell fate and molecular imaging can provide a targeted method to detect changes in cancerous tissue prior to anatomical changes occurring [17, 36, 37, 68, 69].

This thesis employs two pulse sequences to investigate brain metastasis development. Contrast-enhanced T1-weighted SE images are acquired to study BBB integrity and tumor permeability. The balanced steady state free precession (bSSFP) pulse sequence is

used to image tumor development in the brain and track iron-labeled cancer cells. These sequences are discussed in the following section.

1.3.2 Relevant Pulse Sequences

The SE pulse sequence is a common and relatively straightforward image acquisition. The contrast is produced by two main parameters: repetition time (TR) and echo time (TE). The TR refers to the time between RF excitation pulses in consecutive repetitions of the pulse sequence. The TE is the time between the RF excitation pulse and the echo. Short TE and TR create T1-weighted images [57].

In the magnet, but prior to initiating the pulse sequence, the magnetization vector is aligned with B_0 and points along the z-axis. In the SE pulse sequence, a 90° RF pulse is applied and tips the magnetization vector into the x-y plane. The spins begin to dephase and realign with B_0 in a process known as free induction decay (FID). After a short duration $TE/2$, a 180° RF pulse is applied to refocus the spins; this brings the spins back into phase at TE when the echo is formed and the signal is acquired [57]. During this series of excitations and readout, spatial localization of the signal is achieved by applying magnetic fields that vary with position, known as gradient fields, in the x- y- and z- directions. A slice-select gradient (G_z) is turned on during the 90° and 180° RF excitation pulses to determine the position of the imaging slice along the z-direction. A phase-encoding gradient (G_y) is turned on briefly between the excitation pulses, which causes a temporary change in precession speed and causes protons to acquire phase shifts based on their position in the y-direction [57]. To acquire a complete image, this phase-encode gradient is applied with different strengths during each TR. Frequency-encoding gradients (G_x) are turned on during readout and cause protons to precess at different frequencies along the x-axis. The RF signal acquired during readout is digitized and used to fill a data matrix known as k-space, which can then produce an image after applying a Fourier transform.

The bSSFP pulse sequence is a type of GE sequence that is known as Balanced Fast Field Echo (balanced FFE), True Fast Imaging with Steady-state Precession (True FISP), or

Fast Imaging Employing Steady-state acquisition (FIESTA) on Philips, Siemens, and General Electric MRI scanners respectively [57]. A typical GE sequence employs a RF pulse with flip angle α , which tips the magnetization vector towards the x-y plane when applied. Slice-select and phase-encoding gradients are used as in the SE pulse sequence. Dephasing of the transverse magnetization is accelerated by the application of a dephasing readout gradient and reversed by a rephasing gradient with opposite polarity to acquire signal with short TE. Dephasing due to magnetic field inhomogeneity is not rephased in this process and GE sequences are therefore affected by T_2^* [57].

In the bSSFP pulse sequence, signal is conserved due to lack of gradient-induced dephasing during each TR. This is achieved by the application of compensating gradient pulses with equal strength but opposite polarity, such that the dephasing induced by a negative gradient is “balanced” by that of a positive gradient. The result is a highly SNR efficient pulse sequence with interesting T_2/T_1 -weighted image contrast [70, 71]. Scheffler and Lehnhardt give an excellent illustration and description of how the magnetization vector is manipulated during bSSFP and further discuss the principles of this pulse sequence [70].

1.3.3 Contrast Agents

Contrast media is often employed in MRI for cancer research to increase the signal difference between normal tissue and primary tumors, metastatic lesions, or cancer cells. The most common MRI contrast agents are Gadolinium-based chelates (Gd), which are strongly paramagnetic and increase the T_1 relaxation rate ($1/T_1$) of nearby nuclei causing brightness where Gd accumulates. Images are typically acquired before and after intravenous (iv) injection of these agents. In most of the body, Gd initially travels through blood vessels and then extravasates into the interstitial space or undergoes renal clearance. Post-Gd T_1 -weighted images can be used to visualize vasculature in the early stages, or tissue enhancement patterns at later stages. Zhou and Lu recently reviewed Gd-based contrast agents for MR cancer imaging [72].

Iron oxide nanoparticles are another class of MRI contrast agents that create negative contrast by causing local magnetic field inhomogeneities [73]. This causes increased dephasing and increases the T2 relaxation rate ($1/T2$ or $1/T2^*$) of nearby nuclei, resulting in areas of signal void. These agents come in a range of sizes, including: micron-sized particles of iron oxide (MPIO), superparamagnetic iron oxide nanoparticles (SPIO), and ultra-small SPIO (USPIO) [74]. The smallest are USPIO and are referred to as blood pool agents; imaging performed before and after the iv administration of USPIO allows for characterization of tumor vasculature and assessment of vascular volume [75-77]. Imaging cancer cells using iron oxide nanoparticles is further discussed in “Cellular MRI.”

1.3.4 Neuroimaging in Neuro-Oncology

Suspicion of brain metastasis is evaluated by imaging – usually computed tomography (CT) or MRI – where lesions of several millimeters in size are generally radiographically detectable. Contrast-enhanced cranial CT can detect many brain metastases; however, diagnosis by MRI is considered superior due to better soft tissue contrast, ability to detect smaller tumors, fewer artifacts, and ability to acquire images in all three planes and without the risk of ionizing radiation dose to the patient [78]. The radiological appearance of brain metastasis is diverse and varies substantially with primary tumor origin. Generally, the lesion is well demarcated from the brain parenchyma, though it may also be surrounded by cerebral edema.

Contrast-enhanced T1-weighted (T1w) MRI is widely regarded as the most accurate method for clinical brain tumor detection [79, 80]. In healthy brain, the BBB prevents Gd from diffusing out of the circulation. By contrast, the BBB is often disrupted in the local area of a tumor due to tumor infiltration, increased vascular permeability, or poorly constructed angiogenic vessels. Tumors are identified by diffusion of Gd across the impaired BBB/BBB, which results in signal enhancement (brightness) in the post-Gd image.

A clinical MRI session includes many image acquisitions to create different contrasts and gain information about the structure of the brain and tumor. Figure 1.3 illustrates some example images from a brain metastasis imaging protocol in a pre-radiotherapy MR simulation session at the London Regional Cancer Program.

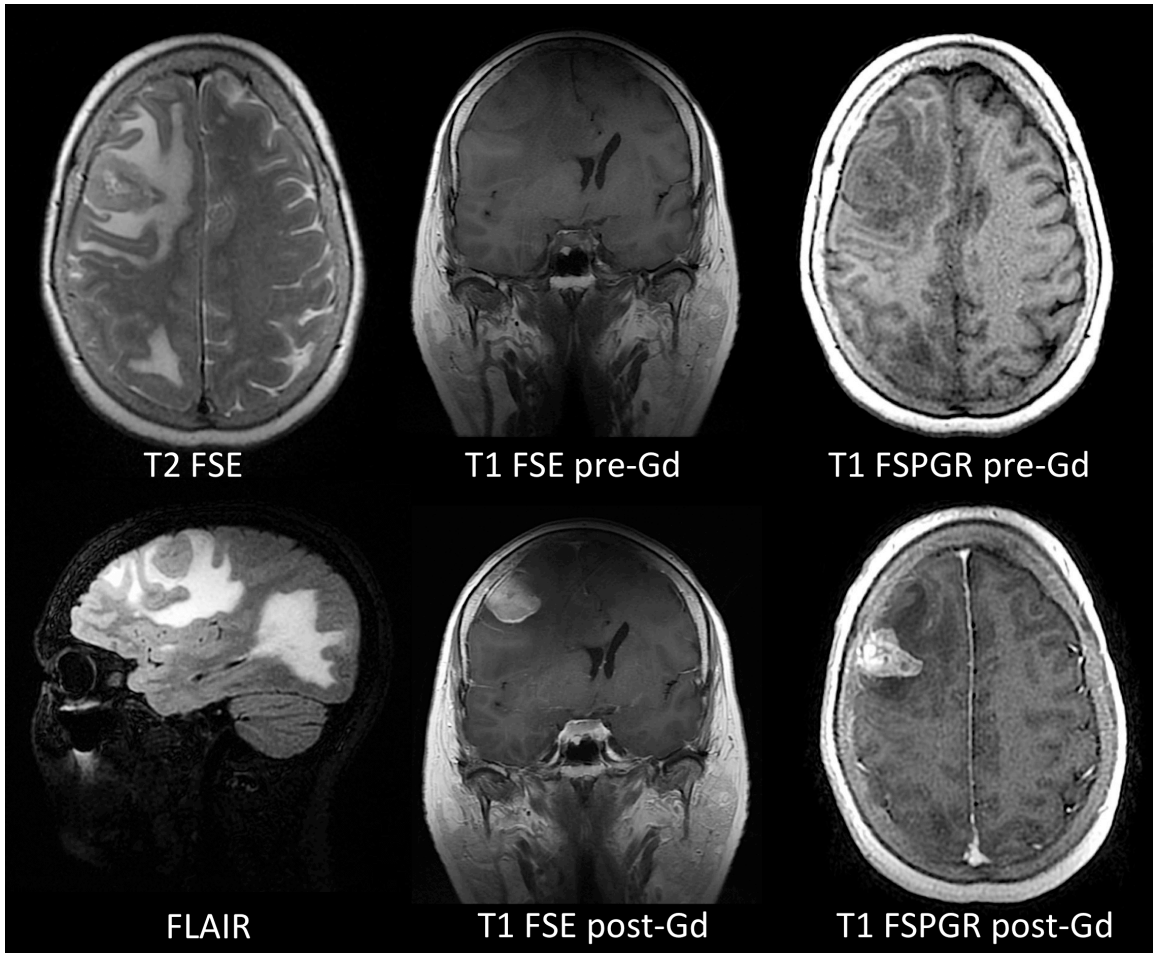


Figure 1.3: A breast cancer patient with brain metastasis. Axial T2-weighted fast spin echo (T2 FSE) imaging illustrates substantial edema surrounding the tumor. The sagittal fluid-attenuated inversion recovery (FLAIR) image has similar contrast to the T2 FSE, but cerebrospinal fluid signal is suppressed for better imaging of lesions near the ventricles. T1-weighted pre- and post-Gd coronal FSE and axial fast spoiled gradient echo (FSPGR) images demonstrate heterogeneous signal enhancement within the tumor mass.

Employing multiple contrast mechanisms aids radiologists to differentiate a brain metastasis from a primary brain tumor, cerebral abscess, or stroke. Furthermore, these protocols may be used to evaluate response after treatment. MR sequences that are used for brain metastasis visualization and evaluation, as well as tumor appearance, are described in Table 1.3 [80-82].

Table 1.3: General MRI protocols for brain metastasis detection and evaluation.

MRI Protocol	Tumor Appearance
T1-weighted <i>pre Gd iv</i>	isointense or mildly hypointense; melanin may cause hyperintensities in some brain metastases due to melanoma; hemorrhagic metastases may also be hyperintense
<i>post Gd iv</i>	intense enhancement throughout, in nodes, or ring-enhancing
T2-weighted	hyperintense; melanin may cause some brain metastases due to melanoma to appear hypointense
Diffusion-weighted imaging	hyperintense on apparent diffusion coefficient map
MR perfusion	increased cerebral blood volume and blood flow
MR spectroscopy	increased metabolic activity; choline and N-acetyl aspartate are common metabolites that are compared with creatine, which is used as an internal control

If imaging suggests clinical presentation of metastatic lesions in the brain, stereotactic or open biopsy may be indicated to confirm diagnosis and characterize the metastasis [79]. Though invasive, biopsy is useful to rule out inflammation or infection, which may appear similar to a metastatic lesion by radiology or MRI.

1.3.5 Pre-clinical Imaging of Blood-Brain Barrier Integrity

Several groups have used Gd-enhanced MRI to evaluate the permeability of the BBB/BTB associated with brain tumors in experimental rodent models [25, 49, 61, 83, 84]. Figure 1.4 shows T1-weighted images of the mouse brain pre- and post-Gd. After Gd, 231-BR-HER2 brain metastases are detectable as regions of signal enhancement due to local disruption in the BBB, which allows Gd to cross and accumulate. Using this technique, Percy and colleagues reported substantial heterogeneity in the permeability of breast cancer brain metastases, even within the same brain [84]. Many of the metastases became permeable with time, suggesting that as they develop changes to the tumor vasculature compromise the integrity of the BBB. At the last imaging time point there were approximately 4 times as many Gd-permeable metastases as Gd-impermeable. Gd-permeable metastases were significantly larger than non-permeable tumors, however, size alone was not sufficient to predict permeability [84]. The impermeability of the BBB hinders the delivery of chemotherapeutic agents to the brain, limiting the success of pharmacological approaches to treat brain metastases [22-24]. The ability to use MRI to noninvasively assess the permeability status of brain metastases will be important for understanding the process of brain metastasis and for evaluating the development of BBB-permeable chemotherapeutic drugs.

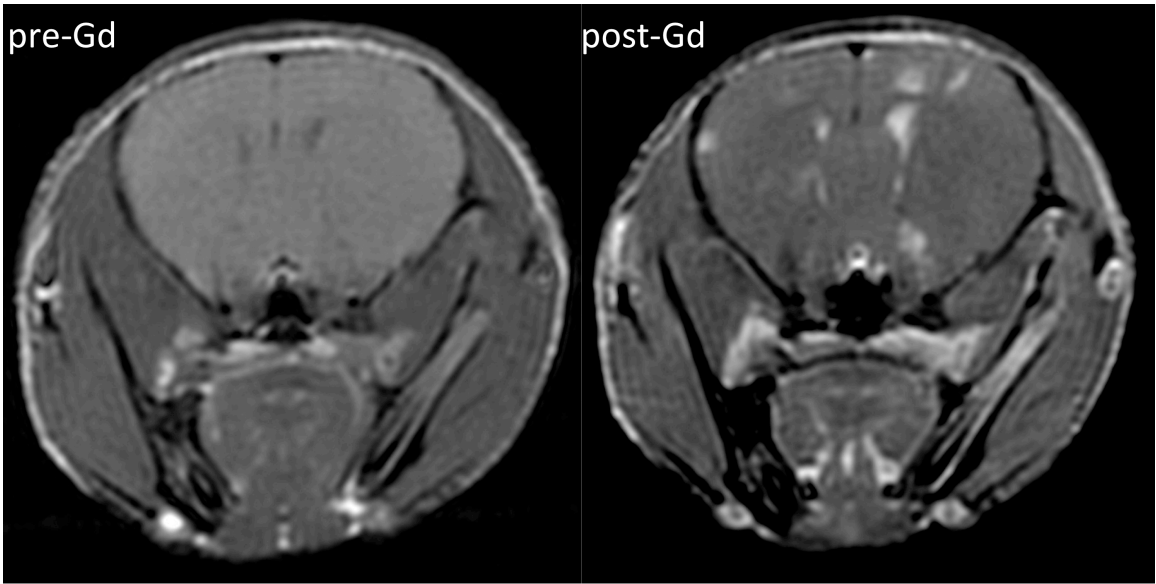


Figure 1.4: T1-weighted SE images of approximately the same slice in a mouse brain acquired pre (left) and post (right) Gd contrast agent administration. Brain tumors are not detectable before Gd (left). After Gd, 231-BR-HER2 metastases are detectable as regions of signal enhancement due to local disruption in the BBB, which allows Gd to cross and accumulate (right).

1.3.6 Cellular MRI

Iron oxide nanoparticles are the most commonly used contrast agents for MRI cell tracking and the development of this technology has been thoroughly reviewed [85-90]. These agents create negative contrast in T2- or T2*-weighted proton MR images because the iron within them causes a local magnetic field inhomogeneity that leads to shorter transverse (T2) and effective transverse (T2*) relaxation times of nearby nuclei; this results in MR signal loss, which extends to occupy more space in an image than the dimensions of the contrast agent or cell itself, and is known as the “blooming artifact” [73]. The degree of contrast in an MR image is derived from the ability of iron oxide nanoparticles to change local relaxation rates ($R2^*=1/T2^*$), which depends on relaxivity values and contrast agent concentration; it is also sensitive to imaging parameters such as field strength, pulse sequence, resolution, and SNR [73, 89, 91-93]. Iron-labeled cells may appear as large areas of hypointensity or discrete regions of signal void in MR images depending on cell density in the target organ.

Many different iron oxide nanoparticles exist as MRI contrast agents and they fall into three categories based on size. Kochinski and colleagues recently reviewed iron oxide contrast agents for MRI and compared the properties and clinical approval status of several commonly used agents in the field [89]. In general, MPIO are the largest with diameters $\geq 1 \mu\text{m}$ and have the highest iron loading per particle. SPIO are relatively smaller at about 50-100 nm, and the smallest agents are USPIO at ≤ 50 nm in diameter [74, 89]. Selection of an MPIO, SPIO, or USPIO contrast agent for imaging depends on the application. The iron content of a single MPIO particle is about 1 pg Fe/particle and is equivalent to 1.5 million SPIO particles or 4.3 million USPIO [94]. Labeling cells with MPIO therefore offers the ability to substantially increase iron content within cells with a reasonable contrast agent volume and improves cell detectability *in vivo*, even at low numbers. Notably, single cell detection is possible, even at clinical field strengths, with MPIO or SPIO cell labeling [17, 73, 95-97]. Applications with MPIO are limited to preclinical investigation because the polymer matrix composition of these particles is not biodegradable.

Cell imaging using MRI has shown great utility in preclinical studies; however widespread use of MRI cell tracking in the clinic has not yet been achieved. This is largely due to the limited availability of commercial, FDA approved imaging agents. Ferumoxides (trade names: Feridex or Endorem) and ferucarbotrans (trade name: Resovist) are FDA-approved SPIO contrast agents used clinically for liver imaging; however these products were withdrawn from the market [98]. Now, in the absence of approved iron-oxide imaging agents, FDA-approved iron replacement therapies, such as Ferumoxytol (trade name: Feraheme), are being investigated off-label as USPIO contrast agents for MR imaging [99, 100].

Cellular MRI has the capacity to track transplanted or endogenous cells with MPIO, SPIO, or USPIO depending on the cell labeling strategy that is used. *In vivo* cell labeling is achieved by systemic injection of iron oxide nanoparticles to primarily image endogenous immune cells due to their innate phagocytic activity. Cells can also be labeled *in vitro* and subsequently implanted into a host for imaging. Many cell types take up iron oxide nanoparticles in culture without intervention and can be iron-labeled by simple co-incubation [17, 73, 95, 96, 101, 102]. In cell types that are not innately phagocytic, internalization of iron nanoparticles may be improved using transfection agents, electroporation, or magnetofection [103-106].

Iron-labeled cell tracking has been applied to a variety of cell types, including: stem cells, immune cells, cancer cells, pancreatic islets, and hepatocytes [17, 36, 37, 52, 96, 97, 102, 103, 107-118]. Despite concerns about functional and phenotypic alterations that could prevent accurate recapitulation of normal and pathological processes, very few detrimental effects have been observed regarding iron-labeled cells at a wide range of iron-loadings. MPIO or SPIO labeling of cancer cells has no discernable effect on viability, *in vitro* proliferation, apoptosis, necrosis, or *in vivo* metastatic efficiency compared to unlabeled cells [17, 36, 52]. Similarly, SPIO labeling of human mesenchymal and hematopoietic stem cells has no significant short- or long-term effects on viability, proliferation, or differentiation to adipogenic and osteogenic lineages; however there may be some effect on chondrogenesis [103, 119]. Notably, Rohani *et al.*

reported that MPIO-labeling of dendritic cells affects activation and maturation, though no differences in viability were found [112].

Relatively few groups have used MRI to track labeled cancer cells, compared to other cell types. This is because iron particles are diluted in the progeny of proliferative cells and therefore labeled cells become undetectable by MRI after repeated cell divisions. Foster *et al.* monitored the iron content in proliferating melanoma cells (B16F10) *in vitro* using inductively coupled plasma-mass spectroscopy and microscopy. They reported the disappearance of intracellular iron in cancer cells after 5 days; this represented approximately the 6th generation of daughter cells and suggested these progeny would be undetectable by MRI [36]. Economopoulos *et al.* found a similar pattern of dilution for breast cancer cells (MDA-MB-231) using flow cytometry and PPB staining; by 4 days post-labeling, less than 50% of cells retained detectable quantities of iron. Notably, 1-2.5% of cells still remained labeled by day 10, which suggests they were non-proliferative or slowly cycling [37]. Heyn and colleagues obtained comparable results in a brain metastatic breast cancer model (MDA-MB-231-BR) by investigating *ex vivo* brain tissue sections stained with PPB. They observed both iron-positive solitary cells and micro-metastases; however, large tumors did not reveal any regions with iron-positive staining, despite nearly 100% labeling efficiency at the time of cell injection [17].

Heyn *et al.* were the first to show that cellular MRI had the sensitivity to detect single iron-labeled cancer cells upon initial arrest in the brain, which is important for tracking metastatic spread [17, 97]. Single cell detection was feasible despite the intrinsically low sensitivity of this imaging modality by exploiting the blooming artifact, which caused 15-fold amplification in the representation of individual MPIO-labeled cancer cells. That is, cancer cells of approximately 20 μm in diameter created discrete signal voids that were 300 μm wide in the MR image [17]. Moreover, the discrete signal voids detected in MRI could be co-registered with microscopy images that revealed the presence of solitary DiI-labeled and green fluorescent cancer cells [17, 97].

Cellular MRI technology has also been adapted to follow cancer cell fate in animal models over time. Heyn and colleagues monitored brain metastatic development over one

month in the MDA-MB-231-BR model [17]. Regions of signal void representing solitary and small clusters of iron-labeled cells were visible in the brain early after injection. After one-month surveillance, three distinct cell fates were discernable. Consistent with metastatic inefficiency, most cancer cells were ‘transient’ (93.9%); these signal voids were present after injection but disappeared over time. A small population of cells was ‘proliferative’ (1.6%) and appeared as regions of signal void after injection that later grew into tumors at the same location. Finally, ‘non-proliferative’ cancer cells were also observed (4.5%) by virtue of long-term MPIO retention causing regions of persisting signal void in MR images and iron-positive cells in PPB-stained brain sections [17]. This subpopulation of non-proliferative cancer cells is thought to represent ‘quiescent’ or ‘dormant’ cancer cells that are in reversible G0-G1 cell cycle arrest and may proliferate to form relevant metastases in the future. Illustration of cell fate surveillance using this technique is shown in Figure 1.5 where proliferative and non-proliferative cancer cells are co-detected in the mouse brain over time.

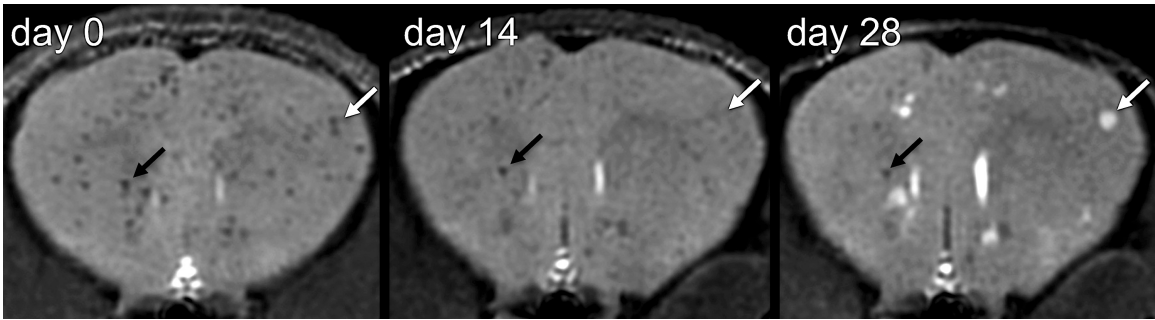


Figure 1.5: Visualization of cancer cell fate during metastatic development using cellular MRI. Tracking MPIO-labeled MDA-MB-231-BR-HER2 cells in the mouse brain over time reveals distinct cancer subpopulations with different latency periods. After intracardiac injection (day 0), all cancer cells arresting in the brain appear similar as discrete regions of signal void. Over time, the iron label is diluted among proliferative cells and they are undetectable by MRI until a tumor forms in their place (white arrow). Slowly-cycling or non-proliferative cancer cells can be detected alongside proliferative cells and tumors due to their long-term retention of the iron label (black arrow).

The retention of iron by slowly-cycling or non-proliferative cancer cells has been exploited by some groups to monitor this unique cell population. Magnitsky *et al.* tracked slowly-cycling UPSIO, SPIO, and MPIO-labeled melanoma cells (WM3734) within the tumor mass using *in vivo* and *ex vivo* MRI. They found slowly-cycling iron-labeled cells often formed clusters nearby vasculature; interestingly, this observation was previously associated with cancer stem cells [115]. Consistent with this result, Economopoulos *et al.* also observed distinct zones of hypointensity due to clusters of iron-retaining non-proliferative cancer cells within primary tumors (MDA-MB-231). Notably, this group also found regions of signal void within the lymph nodes and was the first to observe migration of metastatic iron-labeled cancer cells from a primary tumor [37].

Cellular MRI has been useful to simultaneously monitor treatment response of both non-proliferating iron-labeled cancer cells and macroscopic tumor burden. Townson *et al.* used this approach in a murine model of melanoma metastasis to the liver (B16F1) and reported heterogeneous response among metastatic cell populations to cytotoxic chemotherapy with doxorubicin [38]. The growth of metastasis was inhibited by 1 mg/kg doxorubicin administered three times weekly; however, the number of co-existing dormant cancer cells, as measured by signal void area, did not change after treatment [38]. Importantly, eradication of the tumor burden would have suggested complete and successful response to treatment, had cell tracking not revealed a substantial population of persisting cancer cells in MRI. Further investigation of the dormant cell population by cellular MRI is warranted; if these cells are viable and clonogenic, then they may play a critical role in treatment failure leading to recurrence.

1.4 Treatment for Brain Metastasis

In general, systemic chemo- and molecular anti-cancer therapies, which are highly successful at treating extra-cranial metastases, are ineffective for brain metastases because they are unable to cross the intact BBB/BTB in sufficient concentrations [10, 22-24, 44]. This leaves few treatment options for brain metastases. The National Comprehensive Cancer Network published their consensus on clinical practice guidelines in oncology for CNS cancers, which included management strategies for brain metastases

[79]. Symptoms, such as headache, neurologic dysfunction, and seizures, can be managed with steroids and anti-epileptic drugs. Corticosteroids, such as dexamethasone, are used to reduce swelling in the brain and to help alleviate symptoms. This treatment alone offers survival of only 1 – 2 months [120]. Primary anti-cancer treatment possibilities to extend survival include: whole brain radiotherapy (WBRT), surgical resection, stereotactic radiosurgery (SRS), or some combination of these.

WBRT is a mainstay in the treatment for brain metastasis; in this method, radiation dose is delivered to the entire brain volume, regardless of tumor location. It is often used as an adjuvant therapy, though it can be used alone for palliation. WBRT alone improves neurologic symptoms and may extend survival to 4 – 6 months; however, recurrences in the brain after WBRT alone are common [121, 122].

Surgical resection involves craniotomy followed by neurosurgery to remove or debulk the tumor mass. In 1990, Patchell and colleagues published results indicating that surgical resection followed by WBRT was superior to WBRT alone in a randomized trial including 48 patients with a solitary brain metastasis. In this study, the surgical group outlived the radiation group by more than 2.5 times and remained functionally independent nearly 5 times longer [123].

In 1998, Patchell and colleagues published another randomized clinical trial comparing surgical resection alone versus surgical resection followed by WBRT and determined that adjuvant WBRT was beneficial for patients with a single metastasis, even when complete surgical resection of the tumor was achieved. Recurrence in the brain was reduced in the radiotherapy group and patients were less likely to die from neurologic causes than patients who underwent surgical resection alone [124].

SRS offers an alternative and less invasive treatment option compared to surgery. This is beneficial for tumors that develop in eloquent cortical areas, which were previously considered untreatable due to potentially devastating neurological side effects from surgery. Furthermore, SRS is advantageous for treatment of deep-seated and otherwise

unresectable tumors [79]. This technique uses multiple convergent radiation beams to deliver very high radiation doses to a precise tumor volume.

1.4.1 Oligometastatic Disease (1 – 3 metastases)

Patients presenting with few metastatic lesions on MRI (typically 1 – 3) and controlled extra-cranial disease may undergo surgical resection [79]. Surgical excision of brain metastasis may also be indicated, regardless of systemic disease status, if the mass effect by the tumor causes significant symptoms for the patient. Tumor location and accessibility are critical factors for determining if surgical intervention is the most feasible and advantageous approach.

Following resection, WBRT and/or SRS are used as adjuvant therapies to control micrometastatic disease in the surgical bed and surrounding brain tissue [79]. WBRT is delivered in radiation doses ranging from 20 – 40 Gy in 5 – 20 fractions, though 30Gy/10 or 37.5Gy/15 are common treatment regimens [79, 125]. SRS typically uses single doses of 15-24 Gy [79]. In some cases, WBRT may be delivered in addition to a SRS ‘boost’ to the surgical bed.

The primary treatment for patients with oligometastatic disease that is not amenable to surgery is WBRT and/or SRS. In the Radiation Therapy Oncology Group (RTOG 9508) clinical trial of patients with one to three brain metastases, Andrews and colleagues found that SRS in combination with WBRT improved survival when compared to WBRT alone but only in the subset of patients with single metastases or favorable features. In addition, patients who underwent SRS had better neurologic function six months post-treatment than those who had WBRT alone [126]. There is concern that WBRT leads to neurocognitive decline compared to SRS or surgical resection. Nevertheless, in the comparison of SRS or surgical resection of one to three brain metastases versus the same treatments followed by WBRT, the European Organization for Research and Treatment of Cancer (EORTC 22952-26001) study found that adding WBRT reduced recurrence of initial brain metastases and the development of new metastases but did not improve overall survival or functional decline [127].

If oligometastatic disease is presented with disseminated systemic disease, then WBRT followed by appropriate systemic therapy are used as primary treatment [79].

1.4.2 Multiple Metastatic Lesions (>3 metastases)

WBRT is the clinical standard for treating multiple (e.g. > 3) brain metastases and diffuse disease, though this treatment alone is generally considered palliative. Surgical resection may be considered to relieve mass effect [79]. In patients with unfavorable prognostic scores, supportive care only may be an option.

1.4.3 Preventative Treatment

Prophylactic cranial irradiation (PCI) is a preventative treatment for patients at high-risk of developing clinically relevant brain metastasis. It is a WBRT-like regimen that is employed if developing micro-metastatic foci are suspected in the brain, but are not yet detectable by radiology. PCI decreased the subsequent incidence of brain metastasis in a study of 286 patients with extensive small-cell lung cancer (SCLC) responding to chemotherapy; moreover, PCI prolonged both disease-free and overall survival [128]. Despite the significant survival benefit in SCLC patients, PCI does not guarantee prevention of brain metastasis and may cause unwanted neurocognitive side effects. For this reason, the risk to benefit ratio for this method is not favorable in many other cancers. The utility of PCI is therefore mainly limited to SCLC patients, though it has been discussed for some patients with advanced metastatic breast cancer who develop brain metastasis at a high rate, such as those who are HER2+ [129].

1.5 Purpose of Thesis

This thesis uses MRI to monitor the development of brain metastasis due to HER2+ breast cancer and track cancer cells in mouse models over time. The objectives of this work were to use *in vivo* MR image techniques to characterize new models of brain metastasis due to HER2+ breast cancer and investigate how radiotherapy affected metastatic development, dormancy, and tumor permeability.

1.5.1 Hypotheses

1. There will be differences in tumor growth and morphology, as well as differences in MRI appearance, of brain metastasis resulting from each of the HER2+ breast cancer cell lines: SUM-190-BR3, JIMT-1-BR3, and MDA-MB-231-BR-HER2.
2. A modified micro-CT/RT system can be used to irradiate the whole mouse brain to a dose of 10 Gy per fraction in a reasonable treatment time.
3. WBRT, when delivered after tumor detection by MRI, will decrease the tumor burden and increase tumor permeability to Gd.
4. Early WBRT will halt the transition to growth from disseminated solitary cancer cells, but will not alter the number of non-proliferative cancer cells.

In Chapter 2, high resolution anatomical and contrast-enhanced MRI was used to quantify tumor growth and BBB integrity in three experimental models of brain metastasis due to HER2+ breast cancer. This work explores the relationship between tumor development and permeability as well as the heterogeneity present amongst animal models of the same disease. This chapter was published in *Translational Oncology* (Murrell DH *et al.*, *Understanding heterogeneity and permeability of brain metastases in murine models of HER2-positive breast cancer through magnetic resonance imaging: implications for detection and therapy* *Translational Oncology* 2015 8(3):176-184).

In Chapter 3, a micro-CT/RT system was commissioned for use in mouse brain irradiation. This was then employed to develop a clinically relevant WBRT plan to investigate the impact of radiation on brain metastasis development and BBB permeability in the MDA-MB-231-BR-HER2 model. This chapter was published in *Translational Oncology* (Murrell DH *et al.*, *Evaluating changes to blood-brain barrier integrity in brain metastasis over time and after radiation treatment* *Translational Oncology* 2016 9(3): 219-227).

In Chapter 4, the micro-CT/RT system and mouse WBRT plan were used to investigate the impact of early radiation treatment on brain metastasis development and dormancy in the MDA-MB-231-BR-HER2 model. This chapter is under review in *Radiotherapy and Oncology* (Murrell DH *et al.*, *MRI surveillance of cancer cell fate in a brain metastasis model after early radiotherapy* *Radiotherapy and Oncology*).

1.6 References

1. Canadian Cancer Society's Advisory Committee on Cancer Statistics. Canadian Cancer Statistics 2015. Toronto, ON: Canadian Cancer Society; 2015.
2. Chambers AF, Groom AC, MacDonald IC. Dissemination and growth of cancer cells in metastatic sites. *Nat Rev Cancer* 2002;2:563–72.
3. Maxmen A. The Hard Facts. *Nature* 2012;485:4–6.
4. Kennecke H, Yerushalmi R, Woods R, Cheang MCU, Voduc D, Speers CH, *et al.* Metastatic behavior of breast cancer subtypes. *J Clin Oncol* 2010;28:3271–7.
5. Lin NU, Winer EP. Brain metastases: the HER2 paradigm. *Clin Cancer Res* 2007;13:1648–55.
6. Schouten LJ, Rutten J, Huveneers HAM, Twijnstra A. Incidence of brain metastases in a cohort of patients with carcinoma of the breast, colon, kidney, and lung and melanoma. *Cancer* 2002;94:2698–705.
7. Barnholtz-Sloan JS, Sloan AE, Davis FG, Vigneau FD, Lai P, Sawaya RE. Incidence Proportions of Brain Metastases in Patients Diagnosed (1973 to 2001) in the Metropolitan Detroit Cancer Surveillance System. *J Clin Oncol* 2004;22:2865–72.
8. Smedby KE, Brandt L, Bäcklund ML, Blomqvist P. Brain metastases admissions in Sweden between 1987 and 2006. *Br J Cancer* 2009;101:1919–24.
9. Lin NU, Bellon JR, Winer EP. CNS Metastases in Breast Cancer. *J Clin Oncol* 2004;22:3608–17. d
10. Stemmler HJ, Kahlert S, Siekiera W, Untch M, Heinrich B, Heinemann V. Characteristics of patients with brain metastases receiving trastuzumab for HER2 overexpressing metastatic breast cancer. *Breast* 2006;15:219–25.

11. Shmueli E, Wigler N, Inbar M. Central nervous system progression among patients with metastatic breast cancer responding to trastuzumab treatment. *Eur J Cancer* 2004;40:379–82.
12. Bendell JC, Domchek SM, Burstein HJ, Harris L, Younger J, Kuter I, *et al.* Central nervous system metastases in women who receive trastuzumab-based therapy for metastatic breast carcinoma. *Cancer* 2003;97:2972–7.
13. Lai R, Dang CT, Malkin MG, Abrey LE. The risk of central nervous system metastases after trastuzumab therapy in patients with breast carcinoma. *Cancer* 2004;101:810–6.
14. Tarin D, Price JE, Kettlewell MGW, Souter RG, Vass ACR, Crossley B. Mechanisms of Human Tumor Metastasis Studied in Patients with Peritoneovenous Shunts. *Cancer Res* 1984;44:3584–92.
15. Chambers AF, Naumov GN, Vantghem SA, Tuck AB. Molecular biology of breast cancer metastasis. Clinical implications of experimental studies on metastatic inefficiency. *Breast Cancer Res* 2000;2:400–7.
16. Kienast Y, von Baumgarten L, Fuhrmann M, Klinkert WEF, Goldbrunner R, Herms J, *et al.* Real-time imaging reveals the single steps of brain metastasis formation. *Nat Med* 2010;16:116–22.
17. Heyn C, Ronald JA, Ramadan SS, Snir JA, Barry AM, MacKenzie LT, *et al.* In vivo MRI of cancer cell fate at the single-cell level in a mouse model of breast cancer metastasis to the brain. *Magn Reson Med* 2006;56:1001–10.
18. Steeg PS, Camphausen KA, Smith QR. Brain metastases as preventive and therapeutic targets. *Nat Rev Cancer* 2011;11:352–63.
19. Deeken JF, Löscher W. The blood-brain barrier and cancer: transporters, treatment, and Trojan horses. *Clin Cancer Res* 2007;13:1663–74.

20. Kemper EM, Boogerd W, Thuis I, Beijnen JH, van Tellingen O. Modulation of the blood-brain barrier in oncology: therapeutic opportunities for the treatment of brain tumours? *Cancer Treat Rev* 2004;30:415–23.
21. Arshad F, Wang L, Sy C, Avraham S, Avraham HK. Blood-brain barrier integrity and breast cancer metastasis to the brain. *Patholog Res Int* 2010;2011:920509.
22. Stemmler H-J, Schmitt M, Willems A, Bernhard H, Harbeck N, Heinemann V. Ratio of trastuzumab levels in serum and cerebrospinal fluid is altered in HER2-positive breast cancer patients with brain metastases and impairment of blood-brain barrier. *Anticancer Drugs* 2007;18:23–8.
23. Connell JJ, Chatain G, Cornelissen B, Vallis KA, Hamilton A, Seymour L, *et al.* Selective permeabilization of the blood-brain barrier at sites of metastasis. *J Natl Cancer Inst* 2013;105:1634–43.
24. Morikawa A, Peereboom DM, Thorsheim HR, Samala R, Balyan R, Murphy CG, *et al.* Capecitabine and lapatinib uptake in surgically resected brain metastases from metastatic breast cancer patients: a prospective study. *Neuro Oncol* 2014:1–7.
25. Leenders WPJ, Küsters B, Verrijp K, Maass C, Wesseling P, Heerschap A, *et al.* Antiangiogenic Therapy of Cerebral Melanoma Metastases Results in Sustained Tumor Progression via Vessel Co-Option. *Clin Cancer Res* 2004;10:6222–30.
26. Donnem T, Hu J, Ferguson M, Adighibe O, Snell C, Harris AL, *et al.* Vessel co-option in primary human tumors and metastases: an obstacle to effective anti-angiogenic treatment? *Cancer Med* 2013;2:427–36.
27. Bugyik E, Dezso K, Reiniger L, László V, Tóvári J, Tímár J, *et al.* Lack of angiogenesis in experimental brain metastases. *J Neuropathol Exp Neurol* 2011;70:979–91.

28. Barkan D, Chambers AF. β 1-Integrin: A Potential Therapeutic Target in the Battle against Cancer Recurrence. *Clin Cancer Res* 2011;17:7219–23.
29. Ghajar CM, Peinado H, Mori H, Matei IR, Evason KJ, Brazier H, *et al.* The perivascular niche regulates breast tumour dormancy. *Nat Cell Biol* 2013;15:807–17.
30. Sosa MS, Bragado P, Debnath J, Aguirre-Ghiso JA. Regulation of Tumor Cell Dormancy by Tissue Microenvironments and Autophagy. *Adv Exp Med Biol* 2013;734:73–89.
31. Ruggiero A, Bruzzo J, Chiarella P, Gianni P, Isturiz MA, Linskens S. Tyrosine Isomers Mediate the Classical Phenomenon of Concomitant Tumor Resistance. *Cancer Res* 2011;71:7113–25.
32. Baum M, Demicheli R, Hrushesky W, Retsky M. Does surgery unfavourably perturb the “natural history” of early breast cancer by accelerating the appearance of distant metastases? *Eur J Cancer* 2005;41:508–15.
33. Galmarini CM, Tredan O, Galmarini FC. Concomitant resistance and early-breast cancer: should we change treatment strategies? *Cancer Metastasis Rev* 2014;33:271–83.
34. Demicheli R. Tumour dormancy: findings and hypotheses from clinical research on breast cancer. *Semin Cancer Biol* 2001;11:297–305.
35. Naumov GN, MacDonald IC, Weinmeister PM, Kerkvliet N, Nadkarni KV, Wilson SM, *et al.* Persistence of Solitary Mammary Carcinoma Cells in a Secondary Site: A Possible Contributor to Dormancy. *Cancer Res* 2002; 62:2162-8.
36. Foster PJ, Dunn EA, Karl KE, Snir JA, Nycz CM, Harvey AJ, *et al.* Cellular Magnetic Resonance Imaging: In Vivo Imaging of Melanoma Cells in Lymph Nodes of Mice. *Neoplasia* 2008;10:207–16.

37. Economopoulos V, Chen Y, McFadden C, Foster PJ. MRI Detection of Nonproliferative Tumor Cells in Lymph Node Metastases Using Iron Oxide Particles in a Mouse Model of Breast Cancer. *Transl Oncol* 2013;6:347–54.
38. Townson JL, Ramadan SS, Simeanea C, Rutt BK, MacDonald IC, Foster PJ, *et al.* Three-dimensional imaging and quantification of both solitary cells and metastases in whole mouse liver by magnetic resonance imaging. *Cancer Res* 2009;69:8326–31.
39. Naumov GN, Townson JL, MacDonald IC, Wilson SM, Bramwell VH, Groom AC, *et al.* Ineffectiveness of doxorubicin treatment on solitary dormant mammary carcinoma cells or late-developing metastases. *Breast Cancer Res Treat* 2003;82:199–206.
40. Yoneda T, Williams PJ, Hiraga T, Niewolna M, Nishimura R. A bone-seeking clone exhibits different biological properties from the MDA-MB-231 parental human breast cancer cells and a brain-seeking clone in vivo and in vitro. *J Bone Miner Res* 2001;16:1486–95.
41. Palmieri D, Bronder JL, Herring JM, Yoneda T, Weil RJ, Stark AM, *et al.* Her-2 overexpression increases the metastatic outgrowth of breast cancer cells in the brain. *Cancer Res* 2007;67:4190–8.
42. Tanner M, Kapanen AI, Junttila T, Raheem O, Grenman S, Elo J, *et al.* Characterization of a novel cell line established from a patient with Herceptin-resistant breast cancer. *Mol Cancer Ther* 2004;3:1585–92.
43. Tao K, Fang M, Alroy J, Sahagian GG. Imagable 4T1 model for the study of late stage breast cancer. *BMC Cancer* 2008;8:228–46.
44. Lockman PR, Mittapalli RK, Taskar KS, Rudraraju V, Gril B, Bohn KA, *et al.* Heterogeneous blood-tumor barrier permeability determines drug efficacy in

- experimental brain metastases of breast cancer. *Clin Cancer Res* 2010;16:5664–78.
45. Quintana A, Raczka E, Bonaccorsi A. Cardiac output distribution measured with radioactive microspheres in the mouse. *Pharmacol Res Commun* 1979;11:245–52.
 46. Basse P, Hockland P, Heron I, Hokland M. Fate of Tumor Cells Injected Into Left Ventricle of Heart in BALB/c Mice: Role of Natural Killer Cells. *J Natl Cancer Inst* 1988;80:657–65.
 47. Schackert G, Price J, Bucana C, Fidler I. Unique patterns of brain metastasis produced by different human carcinomas in athymic nude mice. *Int J Cancer* 1989;44:892–7.
 48. Kim LS, Huang S, Lu W, Lev DC, Price JE. Vascular endothelial growth factor expression promotes the growth of breast cancer brain metastases in nude mice. *Clin Exp Metastasis* 2004;21:107–18.
 49. Murrell DH, Hamilton AM, Mallett CL, van Gorkum R, Chambers AF, Foster PJ. Understanding Heterogeneity and Permeability of Brain Metastases in Murine Models of HER2-Positive Breast Cancer Through Magnetic Resonance Imaging: Implications for Detection and Therapy. *Transl Oncol* 2015;8:176–84.
 50. Fitzgerald DP, Palmieri D, Hua E, Hargrave E, Herring JM, Qian Y, *et al.* Reactive glia are recruited by highly proliferative brain metastases of breast cancer and promote tumor cell colonization. *Clin Exp Metastasis* 2008;25:799–810.
 51. Perera M, Ribot EJ, Percy DB, McFadden C, Simehra C, Palmieri D, *et al.* In Vivo Magnetic Resonance Imaging for Investigating the Development and Distribution of Experimental Brain Metastases due to Breast Cancer. *Transl Oncol* 2012;5:217–25.

52. Ribot EJ, Martinez-Santesteban FM, Simedrea C, Steeg PS, Chambers AF, Rutt BK, *et al.* In vivo single scan detection of both iron-labeled cells and breast cancer metastases in the mouse brain using balanced steady-state free precession imaging at 1.5 T. *J Magn Reson Imaging* 2011;34:231–8.
53. Kil WJ, Cerna D, Burgan WE, Beam K, Carter D, Steeg PS, *et al.* In vitro and in vivo radiosensitization induced by the DNA methylating agent temozolomide. *Clin Cancer Res* 2008;14:931–8.
54. McGowan PM, Simedrea C, Ribot EJ, Foster PJ, Palmieri D, Steeg PS, *et al.* Notch1 inhibition alters the CD44^{hi}/CD24^{lo} population and reduces the formation of brain metastases from breast cancer. *Mol Cancer Res* 2011;9:834–44.
55. Taskar KS, Rudraraju V, Mittapalli RK, Samala R, Thorsheim HR, Lockman J, *et al.* Lapatinib distribution in HER2 overexpressing experimental brain metastases of breast cancer. *Pharm Res* 2012;29:770–81.
56. Gril B, Palmieri D, Bronder JL, Herring JM, Vega-Valle E, Feigenbaum L, *et al.* Effect of lapatinib on the outgrowth of metastatic breast cancer cells to the brain. *J Natl Cancer Inst* 2008;100:1092–103.
57. McRobbie DW, Moore EA, Graves MJ, Prince MR. *MRI From Picture to Proton*. 2nd edition. New York: Cambridge University Press; 2007.
58. Stanisz GJ, Odobina EE, Pun J, Escaravage M, Graham SJ, Bronskill MJ, *et al.* T1, T2 Relaxation and Magnetization Transfer in Tissue at 3T. *Magn Reson Med* 2005;54:507–12.
59. Law M, Cha S, Knopp EA, Johnson G, Arnett J, Litt AW. High-Grade Gliomas and Solitary Metastases: Differentiation by Using Perfusion and Proton Spectroscopic MR Imaging. *Neuroradiology* 2002;222:715–21.

60. Bello E, Colella G, Scarlato V, Oliva P, Berndt A, Valbusa G, *et al.* E-3810 Is a Potent Dual Inhibitor of VEGFR and FGFR that Exerts Antitumor Activity in Multiple Preclinical Models 2011;71:1396–406.
61. Budde MD, Gold E, Jordan EK, Frank JA. Differential microstructure and physiology of brain and bone metastases in a rat breast cancer model by diffusion and dynamic contrast enhanced MRI. *Clin Exp Metastasis* 2012;29:51–62.
62. Moffat BA, Chenevert TL, Meyer CR, Mckeever PE, Hall DE, Hoff BA, *et al.* The Functional Diffusion Map: An Imaging Biomarker for the Early Prediction of Cancer Treatment Outcome. *Neoplasia* 2006;8:259–67.
63. Ross BD, Chenevert TL, Kim B, Ben-Yoseph O. Magnetic Resonance Imaging and Spectroscopy: Application to Experimental Neuro-Oncology. *Q Magn Reson Biol Med* 1994;1:89–106.
64. Rodrigues TB, Serrao EM, Kennedy BWC, Hu D, Kettunen MI, Brindle KM. Magnetic resonance imaging of tumor glycolysis using hyperpolarized ¹³C-labeled glucose. *Nat Med* 2014;20:93–8.
65. Mallett CL, Lim H, Thind K, Chen Y, Ribot EJ, Martinez F, *et al.* Longitudinal Anatomical and Metabolic MRI Characterization of Orthotopic Xenograft Prostate Tumors in Nude Mice. *J Magn Reson Imaging* 2014;856:848–56..
66. McVicar N, Li AX, Meakin SO, Bartha R. Imaging chemical exchange saturation transfer (CEST) effects following tumor-selective acidification using lonidamine. *NMR Biomed* 2015;28:566–75.
67. Ouwerkerk R, Jacobs MA, Macura KJ, Wolff AC, Stearns V, Mezban SD, *et al.* Elevated tissue sodium concentration in malignant breast lesions detected with non-invasive ²³Na MRI. *Breast Cancer Res Treat* 2007;106:151–60.

68. Artemov D, Mori N, Okollie B, Bhujwala ZM. MR Molecular Imaging of the Her-2/neu Receptor in Breast Cancer Cells Using Targeted Iron Oxide Nanoparticles. *Magn Reson Med* 2003;49:403–8.
69. Banerjee SR, Ngen EJ, Rotz MW, Kakkad S, Lisok A, Pracitto R, *et al.* Synthesis and Evaluation of GdIII-Based Magnetic Resonance Contrast Agents for Molecular Imaging of Prostate-Specific Membrane Antigen. *Angew Chem Int Ed* 2015;54:10778–82.
70. Scheffler K, Lehnhardt S. Principles and applications of balanced SSFP techniques. *Eur Radiol* 2003;13:2409–18.
71. Bieri O, Scheffler K. Fundamentals of balanced steady state free precession MRI. *J Magn Reson Imaging* 2013;38:2–11.
72. Zhou Z, Lu Z-R. Gadolinium-Based Contrast Agents for MR Cancer Imaging. *Wiley Interdiscip Rev Nanomed Nanobiotechnol* 2013;5:1–18.
73. Heyn C, Bowen C V, Rutt BK, Foster PJ. Detection threshold of single SPIO-labeled cells with FIESTA. *Magn Reson Med* 2005;53:312–20.
74. Modo M, Hoehn M, Bulte JWM. Cellular MR imaging. *Mol Imaging* 2005;4:143–64.
75. Gambarota G, Leenders W. Characterization of Tumor Vasculature in Mouse Brain by USPIO Contrast-Enhanced MRI. *Methods Mol Biol*, 2011, p. 477–87.
76. Gambarota G, Leenders W, Maass C, Wesseling P, Kogel B Van Der, Telling O Van, *et al.* Characterisation of tumour vasculature in mouse brain by USPIO contrast-enhanced MRI. *Br J Cancer* 2008;98:1784–9.
77. Leenders W, Küsters B, Pikkemaat J, Wesseling P, Ruiter D, Heerschap A, *et al.* Vascular endothelial growth factor-A determines detectability of experimental

- melanoma brain metastasis in GD-DTPA-enhanced MRI. *Int J Cancer* 2003;105:437–43.
78. Schellinger PD, Meinck HM, Thron A. Diagnostic accuracy of MRI compared to CCT in patients with brain metastases. *J Neurooncol* 1999;44:275–81.
 79. Brem SS, Bierman PJ, Black P, Blumenthal DT, Brem H, Chamberlain MC, *et al.* Central nervous system cancers: Clinical Practice Guidelines in Oncology. *J Natl Compr Canc Netw* 2011;9:352–400.
 80. Fink KR, Fink JR. Imaging of brain metastases. *Surg Neurol Int* 2013;4:S209–19.
 81. Cha S. Update on Brain Tumor Imaging: From Anatomy to Physiology. *AJNR Am J Neuroradiol* 2006;27:475–87.
 82. Cha S. Neuroimaging in Neuro-Oncology. *Neurotherapeutics* 2009;6:465–77.
 83. Kemper EM, Leenders W, Kusters B, Lyons S, Buckle T, Heerschap A, *et al.* Development of luciferase tagged brain tumour models in mice for chemotherapy intervention studies. *Eur J Cancer* 2006;42:3294–303.
 84. Percy DB, Ribot EJ, Chen Y, McFadden C, Simeone C, Steeg PS, *et al.* In vivo characterization of changing blood-tumor barrier permeability in a mouse model of breast cancer metastasis: a complementary magnetic resonance imaging approach. *Invest Radio* 2011; 46:718-25.
 85. Bulte JW, Kraitchman DL. Iron oxide MR contrast agents for molecular and cellular imaging. *NMR Biomed* 2004;17:484–99.
 86. Gupta AK, Gupta M. Synthesis and surface engineering of iron oxide nanoparticles for biomedical applications. *Biomaterials* 2005;26:3995–4021.
 87. Rogers WJ, Meyer CH, Kramer CM. Technology Insight: in vivo cell tracking by use of MRI. *Nat Clin Pract* 2006;3:554–62.

88. Dekaban GA, Hamilton AM, Fink CA, Au B, de Chickera SN, Ribot EJ, *et al.* Tracking and evaluation of dendritic cell migration by cellular magnetic resonance imaging. *WIREs Nanomed Nanobiotechnol* 2013;5:469–83.
89. Korchinski DJ, Taha M, Yang R, Nathoo N, Dunn JF. Iron Oxide as an MRI Contrast Agent for Cell Tracking. *Magn Reson Insights* 2015;8:15–29.
90. Bull E, Madani SY, Sheth R, Seifalian A, Green M, Seifalian AM. Stem cell tracking using iron oxide nanoparticles. *Int J Nanomedicine* 2014;9:1641–53.
91. Weissleder R, Bogdanov A, Neuwelt EA, Papisov M. Long-circulating iron oxides for MR imaging. *Adv Drug Deliv Rev* 1995;16:321–34.
92. Ramadan SS, Heyn C, Mackenzie LT, Chambers AF, Rutt BK, Foster PJ. Ex-vivo cellular MRI with b-SSFP: quantitative benefits of 3T over 1.5T. *Magn Reson Mater Phys* 2008;21:251–9.
93. Tanimoto A, Kuribayashi S. Application of superparamagnetic iron oxide to imaging of hepatocellular carcinoma. *Eur J Radiol* 2006;58:200–16.
94. Shapiro EM, Koretsky AP. Micron-Sized Iron Oxide Particles (MPIOs) for Cellular Imaging: More Bang for the Buck. In: Bulte JWM, Modo MMJ, editors. *Nanoparticles Biomed. Imaging*, Springer New York; 2008, p.141–61.
95. Foster-Gareau P, Heyn C, Alejski A, Rutt BK. Imaging Single Mammalian Cells With a 1.5T Clinical MRI Scanner. *Magn Reson Med* 2003;49:968–71.
96. Shapiro EM, Sharer K, Skrtic S, Koretsky AP. In Vivo Detection of Single Cells by MRI. *Magn Reson Med* 2006;55:242–9.
97. Heyn C, Ronald JA, Mackenzie LT, MacDonald IC, Chambers AF, Rutt BK, *et al.* In vivo magnetic resonance imaging of single cells in mouse brain with optical validation. *Magn Reson Med* 2006;55:23–9.

98. Ahrens ET, Bulte JWM. Tracking immune cells in vivo using magnetic resonance imaging. *Nat Rev Immunol* 2013;13:755–63.
99. Bashir MR, Bhatti L, Marin D, Nelson RC. Emerging Applications for Ferumoxytol as a Contrast Agent in MRI. *J Magn Reson Imaging* 2015;41:884–98.
100. Hamilton B, Nesbit G, Dosa E, Gahramanov S, Rooney B, Nesbit E, *et al.* Comparative analysis of ferumoxytol and gadoteridol enhancement using T- and T2-weighted MRI in neuroimaging. *AJR Am J Roentgenol* 2011;197:981–8.
101. McFadden C, Mallett CL, Foster PJ. Labeling of multiple cell lines using a new iron oxide agent for cell tracking by MRI. *Contrast Media Mol Imaging* 2011;6:514–22.
102. Gonzalez-Lara LE, Xu X, Hofstetrova K, Pniak A, Chen Y, McFadden CD, *et al.* The use of cellular magnetic resonance imaging to track the fate of iron-labeled multipotent stromal cells after direct transplantation in a mouse model of spinal cord injury. *Mol Imaging Biol* 2011;13:702–11.
103. Arbab AS, Yocum GT, Kalish H, Jordan EK, Anderson SA, Khakoo AY, *et al.* Efficient magnetic cell labeling with protamine sulfate complexed to ferumoxides for cellular MRI. *Blood* 2004;104:1217–24.
104. Walczak P, Kedziorek DA, Gilad AA, Lin S, Bulte JWM. Instant MR Labeling of Stem Cells Using Magnetoelectroporation 2005;774:769–74.
105. Siegers GM, Ribot EJ, Keating A, Foster PJ. Extensive expansion of primary human gamma delta T cells generates cytotoxic effector memory cells that can be labeled with Feraheme for cellular MRI. *Cancer Immunol Immunother* 2013;62:571–83.

106. Kedziorek DA, Kraitchman DL. Superparamagnetic Iron Oxide Labeling of Stem Cells for MRI Tracking and Delivery in Cardiovascular Disease. *Methods Mol Biol* 2010;660:171–83.
107. Hinds KA, Hill JM, Shapiro EM, Laukkanen MO, Silva AC, Combs CA, *et al.* Highly efficient endosomal labeling of progenitor and stem cells with large magnetic particles allows magnetic resonance imaging of single cells. *Blood* 2003;102:867–72.
108. Ahrens ET, Xu H, Genove G, Morel PA. Receptor-Mediated Endocytosis of Iron-Oxide Particles Provides Efficient Labeling of Dendritic Cells for In Vivo MR Imaging. *Magn Reson Med* 2003;49:1006–13.
109. Shapiro EM, Medford-Davis LN, Fahmy TM, Dunbar CE, Koretsky AP. Antibody-mediated cell labeling of peripheral T cells with micron-sized iron oxide particles (MPIOs) allows single cell detection by MRI. *Contrast Media Mol Imaging* 2007;2:147–53.
110. Dekaban GA, Snir J, Shrum B, de Chickera S, Willert JC, Merrill M, *et al.* Semiquantitation of Mouse Dendritic Cell Migration In Vivo Using Cellular MRI. *J Immunother* 2009;32:240–51.
111. Zhang X, Chickera SNDE, Willert C, Economopoulos V, Noad J, Rohani R, *et al.* Cellular magnetic resonance imaging of monocyte-derived dendritic cell migration from healthy donors and cancer patients as assessed in a scid mouse model. *Cytotherapy* 2011;13:1234–48.
112. Rohani R, de Chickera SN, Willert C, Chen Y, Dekaban GA, Foster PJ. In vivo cellular MRI of dendritic cell migration using micrometer-sized iron oxide (MPIO) particles. *Mol Imaging Biol* 2011;13:679–94.
113. de Chickera SN, Willert C, Mallet C, Foley R, Foster PJ, Dekaban GA. Cellular MRI as a suitable, sensitive non-invasive modality for correlating in vivo

- migratory efficiencies of different dendritic cell populations with subsequent immunological outcomes. *Int Immunol* 2012;24:29–41.
114. Bernas LM, Foster PJ, Rutt BK. Imaging Iron-Loaded Mouse Glioma Tumors With bSSFP at 3T. *Magn Reson Med* 2010;64:23–31.
 115. Magnitsky S, Roesch A, Herlyn M, Glickson JD. In Vivo and Ex Vivo MR Imaging of Slowly Cycling Melanoma Cells. *Magn Reson Med* 2011;66:1362–73.
 116. Berkova Z, Jirak D, Zacharovova K, Kriz J, Lodererova A, Girman P, *et al.* Labeling of Pancreatic Islets With Iron Oxide Nanoparticles for In Vivo Detection With Magnetic Resonance. *Transplantation* 2008;85:155–9.
 117. Barnett BP, Arepally A, Karmarkar PV, Qian D, Gilson WD, Walczak P, *et al.* Magnetic resonance-guided, real-time targeted delivery and imaging of magnetocapsules immunoprotecting pancreatic islet cells. *Nat Med* 2007;13:986–91.
 118. Evgenov NV, Medarova Z, Dai G, Bonner-Weir S, Moore A. In vivo imaging of islet transplantation. *Nat Med* 2006;12:144–8.
 119. Kostura L, Kraitchman DL, Mackay AM, Pittenger MF, Bulte JWM. Feridex labeling of mesenchymal stem cells inhibits chondrogenesis but not adipogenesis or osteogenesis. *NMR Biomed* 2004;17:513–7.
 120. Weissman DE. Glucocorticoid Treatment for Brain Metastases and Epidural Spinal Cord Compression: A Review. *J Clin Oncol* 1988;6:543–51.
 121. Viani GA, Castilho MS, Salvajoli J V, Pellizzon ACA, Novaes PE, Guimarães FS, *et al.* Whole brain radiotherapy for brain metastases from breast cancer: estimation of survival using two stratification systems. *BMC Cancer* 2007;7:53–61.

122. Mahmoud-Ahmed AS, Suh JH, Lee S-Y, Crownover RL, Barnett GH. Results of whole brain radiotherapy in patients with brain metastases from breast cancer: a retrospective study. *Int J Radiat Oncol Biol Phys* 2002;54:810–7.
123. Patchell RA, Tibbs PA, Walsh JW, Dempsey RJ, Maruyama Y, Kryscio RJ, *et al.* A randomized trial of surgery in the treatment of single metastases to the brain. *N Engl J Med* 1990;322:494–500.
124. Patchell RA, Tibbs PA, Regine WF, Dempsey RJ, Mohiuddin M, Kryscio RJ, *et al.* Postoperative Radiotherapy in the Treatment of Single Metastases to the Brain. *J Am Med Assoc* 1998;280:1485–9.
125. Son CH, Jimenez R, Niemierko A, Loeffler JS, Oh KS, Shih H a. Outcomes after whole brain reirradiation in patients with brain metastases. *Int J Radiat Oncol Biol Phys* 2012;82:e167–72.
126. Andrews DW, Scott CB, Sperduto PW, Flanders AE, Gaspar LE, Schell MC, *et al.* Whole brain radiation therapy with or without stereotactic radiosurgery boost for patients with one to three brain metastases: phase III results of the RTOG 9508 randomised trial. *Lancet* 2004;363:1665–72.
127. Kocher M, Soffiatti R, Abacioglu U, Villà S, Fauchon F, Baumert BG, *et al.* Adjuvant whole-brain radiotherapy versus observation after radiosurgery or surgical resection of one to three cerebral metastases: Results of the EORTC 22952-26001 study. *J Clin Oncol* 2011;29:134–41.
128. Slotman B, Faivre-Finn C, Kramer G, Rankin E, Snee M, Hatton M, *et al.* Prophylactic cranial irradiation in extensive small-cell lung cancer. *N Engl J Med* 2007;357:664–72.
129. Huang F, Alrefae M, Langleben A, Roberge D. Prophylactic cranial irradiation in advanced breast cancer: a case for caution. *Int J Radiat Oncol Biol Phys* 2009;73:752–8.

Chapter 2

2 Understanding Heterogeneity and Permeability of Brain Metastases in Murine Models of HER2-positive Breast Cancer through Magnetic Resonance Imaging: Implications for Detection and Therapy

Objectives: Brain metastases due to breast cancer are increasing and the prognosis is poor. Lack of effective therapy is attributed to heterogeneity of breast cancers and their resulting metastases, as well as impermeability of the blood-brain barrier (BBB), which hinders delivery of therapeutics to the brain. This work investigates three experimental models of HER2+ breast cancer brain metastasis to better understand the inherent heterogeneity of the disease. We use MRI to quantify brain metastatic growth and explore its relationship with BBB permeability. **Methods:** Brain metastases due to breast cancer cells (SUM190-BR3, JIMT-1-BR3, or MDA-MB-231-BR-HER2) were imaged at 3T using balanced steady state free precession (bSSFP) and contrast-enhanced T1-weighted spin echo sequences. The histology and immunohistochemistry corresponding to MRI was also analyzed. **Results:** There were differences in metastatic tumor appearance by MRI, histology, and immunohistochemistry (Ki67, CD31, CD105) across the three models. The mean volume of a MDA-MB-231-BR-HER2 tumor was significantly larger compared to other models [$F(2,12)=5.845$, $p < 0.05$]; interestingly, this model also had a significantly higher proportion of Gd-impermeable tumors [$F(2,12)=22.18$, $p < 0.0001$]. Ki67 staining indicated that Gd-impermeable tumors had significantly more proliferative nuclei compared to Gd-permeable tumors [$t(24)=2.389$, $p < 0.05$] in the MDA-MB-231-BR-HER2 model. CD31 and CD105 staining suggested no difference in new vasculature patterns between permeable and impermeable tumors in any model. **Conclusions:** Significant heterogeneity is present in these models of brain metastases from HER2+ breast cancer. Understanding this heterogeneity, especially as it relates to BBB permeability, is important for improvement in brain metastasis detection and treatment delivery.

2.1 Introduction

Breast cancer will affect approximately 1 in 8 American women [1]. It is the most commonly diagnosed cancer in women and is the second leading cause of cancer death in American women [1]. The major challenge of this disease is its propensity to metastasize to distant sites such as bone, liver, lung, and brain [2]. The relative rate of breast cancer brain metastasis is extremely high, second only to lung cancer [3].

Breast cancer is a complex and heterogeneous disease and is classified into at least four molecular subtypes with different prognostic significance; further classification exists by histological type and grade [2, 4, 5]. No single subgroup is biologically homogeneous. The HER2 subtype – estrogen receptor negative (ER-), progesterone receptor negative (PR-), HER2+ [6] – is of particular concern since it accounts for 10-15% of breast cancers and develops brain metastases at a significantly higher rate compared to other breast cancer subtypes [2, 7].

Brain metastases that form from breast cancers are also complex and heterogeneous. These can manifest in three clinically distinct situations: multiple brain metastases (78%), solitary brain metastasis (14%), or leptomeningeal metastasis (8%) [8]. Each manifestation dictates a different course of treatment; however, responses to therapy vary among metastases. Some metastases will not respond to therapy while others will appear to initially respond, but develop resistance during treatment, or will cause recurrence at a later time. This heterogeneity in tumor response complicates clinical management and contributes to the poor prognosis for this disease.

Clinical data suggest that HER2 overexpression is present in as many as 53% of breast cancer brain metastasis cases [7]. Median survival from diagnosis of HER2+ brain metastases to death is 4-6 months and less than 20% of patients can expect to live one year [9]. Treatment for HER2+ metastatic breast cancer includes anti-HER2 therapy such as trastuzumab (Herceptin®). Despite improvement in both disease-free and overall survival [10], CNS metastases develop in 31-48% of patients on trastuzumab [11-14] and 33-50% of those are responding to therapy or have stable disease at other sites when

diagnosed with CNS involvement [11, 14]. This suggests that the brain offers a sanctuary site where metastases can persist, unaffected by therapy.

The poor prognosis for brain metastases has been largely attributed to obstacles created by the BBB. Under normal conditions, the BBB acts to protect the brain by tightly regulating the diffusion of substrates from the blood into the brain parenchyma [15]; however this also causes systemic therapies to be excluded from the brain. For example, chemo- and targeted therapies – such as doxorubicin and trastuzumab – which are highly successful at treating HER2+ metastases in other areas of the body, are ineffective for brain metastases [14, 16] presumably because they are unable to cross the intact BBB.

Studying brain metastatic breast cancer is challenging because there are few experimental animal models [17-20]. The MDA-MB-231-BR cell line has been the most widely used to study brain metastasis from breast cancer [18, 21-29]. Work performed in the Steeg laboratory has shown that this preclinical model shares many characteristics of human brain metastases [22]. The MDA-MB-231-BR cell line has also been transduced with HER2 cDNA (resulting in the MDA-MB-231-BR-HER2 cell line) and significant heterogeneity in the permeability of the BBB associated with these brain metastases was demonstrated by Lockman *et al.* using dextran perfusion and *ex vivo* fluorescence microscopy [30].

Imaging is increasingly being used to study models of brain metastasis. MRI allows for non-invasive, three-dimensional, longitudinal studies at very high spatial resolution and a wide range of contrast mechanisms are possible. Contrast-enhanced T1-weighted (T1w) MRI, which relies on tumor detection by diffusion of Gd across an impaired BBB in the local region of a tumor, is widely regarded as the most accurate method for clinical brain tumor detection. A previous imaging study performed in our laboratory showed that not all 231BR brain metastases were detectable after Gd-enhanced MRI and that the BBB permeability changed over time as brain metastases developed [24]. These findings suggest that brain metastases that are not permeable to Gd may go undetected by conventional MRI. In addition, heterogeneity in BBB permeability between metastases also means that therapeutic access to individual brain metastases varies [28, 30, 31].

In this study we explore the relationship between the growth of brain metastases and their permeability status in three HER2+ human brain metastatic breast cancer cell lines, two of which are HER2 expressing cell lines that have been recently developed. We present quantification of metastasis volume in the whole mouse brain using high resolution 3D MRI, as well as an assessment of the integrity of the BBB associated with each tumor (BTB). Correlative histology and immunohistochemistry provide image validation and further characterization of each cell line.

2.2 Methods

2.2.1 Cell Culture

The following three HER2+ human brain metastatic breast cancer cell lines were used: (1) MDA-MB-231-BR-HER2 [19], (2) JIMT-1-BR3 [32], (3) SUM190-BR3. The MDA-MB-231-BR-HER2 cell line is derived from the breast carcinoma parental line, MDA-MB-231, and transfected with HER2 [19]; the other two cell lines were derived from their parental lines – JIMT-1 [20] and SUM190 [33] respectively – and are HER2+. All three cells line were developed in the lab of Dr. Patricia Steeg at the National Cancer Institute (Bethesda, MA). For MDA-MB-231-BR-HER2 and JIMT-1-BR3, cells were maintained in Dulbecco's Modified Eagle Medium with 10% fetal bovine serum. MDA-MB-231-BR-HER2 media also contained penicillin and streptomycin; the JIMT-1-BR3 media contained 2mM glutamine. SUM190-BR3 cells were grown in serum-free Ham's F-12 medium supplemented with insulin and hydrocortisone. Culture media and supplements were purchased from Thermo Fisher Scientific (Mississauga, ON). All cell lines were maintained at 37°C and 5% CO₂. Cell viability was calculated by the trypan blue exclusion assay.

2.2.2 Cell Labeling

For a subset of *in vivo* experiments, cells were labeled with micron-sized iron oxide particles (0.9 μm MPIO, Bangs Laboratory, Fishers, IN) for cell tracking by MRI as previously described [21]. Labeling was achieved by co-incubating 2x10⁶ seeded cells with MPIO at a concentration of 25 μg Fe/mL for 24 hours in a T75cm² flask. The cells

were harvested and thoroughly washed three times with Hank's Balanced Salt Solution (HBSS) in order to remove unincorporated MPIO prior to cell injection. Perl's Prussian Blue (PPB) stained cytospin slides were analyzed to determine labeling efficiency; this was calculated in ImageJ software (Open-source, NIH, USA) as the ratio of PPB-positive cells to the total number of cells in five random fields of view at 40x magnification using a Zeiss AXIO Imager A1 Microscope.

Iron-labeled cells create regions of signal void on MR images [21, 23] and allow for the confirmation of successful cell injections and arrest of cancer cells in the brain; lack of signal voids results in exclusion from further study.

2.2.3 Animal Preparation

Female nude mice (nu/nu, aged 6-8 weeks from Charles River Laboratories, Wilmington, MA) were housed in a pathogen-free barrier facility and all experiments were approved by the Animal Use Subcommittee of the University Council on Animal Care at the University of Western Ontario. Cells suspended in 0.1mL of Hank's balanced salt solution were delivered to female nude mice, anesthetized with 2% isoflurane in oxygen, by intracardiac injection to the beating left ventricle of the mouse heart.

The three brain metastatic breast cancer models were injected intracardially into mice. The first group (n=5) was injected with 100,000 MDA-MB-231-BR-HER2 cells per mouse; another group of mice (n=6) was injected with 175,000 JIMT-1-BR3 cells; the final group (n=4) was injected with 500,000 SUM190-BR3 cells. The number of injected cells was selected based on *in vivo* tumorigenic potential determined from previous studies [28].

2.2.4 Experimental Endpoint

Mice were scanned using MRI at the experimental endpoint and then euthanized by an overdose injection of pentobarbital (Euthanyl). The endpoint was determined by the onset of neurological symptoms, unacceptable weight loss and body condition, or hind-limb paralysis. Different degrees of *in vivo* tumor growth and aggressiveness caused the

endpoint to be reached at different times for each model; this is further discussed in our results. The endpoints were day 28 for JIMT1-BR3, day 36 for MDA-MB-231-BR-HER2 and day 64 for SUM190-BR3.

2.2.5 Magnetic Resonance Imaging

All images were acquired on a 3.0T GE MR750 clinical scanner (General Electric, Mississauga, Canada), using a custom-built insertable gradient coil (inner diameter = 17.5cm, gradient strength = 500 mT/m, and peak slew rate = 3000 T/m/s) and a custom solenoidal mouse head radiofrequency (RF) coil (inner diameter = 1.5cm). Mice were anesthetized (1.5% isoflurane in oxygen) and temperature was maintained using warm saline bags during the scans. *In vivo* MRI was acquired using two pulse sequences: a three-dimensional bSSFP scan, and a two-dimensional post-Gd T1-weighted spin echo (T1wSE) scan.

The bSSFP sequence was used to detect signal voids post-cell injection on day 0, and to quantify metastases numbers and volumes in the whole mouse brain. The parameters for the bSSFP scans were as follows: resolution = 100 x 100 x 200 μm , repetition time = 8 or 10 ms, echo time = 4 or 5ms, flip angle = 35°, signal averages = 2, RF phase cycles = 8, scan time = 28 or 36 minutes. The T1wSE was acquired approximately 40 minutes after the intraperitoneal (ip) administration of 0.2mL gadopentetate dimeglumine (Magnevist, Schering, US; 0.5 mmol/mL) and used to assess the BTB associated with individual tumors. The parameters for these scans were as follows: resolution = 156 x 156 x 400 μm , repetition time = 600 ms, echo time = 20 ms, signal averages = 8, scan time = 20 minutes. Zero filling interpolation (ZIP) was applied to all images.

2.2.6 Histology and Immunohistochemistry

At respective endpoints, all mice were sacrificed by pentobarbital overdose and perfused with saline and subsequently with 4% paraformaldehyde or 4% formalin. Brains were excised and placed in paraformaldehyde for at least another 24h. Fixed brains were processed, paraffin-embedded and serially cut into 5 μm sections. Tissue sections were deparaffinized, rehydrated and either histologically stained with hematoxylin and eosin

(H&E) or stained for CD31, CD105 or ki67 by immunohistochemistry. Heat mediated antigen retrieval with citrate buffer pH6 was performed for sections that were to be stained for CD31 or Ki67. All tissue sections were blocked with Dako protein block, serum free (Dako Canada, Inc, Burlington, ON, Canada) and the following rabbit polyclonal antibodies were used: anti-CD31 (1:50, ab28364, Abcam Inc, Toronto, ON, Canada), anti-CD105 (1:1000, ab107595, Abcam Inc), anti-Ki67 (1:100, ab833, Abcam Inc). Dako LSAB2 system-HRP (Dako Canada Inc) and Vector DAB peroxidase substrate kit (Vector Laboratories, Burlingame, CA, USA) were used according to manufacturers' instructions to detect positive staining. All stained sections were counterstained with hematoxylin before dehydration and mounting. All staining was imaged on an Axio Imager A1 microscope (Zeiss CANADA, Toronto, ON, Canada) with a Retiga EXi (QImaging Scientific Research Cameras, Surrey, BC, Canada) digital camera.

2.2.7 Data Analysis

Images were analyzed using open-source OsiriX image software, version 3.9.2. Qualitative analysis of signal voids on day 0 confirmed mice with successful iron-labeled cell injections; lack of signal voids excluded mice from further study. Brain metastases were counted manually. 3D tumor volumes were reconstructed using the OsiriX volume algorithm from the manual segmentation of a ROI around each tumor boundary in every bSSFP image slice for each mouse. Comparison of corresponding bSSFP and T1wSE images were used to qualitatively assess BTB permeability to Gd – if metastases were detected on the T1wSE, these were classified as “Gd-permeable”; in contrast, if they were detected on the bSSFP but not in the corresponding T1wSE, these were deemed “Gd-impermeable”. If corresponding images were not available, permeability status was not decided. The “Gd-permeable fraction” was determined as the percentage of Gd-permeable metastases in relation to the total number of metastases in the whole brain at a specific time point. To evaluate the proliferative index of Gd-permeable and Gd-impermeable tumors, Ki67 stained tissue sections were matched to MRI data and imaged at 40x magnification; all nuclei within a random field of view in the tumor were manually counted. The proliferative index was calculated as the percent of Ki67-positively stained

nuclei among all MDA-MB-231-BR-HER2 cancer cells. All values are presented graphically as mean \pm SE. Statistical analysis was performed using unpaired t-tests, or a one-way analysis of variance followed by Tukey Honestly Significant Difference tests on GraphPad Prism version 6 software (GraphPad, San Diego, CA).

2.3 Results

Representative images of brain metastases from each group are shown in Figure 2.1. Contrast in bSSFP images is related to the ratio of spin-spin to spin-lattice relaxations (T_2/T_1); in general, metastases appear hyperintense compared to brain parenchyma due to relatively higher fluid content and therefore a longer T_2 and T_2/T_1 ratio.

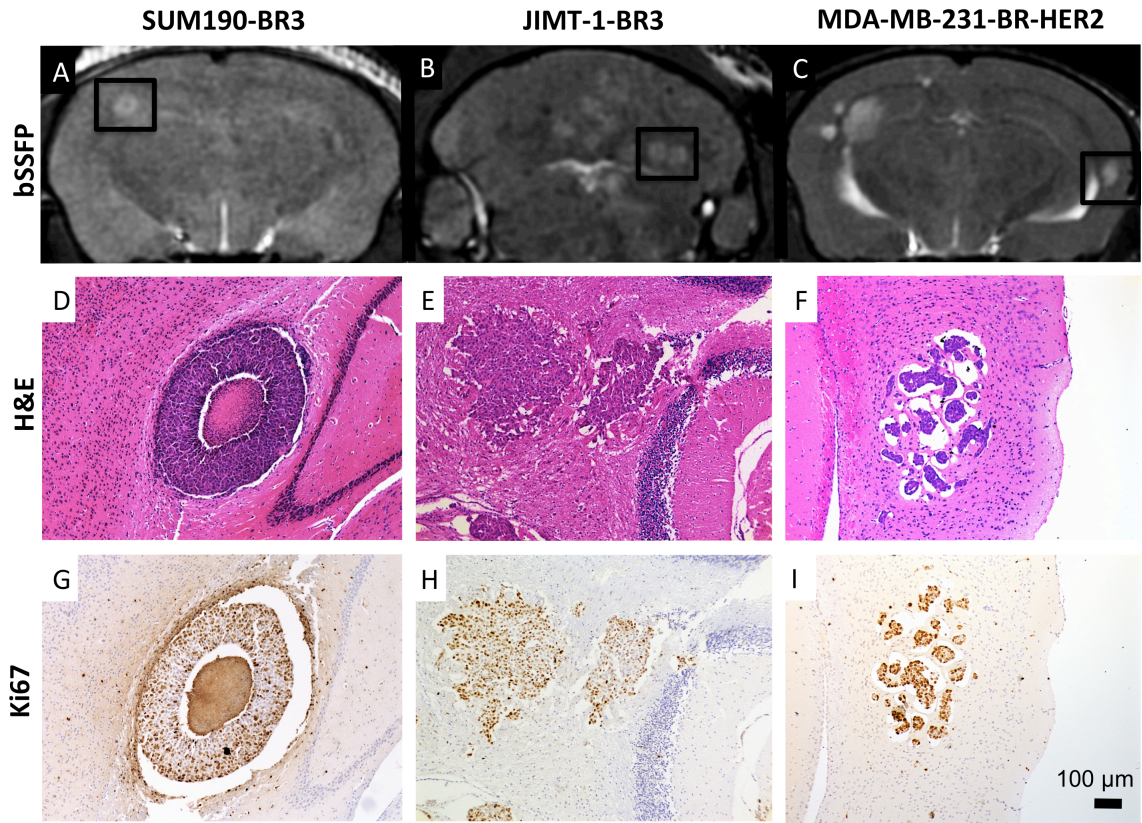


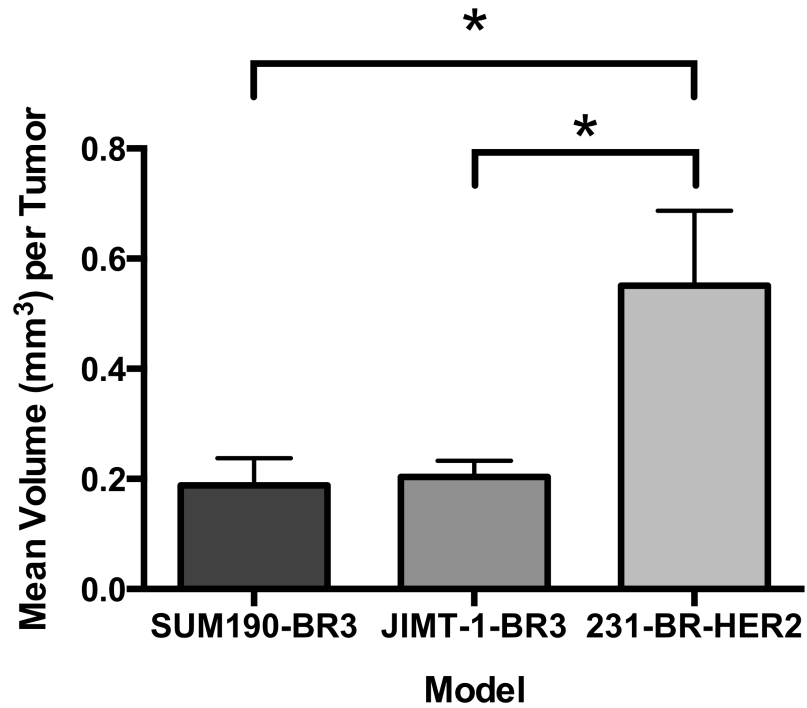
Figure 2.1: Representative images showing metastases resulting from SUM190-BR3, JIMT-1-BR3, or MDA-MB-231-BR-HER2 human brain metastatic breast cancer. (A-C) bSSFP images show metastasis burden (hyperintensities); (D-F) correlative H&E stained sections of the area indicated by boxes shows morphology of tumors in each model; (G-I) Ki67 staining indicates proliferative nuclei in brown. The region of signal void in the center of the SUM190-BR3 tumor (A) relates to the necrotic core seen in histology (D). JIMT-1-BR3 tumors are hyperintense in bSSFP (B) and grow as dense and proliferative nuclei clusters (E,H). 231-BR-HER2 tumors are the most hyperintense in bSSFP (C) and present as clusters of highly proliferative cell nuclei within pockets of edema in H&E (F,I).

The three models of HER2+ breast cancer brain metastasis each had a different appearance by MRI as well as in histology and immunohistochemistry. The SUM190-BR3 tumors were hyperintense with a hypointense core in bSSFP images (Figure 2.1A); this appearance was reflected in the corresponding H&E and Ki67 stained tissue sections where a necrotic core was evident (Figure 2.1D) and proliferation was evident around the outer edge (Figure 2.1G). The JIMT-1-BR3 tumors also appeared hyperintense in bSSFP images (Figure 2.1B) and tissue staining showed tumors with dense clusters of proliferative nuclei (Figure 2.1E,H). The MDA-MB-231-BR-HER2 tumors appeared the brightest in bSSFP images (Figure 2.1C). In H&E stained sections they present as small, dense clusters of cell nuclei surrounded by substantial pockets of edema (Figure 2.1F); Ki67 staining indicated these tumors were highly proliferative (Figure 2.1I).

The 3D high-resolution nature of MRI allowed us to quantify metastasis volume and permeability in the whole mouse brain for each animal in all three models. We evaluated 198 tumors at experimental endpoint across the three models. Tumor incidence and total tumor burden are shown in Table 2.1. The SUM190-BR3 model grew few tumors and the total tumor volume per brain was relatively low despite having the most cells injected. The MDA-MB-231-BR-HER2 model was injected with the least cells, yet grew the most tumors and had the highest total tumor volume. The study endpoint was decided when mice displayed clinical symptoms of the disease and deteriorating health. The time to endpoint was different for each model – day 28 for JIMT-1-BR3, day 36 for MDA-MB-231-BR-HER2, and day 64 for SUM190-BR3. The mean volume of each tumor was calculated at these times for all mice in each of the three models (Figure 2.2). The average volume of a tumor was significantly different between models [$F(2,12)=5.845$, $p<0.05$], but interestingly a longer experiment did not mean larger tumors. Post hoc Tukey tests showed that MDA-MB-231-BR-HER2 tumors were significantly larger in size compared to JIMT-1-BR3 or SUM190-BR3 tumors, despite the fact that the SUM190-BR3 model grew for longer. No significant difference in tumor volume was observed between JIMT-1-BR3 and SUM190-BR3 models, yet the SUM190-BR3 model grew for more than twice as long before the mice were noted to have neurological symptoms.

Table 2.1: Tumor incidence and burden at endpoint for each brain metastasis model. Number of tumors and total tumor volume is shown for each mouse, as well as average values and standard deviations within each model. Overall, SUM190-BR3 mice have the smallest tumor burden, and MDA-MB-231-BR-HER2 mice have the largest, both in terms of number of tumors and total tumor volume.

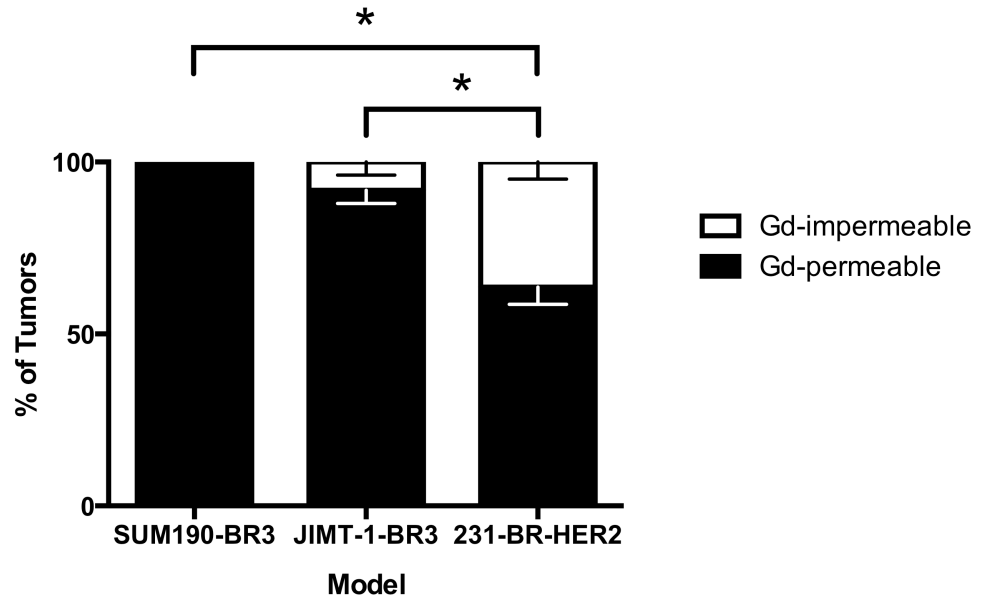
SUM190-BR3			JIMT-1-BR3			231-BR-HER2		
500,000 cells injected			175,000 cells injected			100,000 cells injected		
Mouse ID	# of Tumors	Total Tumor Volume (mm ³)	Mouse ID	# of Tumors	Total Tumor Volume (mm ³)	Mouse ID	# of Tumors	Total Tumor Volume (mm ³)
1	1	0.09	9	28	5.4	1	9	1.7
7	1	0.17	10	26	7.6	2	11	11
8	2	0.65	12	20	2.8	3	54	31
19	1	0.17	13	5	1.5	4	21	7.3
			15	8	1.1	5	7	4.7
			17	4	0.67			
Mean	1.25	0.2	Mean	15	3	Mean	20	11
SD	± 0.5	0.3	SD	± 11	3	SD	± 20	12



* Significantly different volume ($p < 0.05$)

Figure 2.2: Quantification of mean volume per tumor (\pm SEM) at endpoint in SUM190-BR3, JIMT-1-BR3 and MDA-MB-231-BR-HER2 models. The average volume of a tumor was significantly different between groups [$F(2,12)=5.845$, $p<0.05$] and MDA-MB-231-BR-HER2 tumors were significantly larger in size compared to JIMT-1-BR3 or SUM190-BR3 tumors. No other significant differences were observed.

The tumor permeability status for the three models is shown in Figure 2.3. A significant difference was observed in the percentage of Gd-permeable, or Gd-impermeable tumors between models [$F(2,12)=22.18, p<0.0001$]. Post hoc Tukey tests showed the MDA-MB-231-BR-HER2 had a significantly different proportion of Gd-permeable and Gd-impermeable tumors compared to the JIMT-1-BR3 or SUM190-BR3 models. All of the SUM-190-BR3 tumors and most JIMT-1-BR3 tumors were Gd-permeable, whereas only 63.6% of the MDA-MB-231-BR-HER2 tumors displayed BTB permeability to Gd. T1w SE post-Gd MR failed to detect 36.4% of MDA-MB-231-BR-HER2 metastases that were visible in bSSFP images. No other significant differences within or between groups were observed.



* Significantly different Gd-permeable and Gd-impermeable fractions ($p < 0.0001$)

Figure 2.3: Quantification of the mean percentage of Gd-permeable (black) and Gd-impermeable (white) tumors (\pm SEM). The percentage of Gd-permeable, or Gd-impermeable tumors was significantly different between groups [$F(2,12)=22.18$, $p<0.0001$]. All SUM190-BR3 and most JIMT-1-BR3 tumors were Gd-permeable, whereas only 63.6% of MDA-MB-231-BR-HER2 tumors display BTB permeability to Gd. Post hoc Tukey tests showed the MDA-MB-231-BR-HER2 had a significantly different proportion of Gd-permeable and Gd-impermeable tumors compared to the JIMT-1-BR3 or SUM190-BR3 models. No other significant differences in permeability were observed.

Figure 2.4 shows representative bSSFP and T1w post Gd images for a mouse with MDA-MB-231-BR-HER2 brain metastases. Three metastases were evident in the bSSFP image, yet only two of these were detectable in the T1wSE post-Gd. This suggested that the BTB associated with the third metastasis was intact.

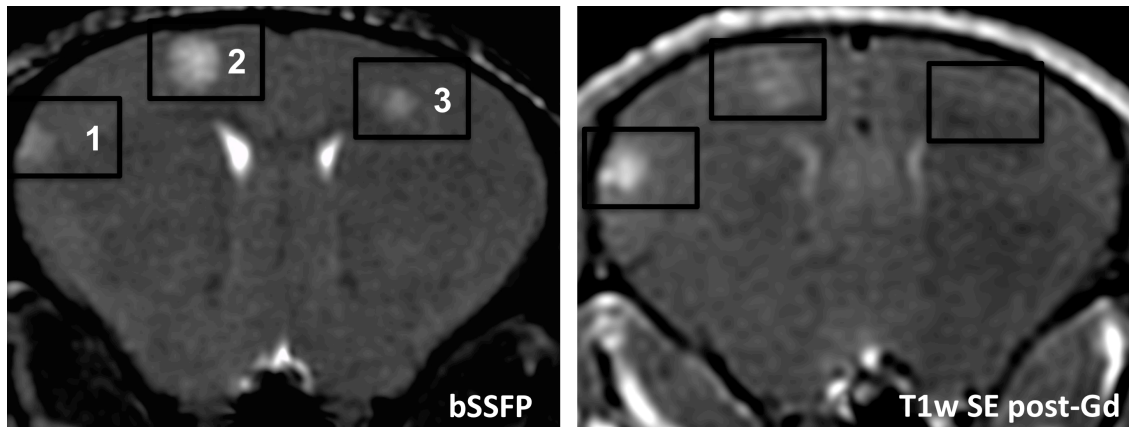
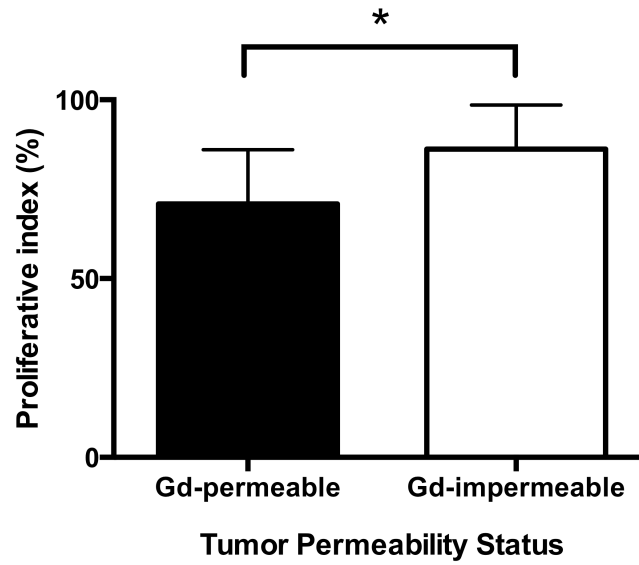


Figure 2.4: *In vivo* visualization of heterogeneous BTB permeability in the same animal. Axial MR images of the mouse brain; tumor burden is shown in the bSSFP image (left) and BTB permeability associated with the tumors is indicated in the T1w SE post-Gd (right). Three tumors are visualized in the bSSFP image, yet only two are detectable in the T1w SE post-Gd. This suggests that Gd cannot cross the BTB associated with tumor 3 and demonstrates the difference in tumor detection using contrast-enhanced MRI compared to the bSSFP sequence.

Immunohistochemistry was performed and evaluated, including CD31, CD105 and Ki67 stains, in an effort to understand factors that might relate to differences between Gd-permeable and Gd-impermeable tumors. Individual tumors in whole brain sections were identified as either Gd-permeable or Gd-impermeable by comparing to MRI. For this analysis, Gd-impermeable tumors were assessed only from the MDA-MB-231-BR-HER2 model, due to their low prevalence in the other models. Ki67 is a marker for proliferative nuclei and was used to calculate the mean proliferative index for Gd-permeable and Gd-impermeable brain metastases in the MDA-MB-231-BR-HER2 model. The proliferative index was determined as the percentage of positively stained nuclei among MDA-MB-231-BR-HER2 cells. The proliferative index for Gd-impermeable tumors was significantly higher than for Gd-permeable tumors [$t(24)=2.389$, $p<0.05$] (Figure 2.5).



* Significantly different proliferative index ($p < 0.05$)

Figure 2.5: The mean proliferation index (\pm SEM) for Gd-permeable and Gd-impermeable brain metastases in the MDA-MB-231-BR-HER2 model. This quantifies tumor proliferation by Ki67 staining and indicates there is a significantly more proliferative nuclei in Gd-impermeable compared to Gd-permeable brain metastases [$t(24)=2.389, p<0.05$].

CD31 is a marker for endothelial cells and CD105 marks proliferative endothelial cells. Together, these stains visualize vasculature patterns and can indicate where new vessels are being formed. This staining was only assessed qualitatively and it is interesting to note the different staining patterns across the three models. In the SUM190-BR3 model, CD31 staining was strongly localized to the outer edge of the tumor rim whereas CD105 staining was strongest on the inner edge of the tumor rim. This indicated the presence of vasculature around the tumor and new vasculature development inside, near the tumor core. The JIMT-1-BR3 and MDA-MB-231-BR-HER2 models had more similar patterns of CD31 and CD105 staining; the JIMT-1-BR3 model had existing and new vasculature dispersed throughout the tumor space while in MDA-MB-231-BR-HER2 tumors this appeared to be associated near areas of edema. Despite variance in vasculature patterns across the three models, no differences were observed between Gd-permeable and Gd-impermeable tumors (Figure 2.6).

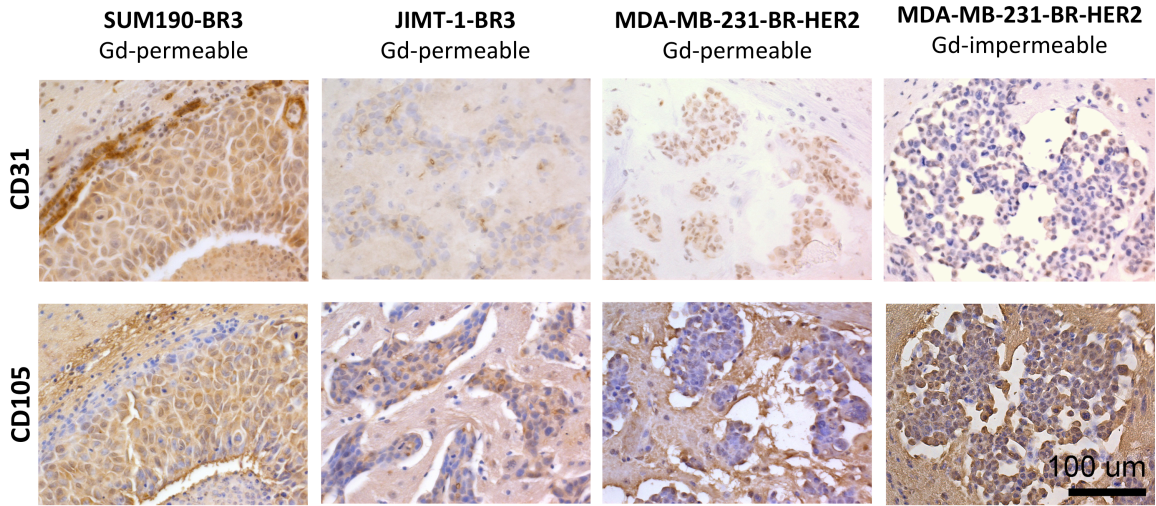


Figure 2.6: Representative images of CD31 (top) and CD105 (bottom) staining in SUM190-BR3, JIMT-1-BR3, and MDA-MB-231-BR-HER2 models. Staining patterns were qualitatively assessed for the distribution of endothelial cells and proliferative endothelial cells in tumor regions. Different staining patterns are evident between models; however, there is no obvious difference in the staining patterns between Gd-permeable and Gd-impermeable metastases within the MDA-MB-231-BR-HER2 model.

2.4 Discussion

In vivo MRI is a valuable tool for preclinical investigation of brain metastatic breast cancer and associated tumor permeability. In the current work, we used MRI to compare HER2+ brain metastases from the following three human breast cancer cell lines: (1) MDA-MB-231-BR-HER2 [19]; (2) JIMT-1-BR3 [32]; (3) SUM190-BR3. We show that there are differences in MRI appearance and permeability to Gd in three different types of HER2+ brain metastases. Furthermore, there is significant heterogeneity of this disease, which is reflected by marked differences in the tumor incidence, total tumor burden, and average size of a tumor in each of these models.

Our Gd-permeability analysis suggests that *in vivo* tumor permeability to Gd cannot be explained by lesion size, aggressiveness, or growth duration. Permeability to Gd indicates a disruption in the BBB, or BTB, when assessing brain tumors; this is important to understand because BBB disruption affects our ability to detect and treat brain metastases. Interestingly, models with smaller tumors – SUM190-BR3 and JIMT-1-BR3 – had significantly higher proportions of Gd-permeable tumors than the MDA-MB-231-BR-HER2 model, which had many Gd-impermeable metastases despite forming much larger metastases more quickly than the other models. Moreover, qualitative analysis of staining for endothelial cells (CD31) and proliferative endothelial cells (CD105) shows different vasculature patterns across different models of HER2+ brain metastatic breast cancer, but suggests no difference in development of new vasculature among Gd-permeable compared to Gd-impermeable tumors. This contradicts the dogma that large tumors have more neovasculature and are more ‘leaky’ [24, 34-36]. In addition to size, tumor aggressiveness does not explain permeability. Indeed, Gd-impermeable tumors in the MDA-MB-231-BR-HER2 model exhibited a significantly higher proliferative index than Gd-permeable tumors.

Our results align with preclinical studies by Lockman *et al.* [30] and Percy *et al.* [24] who have also demonstrated heterogeneity in the permeability status associated with brain metastases. Varying levels of passive permeability to Texas Red Dextran (3 kDa) or ¹⁴C-AIB (103 Da) were detected in MDA-MB-231-BR-HER2 metastases using *ex vivo*

fluorescence microscopy or autoradiography and it was found tumor permeability was not correlated with tumor size; in addition they suggest it is also unrelated to morphology or vascular density [30]. Percy *et al.* previously used the same *in vivo* MR imaging strategy used in our study and found Gd-permeable tumors were significantly larger than Gd-impermeable in the MDA-MB-231-BR model; however size alone was not sufficient to predict permeability [24]. Our work supplements these findings and further illustrates that tumor size and permeability are not directly related because models with smaller tumor size had higher proportions of Gd-permeable metastases. We demonstrate that tumor permeability is not the same in all models of HER2+ brain metastatic breast cancer.

The difference in permeability status across and within the models raises two important clinical implications. First, systemic therapies may be ineffective because they rely on diffusion of a therapeutic across an impaired BBB for delivery to metastases. Trastuzumab is part of the standard treatment for HER2+ metastatic breast cancer; however, this molecule does not adequately cross the BBB [37] and is ineffective for brain metastatic breast cancer [11, 12]. Interestingly, our study shows almost all SUM190-BR3 and JIMT-1-BR3 tumors are permeable to Gd. This molecule is much smaller (590Da) than trastuzumab (145kDa) and therefore may cross the BBB where size restrictions would exclude trastuzumab. Secondly, and perhaps more important is the fact that the population of potentially unresponsive metastases, due to limited drug uptake, are also not likely to be detected by current Gd-enhanced imaging strategies.

Importantly, it is possible for brain metastases to develop while maintaining an intact BBB. This may happen when tumors co-opt the pre-existing rich vasculature of the brain and develop alongside pre-existing microvessels [41-43]. In this situation, a large brain metastasis can develop with an intact BTB because the tumor grows around a pre-formed and properly constructed blood vessel. These tumors are radiographically invisible by Gd-enhanced MRI [41] because Gd does not extravasate from the intact blood vessel; however they are easily detectable in bSSFP images. The bSSFP sequence is advantageous to detect 'Gd-impermeable' tumors because it offers high spatial resolution

and contrast is related to the ratio of spin-spin to spin-lattice relaxations (T_2/T_1) – rather than extravasation of a contrast agent. This allows for the visualization of all brain metastases – regardless of the degree of BBB permeability. The bSSFP pulse sequence is available on clinical MRI systems, but has been predominantly used for cardiac applications [38]. Further investigation of this pulse sequence for brain metastatic evaluation is warranted to determine its clinical utility.

High-resolution MRI also allowed us to quantify the number and volume of metastases in the whole brain for every mouse in each model. We found marked differences in tumor incidence, total tumor burden, and appearance of metastases across the three models, despite the fact they are all meant to represent HER2+ brain metastatic breast cancer. The mean volume of MDA-MB-231-BR-HER2 metastases at endpoint was significantly larger than metastases in the JIMT-1-BR3 and SUM190-BR3 models. It is important to also consider the endpoint for each model to keep this result in context. The MDA-MB-231-BR-HER2 model is the most aggressive; it grows many large tumors, despite the least number of cells injected, and has a relatively short timeline with endpoint typically required by day 36. In comparison, the JIMT-1-BR3 model has a lesser tumor burden, grows significantly smaller metastases, yet endpoint is reached earlier at day 27/28. The SUM190-BR3 model grows tumors similar in size to the JIMT-1-BR3 model, but the total tumor burden is small and these animals can survive more than twice as long, to day 64.

In summary, the differences in appearance, number, volume, and permeability across the three models highlight significant heterogeneity in HER2+ brain metastatic breast cancer. Our findings have implications for both preclinical and clinical understanding of this disease. It is important to study new diagnostics and therapeutics in animal models that accurately reflect human disease and the heterogeneity presented here suggests a panel of different models may be necessary to adequately accomplish this. From a clinical standpoint, understanding the heterogeneity presented in this work will be important for improvements in detection strategies and delivery of therapeutic agents. This work emphasizes the need for personalized medicine; for example, if a patient has brain

metastases similar to the 231-BR-HER2 model, it could be assumed MRI is ‘blind’ to approximately one third of the total brain metastatic burden present in that patient and systemic therapies may not be effective against a large proportion of their disease; other treatment avenues, such as radiotherapy, might be pursued in this case.

3D MRI is a powerful tool to provide an *in vivo* comprehensive analysis of tumor incidence, tumor burden, and permeability status in preclinical models of HER2+ brain metastatic breast cancer. This information is challenging to obtain solely with *ex vivo* methods such as histology and immunohistochemistry, but it is important for understanding the natural heterogeneity present in experimental brain metastasis models. Understanding the disease heterogeneity presented here will be important for advancements in cancer diagnostics and therapy, and for improving patient management and survival.

2.5 References

1. Howlader N, Noone A, Krapcho M, Garshell J, Neyman N, Altekruse S, *et al.* SEER Cancer Statistics Review 1975-2010. Natl Cancer Inst.
2. Kennecke H, Yerushalmi R, Woods R, Cheang MCU, Voduc D, Speers CH, *et al.* Metastatic behavior of breast cancer subtypes. *J Clin Oncol* 2010;28:3271–7.
3. Ohno S, Ishida M, Kataoka A, Murakami S. Brain Metastasis of Breast Cancer. *Breast Cancer* 2004;11:27–9.
4. Sotiriou C, Pusztai L. Gene-expression signatures in breast cancer. *N Engl J Med* 2009;360:790–800.
5. Vanden Bempt I, Drijkoningen M, De Wolf-Peeters C. The complexity of genotypic alterations underlying HER2-positive breast cancer: an explanation for its clinical heterogeneity. *Curr Opin Oncol* 2007;19:552–7.
6. Holliday DL, Speirs V. Choosing the right cell line for breast cancer research. *Breast Cancer Res* 2011;13:215.
7. Niwińska A, Murawska M, Pogoda K. Breast cancer brain metastases: differences in survival depending on biological subtype, RPA RTOG prognostic class and systemic treatment after whole-brain radiotherapy (WBRT). *Ann Oncol* 2010;21:942–8.
8. Pestalozzi BC. Brain metastases and subtypes of breast cancer. *Ann Oncol* 2009;20:803–5.
9. Clayton AJ, Danson S, Jolly S, Ryder WDJ, Burt PA, Stewart AL, *et al.* Incidence of cerebral metastases in patients treated with trastuzumab for metastatic breast cancer. *Br J Cancer* 2004;91:639–43.

10. Slamon D, Leyland-Jones B, Shak S, Fuchs H, Paton V, Bajamonde A, *et al.* Use of Chemotherapy Plus a Monoclonal Antibody Against HER2 for Metastatic Breast Cancer that Overexpresses HER2. *N Engl J Med* 2001;344:783–92.
11. Bendell JC, Domchek SM, Burstein HJ, Harris L, Younger J, Kuter I, *et al.* Central nervous system metastases in women who receive trastuzumab-based therapy for metastatic breast carcinoma. *Cancer* 2003;97:2972–7.
12. Lai R, Dang CT, Malkin MG, Abrey LE. The risk of central nervous system metastases after trastuzumab therapy in patients with breast carcinoma. *Cancer* 2004;101:810–6.
13. Shmueli E, Wigler N, Inbar M. Central nervous system progression among patients with metastatic breast cancer responding to trastuzumab treatment. *Eur J Cancer* 2004;40:379–82.
14. Stemmler HJ, Kahlert S, Siekiera W, Untch M, Heinrich B, Heinemann V. Characteristics of patients with brain metastases receiving trastuzumab for HER2 overexpressing metastatic breast cancer. *Breast* 2006;15:219–25.
15. Deeken JF, Löscher W. The blood-brain barrier and cancer: transporters, treatment, and Trojan horses. *Clin Cancer Res* 2007;13:1663–74.
16. Connell JJ, Chatain G, Cornelissen B, Vallis KA, Hamilton A, Seymour L, *et al.* Selective permeabilization of the blood-brain barrier at sites of metastasis. *J Natl Cancer Inst* 2013;105:1634–43.
17. Rye PD, Norum L, Olsen D-R, Garman-Vik S, Kaul S, Fodstad O. Brain metastasis model in athymic nude mice using a novel MUC1-secreting human breast-cancer cell line, MA11. *Int J Cancer* 1996;68:682–7.
18. Yoneda T, Williams PJ, Hiraga T, Niewolna M, Nishimura R. A bone-seeking clone exhibits different biological properties from the MDA-MB-231 parental

- human breast cancer cells and a brain-seeking clone in vivo and in vitro. *J Bone Miner Res* 2001;16:1486–95.
19. Palmieri D, Bronder JL, Herring JM, Yoneda T, Weil RJ, Stark AM, *et al.* Her-2 overexpression increases the metastatic outgrowth of breast cancer cells in the brain. *Cancer Res* 2007;67:4190–8.
 20. Tanner M, Kapanen AI, Junttila T, Raheem O, Grenman S, Elo J, *et al.* Characterization of a novel cell line established from a patient with Herceptin-resistant breast cancer. *Mol Cancer Ther* 2004;3:1585–92.
 21. Heyn C, Ronald JA, Ramadan SS, Snir JA, Barry AM, MacKenzie LT, *et al.* In vivo MRI of cancer cell fate at the single-cell level in a mouse model of breast cancer metastasis to the brain. *Magn Reson Med* 2006;56:1001–10.
 22. Fitzgerald DP, Palmieri D, Hua E, Hargrave E, Herring JM, Qian Y, *et al.* Reactive glia are recruited by highly proliferative brain metastases of breast cancer and promote tumor cell colonization. *Clin Exp Metastasis* 2008;25:799–810.
 23. Ribot EJ, Martinez-Santesteban FM, Simecra C, Steeg PS, Chambers AF, Rutt BK, *et al.* In vivo single scan detection of both iron-labeled cells and breast cancer metastases in the mouse brain using balanced steady-state free precession imaging at 1.5 T. *J Magn Reson Imaging* 2011;34:231–8.
 24. Percy DB, Ribot EJ, Chen Y, McFadden C, Simecra C, Steeg PS, *et al.* In vivo characterization of changing blood-tumor barrier permeability in a mouse model of breast cancer metastasis: a complementary magnetic resonance imaging approach. *Invest Radiol* 2011;46:718–25.
 25. Perera M, Ribot EJ, Percy DB, McFadden C, Simecra C, Palmieri D, *et al.* In Vivo Magnetic Resonance Imaging for Investigating the Development and

- Distribution of Experimental Brain Metastases due to Breast Cancer. *Transl Oncol* 2012;5:217–25.
26. Kil WJ, Cerna D, Burgan WE, Beam K, Carter D, Steeg PS, *et al.* In vitro and in vivo radiosensitization induced by the DNA methylating agent temozolomide. *Clin Cancer Res* 2008;14:931–8.
 27. McGowan PM, Simeone C, Ribot EJ, Foster PJ, Palmieri D, Steeg PS, *et al.* Notch1 inhibition alters the CD44^{hi}/CD24^{lo} population and reduces the formation of brain metastases from breast cancer. *Mol Cancer Res* 2011;9:834–44.
 28. Taskar KS, Rudraraju V, Mittapalli RK, Samala R, Thorsheim HR, Lockman J, *et al.* Lapatinib distribution in HER2 overexpressing experimental brain metastases of breast cancer. *Pharm Res* 2012;29:770–81.
 29. Gril B, Palmieri D, Bronder JL, Herring JM, Vega-Valle E, Feigenbaum L, *et al.* Effect of lapatinib on the outgrowth of metastatic breast cancer cells to the brain. *J Natl Cancer Inst* 2008;100:1092–103.
 30. Lockman PR, Mittapalli RK, Taskar KS, Rudraraju V, Gril B, Bohn KA, *et al.* Heterogeneous blood-tumor barrier permeability determines drug efficacy in experimental brain metastases of breast cancer. *Clin Cancer Res* 2010;16:5664–78.
 31. Morikawa A, Peereboom DM, Thorsheim HR, Samala R, Balyan R, Murphy CG, *et al.* Capecitabine and lapatinib uptake in surgically resected brain metastases from metastatic breast cancer patients: a prospective study. *Neuro Oncol* 2014:1–7.
 32. Palmieri D, Duchnowska R, Woditschka S, Hua E, Qian Y, Biernat W, *et al.* Profound Prevention of Experimental Brain Metastases of Breast Cancer by

- Temozolomide in an MGMT-Dependent Manner. *Clin Cancer Res* 2014;20:2727–39.
33. Forozan F, Veldman R, Ammerman CA, Parsa NZ, Kallioniemi A, Kallioniemi O, *et al.* Molecular cytogenetic analysis of 11 new breast cancer cell lines. *Br J Cancer* 1999;81:1328–34.
 34. Zhang R, Price JE, Fujimaki T, Bucana CD, Fidler IJ. Differential Permeability of the Blood-Brain Barrier in Experimental Brain Metastases Produced by Human Neoplasms Implanted into Nude Mice. *Am J Pathol* 1992;141:1115–24.
 35. Strugar J, Rothbart D, Harrington W, Criscuolo G. Vascular permeability factor in brain metastases: correlation with vasogenic brain edema and tumor angiogenesis. *J Neurosurg* 1994;81:560–6.
 36. Thorsen F, Fite B, Mahakian LM, Seo JW, Qin S, Harrison V, *et al.* Multimodal imaging enables early detection and characterization of changes in tumor permeability of brain metastases. *J Control Release* 2013;172:812–22.
 37. Stemmler H-J, Schmitt M, Willems A, Bernhard H, Harbeck N, Heinemann V. Ratio of trastuzumab levels in serum and cerebrospinal fluid is altered in HER2-positive breast cancer patients with brain metastases and impairment of blood-brain barrier. *Anticancer Drugs* 2007;18:23–8.
 38. Sung K, Lee H-L, Hu HH, Nayak KS. Prediction of myocardial signal during CINE balanced SSFP imaging. *Magn Reson Mater Phys* 2010; 23(2):85-91.
 39. Pastel DA, Mamourian AC, Duhaime A-C. Internal structure in pineal cysts on high-resolution magnetic resonance imaging: not a sign of malignancy. *J Neurosurg Pediatr* 2009;4(1):81–4.
 40. Xie T, Zhang X-B, Yun H, Hu F, Yu Y, Gu Y. 3D-FIESTA MR images are useful in the evaluation of the endoscopic expanded endonasal approach for midline skull-base lesions. *Acta Neurochir* 2011;153(1):12–8.

41. Leenders WPJ, Küsters B, Verrijp K, Ku B, Maass C, Wesseling P, *et al.* Antiangiogenic Therapy of Cerebral Melanoma Metastases Results in Sustained Tumor Progression via Vessel Antiangiogenic Therapy of Cerebral Melanoma Metastases Results in Sustained Tumor Progression via Vessel Co-Option. *Clin Cancer Res* 2004;10:6222–30.
42. Döme B, Hendrix MJC, Paku S, Tóvári J, Tímár J. Alternative vascularization mechanisms in cancer: Pathology and therapeutic implications. *Am J Pathol* 2007;170:1–15.
43. Donnem T, Hu J, Ferguson M, Adighibe O, Snell C, Harris AL, *et al.* Vessel co-option in primary human tumors and metastases: an obstacle to effective anti-angiogenic treatment? *Cancer Med* 2013;2:427–36.

Chapter 3

3 Evaluating changes to blood-brain barrier integrity in brain metastasis over time and after radiation treatment

Introduction: The incidence of brain metastasis due to breast cancer is increasing and prognosis is poor. Treatment is challenging because the blood-brain barrier (BBB) limits efficacy of systemic therapies. In this work, we develop a clinically relevant whole brain radiotherapy (WBRT) plan to investigate the impact of radiation on brain metastasis development and BBB permeability in a murine model. We hypothesize that radiotherapy will decrease tumor burden and increase tumor permeability, which could offer a mechanism to increase drug uptake in brain metastases. **Methods:** Contrast-enhanced MRI and high resolution anatomical MRI was used to evaluate BBB integrity associated with brain metastases due to breast cancer in the MDA-MB-231-BR-HER2 model during their natural development. Novel image-guided micro-irradiation technology was employed to develop WBRT treatment plans and to investigate if this altered brain metastatic growth or permeability. Histology and immunohistochemistry was performed on whole brain slices corresponding with MRI to validate and further investigate radiological findings. **Results:** Herein, we show successful implementation of micro-irradiation technology that can deliver WBRT to small animals. We further report WBRT following diagnosis of brain metastasis can mitigate, but not eliminate, tumor growth in the MDA-MB-231-BR-HER2 model. Moreover, radiotherapy did not impact BBB permeability associated with metastases. **Conclusions:** Clinically relevant WBRT is not curative when delivered after MRI-detectable tumors have developed in this model. A dose of 20 Gy/2 was not sufficient to increase tumor permeability such that it could be used as a method to increase systemic drug uptake in brain metastasis.

3.1 Introduction

The relative five-year survival for breast cancer patients has steadily increased and was recently reported at 90% in the United States [1]. Now, the major challenge of this disease is its ability to metastasize to distant sites where detection and therapy become

complicated. The incidence of metastasis to the brain is especially high for women with breast cancer that overexpresses HER2 and has been reported at 25 – 48 % [2–4]. More concerning is that brain metastases often manifest while metastases outside of the brain are still responding to successful anti-HER2 therapies, such as trastuzumab (Herceptin®). Several factors may be involved in this type of mixed response, including: the unique microenvironment of the brain, neuro-inflammation, and genetic alterations distinct from the primary tumor [5, 6]. Notably, the inability of traditional systemic therapies to penetrate the intact BBB to any significant degree, or at all, presents a significant obstacle for drug delivery, thus rendering the brain a sanctuary site for metastatic growth [7, 8].

In the absence of effective systemic therapy, treatment options for patients with brain metastases are limited; they include steroids, surgical excision of solitary metastases, SRS for small lesions not amenable to surgery, and WBRT. While combinations of these options has improved prognosis, the median survival time of patients with HER2+ breast cancer is only 11.5-16.5 months after diagnosis of brain metastasis [9]. The clinical standard for treating multiple (e.g. > 3 lesions detected by MRI) brain metastases and diffuse disease is WBRT; however, this treatment is palliative. Response to treatment may be improved by optimizing the timing of radiotherapy in combination with systemic therapies. Some studies suggest that radiation can increase vascular permeability within tumors and in healthy brain tissue through initiation of endothelial cell apoptosis [10, 11]. If WBRT increases permeability of the local BBB *in vivo*, it may be possible to increase drug uptake in brain metastases and improve on the results of systemic therapy or radiotherapy alone [12].

Several contrast agents with varying sizes have been used to assess BBB integrity and degree of permeability. Under normal conditions, the intact BBB prevents extravasation of contrast agents. Damage to the BBB can therefore be evaluated based on the size, charge, and composition of contrast agents that are able to cross the BBB and accumulate in the brain. Traditionally BBB permeability has been studied by microscopy using agents such as sodium fluorescein (376 Da), Texas Red Dextran (3 or 70 kDa), horseradish peroxidase (44 kDa), or albumin-bound Evans blue dye (69 kDa) [8, 10, 13–15]. These

techniques are limited by their *ex vivo* nature, inability to monitor changes over time, and contrast agent sizes that are not directly relevant to drug uptake. In this work, we evaluate BBB integrity *in vivo* over time using Gd-enhanced MRI, which is routinely used in clinical diagnosis to identify BBB breakdown.

Gd-enhanced MRI has also been used in preclinical cancer models to evaluate BBB permeability associated with brain tumors [14, 16–19]. Regions where the BBB has been compromised can be visualized due to local accumulation of the Gd contrast agent, which results in signal enhancement (brightness) in the image. Using this method, substantial heterogeneity has been reported in the permeability of brain metastases. In addition, both Gd-permeable as well as Gd-impermeable tumors have been observed within the same brain [17, 19]. Notably, Percy and colleagues also found that many metastases were impermeable to Gd early in development, but became permeable over time [17]. Here, we build on these results by investigating whether radiation therapy increases the permeability of brain metastases, to understand if it is possible to open a window where systemic therapy could have increased efficacy.

In this study, we developed a clinically relevant WBRT treatment protocol that is feasible in the MDA-MB-231-BR-HER2 experimental brain metastatic breast cancer model. We used this model along with contrast enhanced MRI and high resolution anatomical MRI to investigate the impact of clinically relevant radiation treatment on the growth of brain metastases due to breast cancer and on BBB integrity in a murine model. We hypothesized that radiotherapy will decrease the tumor burden in treated animals and increase tumor permeability.

3.2 Methods

3.2.1 Cell Culture

The brain metastatic breast cancer cells (MDA-MB-231-BR-HER2) used in this research were a kind gift from Dr. Patricia Steeg's laboratory at the National Cancer Institute (Bethesda, MA) [20, 21]. Cells were grown in Dulbecco's Modified Eagle Medium with 10% fetal bovine serum, 1% penicillin and streptomycin, and were maintained at 37°C

and 5% CO₂. Culture media and supplements were purchased from Thermo Fisher Scientific (Mississauga, ON). The cell line was tested for mycoplasma contamination using the MycoAlert Mycoplasma Detection Kit (Lonza, Rockland, ME, USA) and was found to be negative. The trypan blue exclusion assay was used to determine cell viability.

3.2.2 Animal Preparation

Female nude mice (nu/nu, aged 6-8 weeks from Charles River Laboratories, Wilmington, MA, USA) were housed in a pathogen-free barrier facility at Robarts Research Institute. All experiments were approved by the Animal Use Subcommittee of the University Council on Animal Care at the University of Western Ontario. Mice (n=2 for commissioning, n=12 for WBRT experiment) were anesthetized with 2% isoflurane in oxygen, and given an intracardiac injection of 100,000 MDA-MB-231-BR-HER2 cells suspended in 0.1mL of HBSS. Mice were euthanized by an overdose injection of pentobarbital (Euthanyl) after the final imaging session.

3.2.3 Radiotherapy

We previously developed an integrated micro-CT/RT system capable of sophisticated image-guided conformal small animal radiotherapy [22]. The micro-irradiation technology is based on a modified preclinical micro-CT system (GE eXplore CT 120, GE Healthcare, Milwaukee, WI, USA) with an upgraded x-ray generator (140 kVp, 50 kW), custom irradiation control software (Parallax-Innovations, London, ON, Canada), and a custom-built computer-controlled collimator. Thus far, it had been used for respiratory-gated rat lung irradiation and was commissioned for mouse WBRT in this work [22, 23]. Mice were anesthetized (1.5% isoflurane in oxygen), placed feet first prone on the rodent couch, and aligned using set up lasers and CT imaging. On-board fluoroscopy was used to identify the skull and position computerized collimators such that the whole brain was targeted for irradiation and the remainder of the head and body were shielded. Animal temperature was maintained using a heating pad and breathing rate was monitored during treatment.

3.2.4 Magnetic Resonance Imaging

Magnetic resonance images were acquired on a 3.0 T GE MR750 clinical scanner (General Electric, Mississauga, ON, Canada), using a custom-built gradient insert coil (inner diameter = 17.5cm, gradient strength = 500 mT/m, and peak slew rate = 3000 T/m/s). Mice were anesthetized (1.5% isoflurane in oxygen) and placed in a custom solenoidal mouse head radiofrequency (RF) coil (inner diameter = 1.5cm). Animal temperature was maintained using warm saline bags during imaging. Anatomical bSSFP scans were acquired with the following parameters: spatial resolution = 100 x 100 x 200 μm , repetition time = 8 ms, echo time = 4 ms, flip angle = 35°, signal averages = 2, radiofrequency phase cycles = 8, scan time = 29 minutes. ZIP2 and ZIP512 upscaling were applied. Post-Gd T1-weighted spin echo (T1w SE) images were acquired at approximately 45 minutes after an ip injection of 0.2mL gadopentetate dimeglumine (Magnevist, 0.5 mmol/mL). The parameters were: spatial resolution = 156 x 156 x 400 μm , repetition time = 600 ms, echo time = 20 ms, signal averages = 8, scan time = 20 minutes. ZIP512 upscaling was applied.

3.2.5 Data Analysis

Open-source OsiriX image software (version 3.9.2) was used for image analysis. Brain metastases were counted and the boundaries of each were manually segmented using the ROI tool in every bSSFP slice throughout the whole mouse brain. Tumor volume was then calculated by a 3D reconstruction using the Osirix volume algorithm. Enhancing fraction (reflecting Gd-permeable tumors) was determined as previously described by comparing tumor detection in corresponding post-Gd T1w SE and bSSFP images [17, 19]. Metastases that are detected in both the post-Gd T1w SE and the bSSFP sequences are considered ‘enhancing’; tumors appearing in only the bSSFP images are ‘non-enhancing’. Tumors detected in bSSFP without a corresponding T1w SE image slice were excluded from the enhancement analysis.

Statistical analysis was performed using GraphPad Prism version 6.0 software (GraphPad, San Diego, CA, USA). Where two groups were compared, two-way paired or unpaired Students t-tests were performed. Where two groups were compared over

multiple time points, two-way repeated measures analysis of variance (ANOVA) were performed. For enhancement-related statistical analyses over time, one untreated mouse was removed due to unsuccessful injection on day 32, therefore repeated measures was not used for this analysis. *Post hoc* analysis included Sidak's multiple comparisons tests.

3.2.6 Histology and Immunohistochemistry

At experimental endpoint, mice were first perfused with 0.9% saline before perfusion fixation with 4% formalin; brains were then excised, further fixed for 24 hours by immersion in 4% formalin, processed, paraffin-embedded, cut into 5- μ m sections, and stained with hematoxylin and eosin (H&E) for morphology, or stained by IHC for the proliferation marker Ki67, or human mitochondria (clone MTCO2). Briefly, Ki67 staining was achieved on selected brain sections using heat mediated antigen retrieval with citrate buffer pH6. Tissue sections were blocked with Dako protein block, serum free (Dako Canada, Inc, Burlington, ON, Canada) and incubated with anti-ki67 (1:100, ab833, Abcam Inc) rabbit polyclonal antibodies. Positive staining was detected using Dako LSAB2 system-HRP (Dako Canada Inc) and Vector DAB peroxidase substrate kit (Vector Laboratories, Burlingame, CA, USA) according to manufacturer's instructions. Mouse anti-human mitochondria antibody (clone MTCO2, 1:100) was used with the Dako Animal Research Kit according to manufacturer's instructions for detection of human cells. All sections were counterstained with hematoxylin.

For commissioning studies, mice were perfused with 0.9% saline before perfusion fixation with 4% paraformaldehyde; brains were excised, further fixed for 24 hours by immersion in 4% formalin, placed in ascending sucrose gradients (10%, 20%, 30%), embedded in optimal cutting temperature compound (Tissue-Tek, Sakura, Torrance, CA, USA), frozen, cryosectioned with 10 μ m thickness and stained by IHC for γ -H2AX using the Ford protocol [24]. Sections were incubated with mouse anti- γ -H2AX antibody (1:700, anti-phospho-histone H2AX, Ser139, clone JBW301; Millipore, Billerica, MA, USA) overnight and the stained with secondary antibody Alexa-Fluoro 594 goat anti-mouse IgG (1:500, Life Technologies, Carlsbad, CA, USA) for one hour at room temperature. All sections were counterstained with DAPI (4', 6-diamidino-2-

phenylindole) and mounted with anti-fade medium Vectashield (Vector Laboratories, Inc. Burlington, ON, Canada).

All staining was imaged on an Axio Imager A1 microscope (Zeiss CANADA, Toronto, ON, Canada) with a Retiga EXi (QImaging Scientific Research Cameras, Surrey, BC, Canada) digital camera. Whole brain histology images were acquired using the TISSUEScope 4000 (Huron Digital Pathology, Waterloo, ON, Canada). For γ -H2AX confocal images, an inverted confocal microscope (Olympus Fluoview FV1000 Confocal Imaging System) was used.

3.3 Results

3.3.1 Radiation Therapy Planning and Verification

First, the integrated micro-CT/RT system used in this research was implemented for mouse WBRT. A treatment plan of 20 Gy in two fractions on consecutive days was implemented based on the biological effective dose (BED) to tumor (assuming $\alpha/\beta=10$ Gy) to be equivalent to the clinical WBRT dose fractionation scheme of 30Gy/10. Image guidance allowed for precise isolation of the mouse brain in a collimated 10x14-mm field; fluoroscopy images show the uncollimated field (Figure 3.1A) and collimated field (Figure 3.1B). The brain was irradiated with two identical fields using a parallel-opposed beam set-up. One beam was delivered from the animal's left-right direction and one from right-left, for a cumulative dose of 10 Gy per fraction. A Monte Carlo dose verification calculation was performed to confirm delivery of the treatment plan (10 Gy is shown by a green line) (Figure 3.1C). Mean dose rate was 0.12 ± 0.01 Gy per minute.

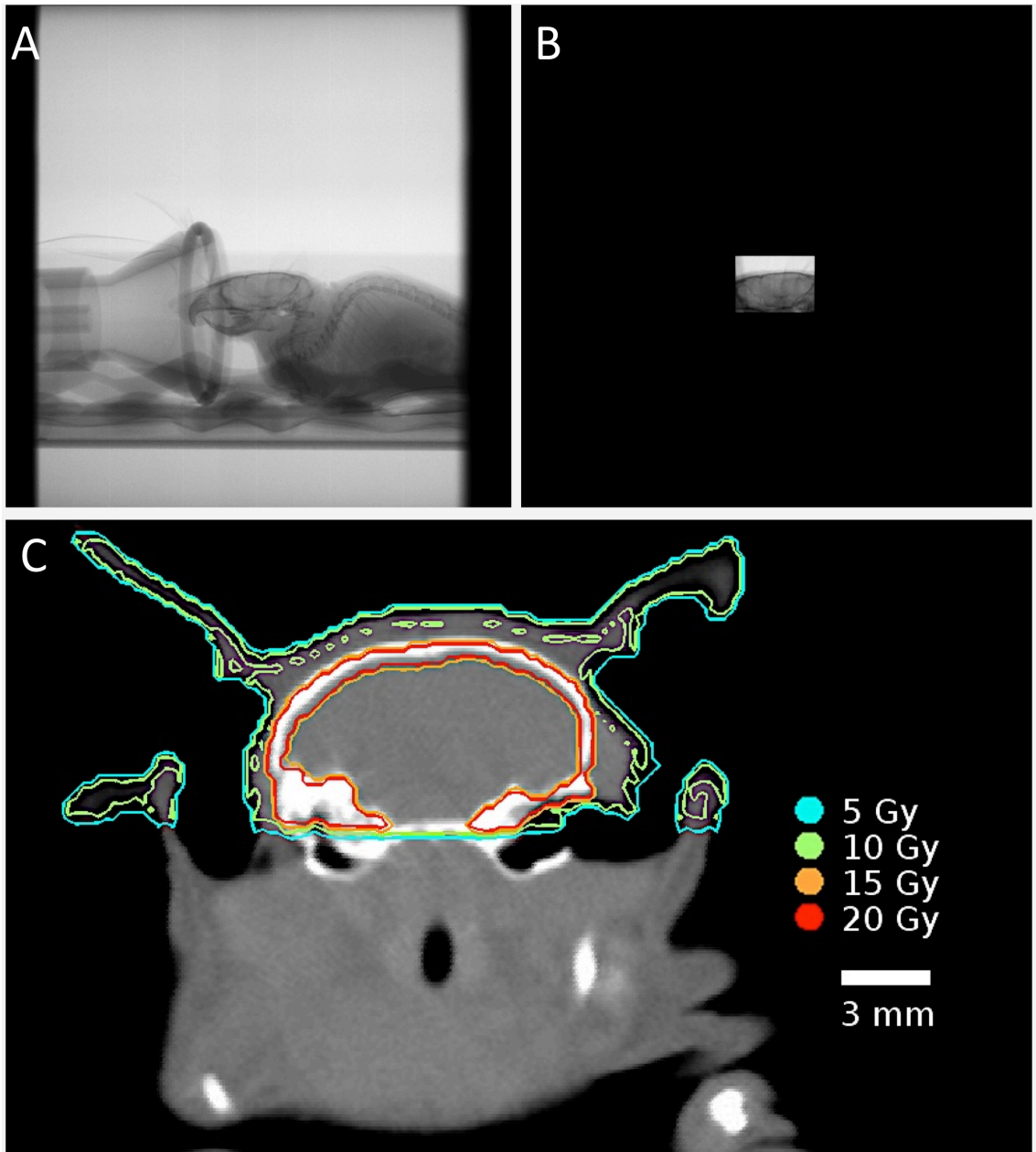


Figure 3.1: Micro-CT/RT targeting for mouse WBRT. Fluoroscopy-guided collimation of the mouse brain (A, B) allows for precise delivery of the 10Gy per fraction treatment plan. Dosimetry was verified using a Monte Carlo dose calculation, where the 10-Gy isodose line is delineated in green (C). The brain received a uniform dose of 10 Gy. Enhanced dose to the skull is observed due to the low energy of the beam (140kV) where photoelectric effect is prominent.

Immunohistochemistry was performed after irradiation to confirm adequate whole brain coverage by the radiotherapy plan. Irradiation-induced DNA damage response was verified by fluorescent γ -H2AX immunohistochemistry and the DAPI nuclear stain; this confirmed the actual whole brain radiation field in tissue. Whole brain sections bearing MDA-MB-231-BR-HER2 metastases were imaged with a fluorescent microscope at 10x magnification; these showed no damage to un-irradiated mouse brain (Figure 3.2A) and confirmed homogeneous γ -H2AX response to radiation-induced DNA double stranded breaks (DSB, red foci) across the whole treated mouse brain 30 minutes after the second fraction of 20Gy/2 (Figure 3.2B). Intrinsic DNA DSB response was evaluated in 100x magnification images of tumor tissue and normal brain of an un-irradiated mouse (Figure 3.2C,D) and compared with initial DNA DSB response in a mouse brain 30 minutes post-irradiation (Figure 3.2E,F). Increased γ -H2AX intensity is evident in both tumor and normal brain tissue in the mouse brain treated with WBRT compared to untreated. Confocal microscopy confirms accumulation of γ -H2AX within the nuclei of tumor cells. While few intrinsic γ -H2AX foci are present in nuclei of un-irradiated tumor cells (Figure 3.2G), they are highly prevalent in response to DNA DSB at 30 minutes post-irradiation (Figure 3.2H).

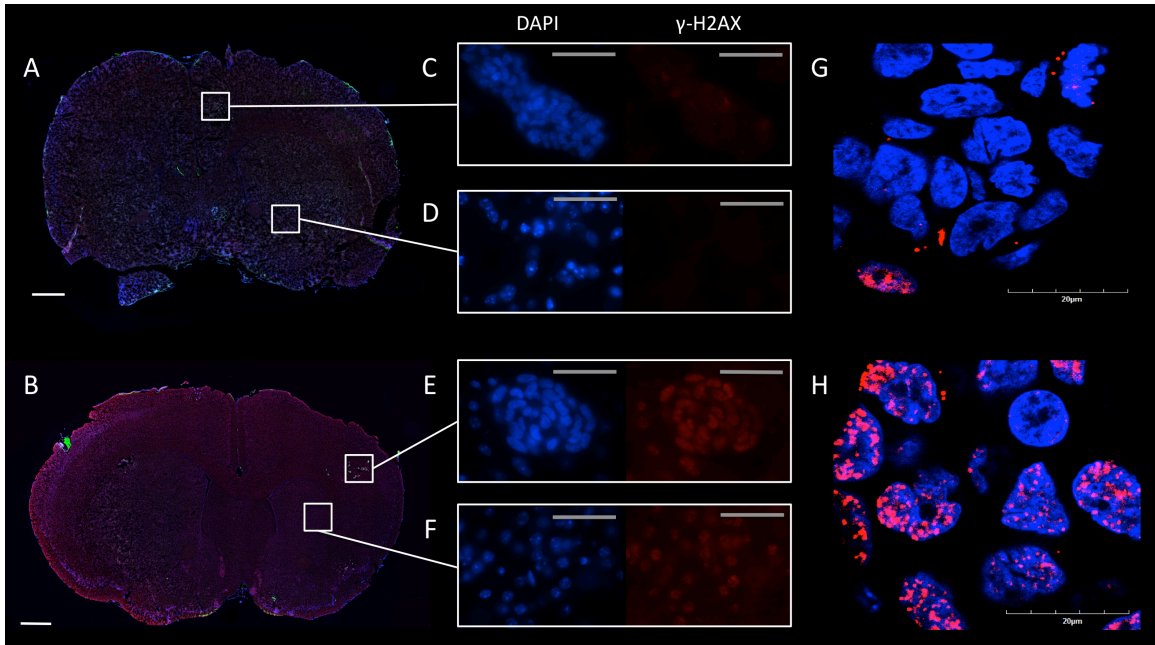


Figure 3.2: Response to radiation-induced DNA DSB was visualized by fluorescent γ -H2AX immunohistochemistry. This staining was performed 30 minutes post-radiotherapy with fluorescent γ -H2AX (red foci) on a nuclear DAPI background (blue) on whole brain sections of untreated (A) and WBRT-treated (B) mouse brain. Magnified images of untreated tumor (C) and normal brain (D) showed minimal γ -H2AX signal intensity compared to irradiated tumor (E) and irradiated normal brain (F). Confocal microscopy illustrated the accumulation of γ -H2AX was within the nuclei of tumor cells; untreated nuclei had few intrinsic γ -H2AX foci (G) and treated nuclei had many γ -H2AX foci in response to radiation-induced DNA DSB. Scale bars are 750 micron (A,B), 50 micron (C-F), and 20 micron (G,H).

Brain sections were also assessed at endpoint (day 36 post cell injection) to confirm imaging results, evaluate proliferation in tumors, and verify human status of the developing cancer (Figure 3.3). Hyperintense regions in the MRI (Figure 3.3A) corresponded to tumor regions as assessed by morphology in standard H&E histology (Figure 3.3B, E). Ki67 staining of neighboring sections indicated that the detected tumors were proliferative (Figure 3.3C, F). Staining for human mitochondria also confirmed the metastases were of human origin (Figure 3.3D, G). The histology and immunohistochemistry therefore validate that the MRI findings in this study reflect cancerous growth due to the injected MDA-MB-231-BR-HER2 cell line.

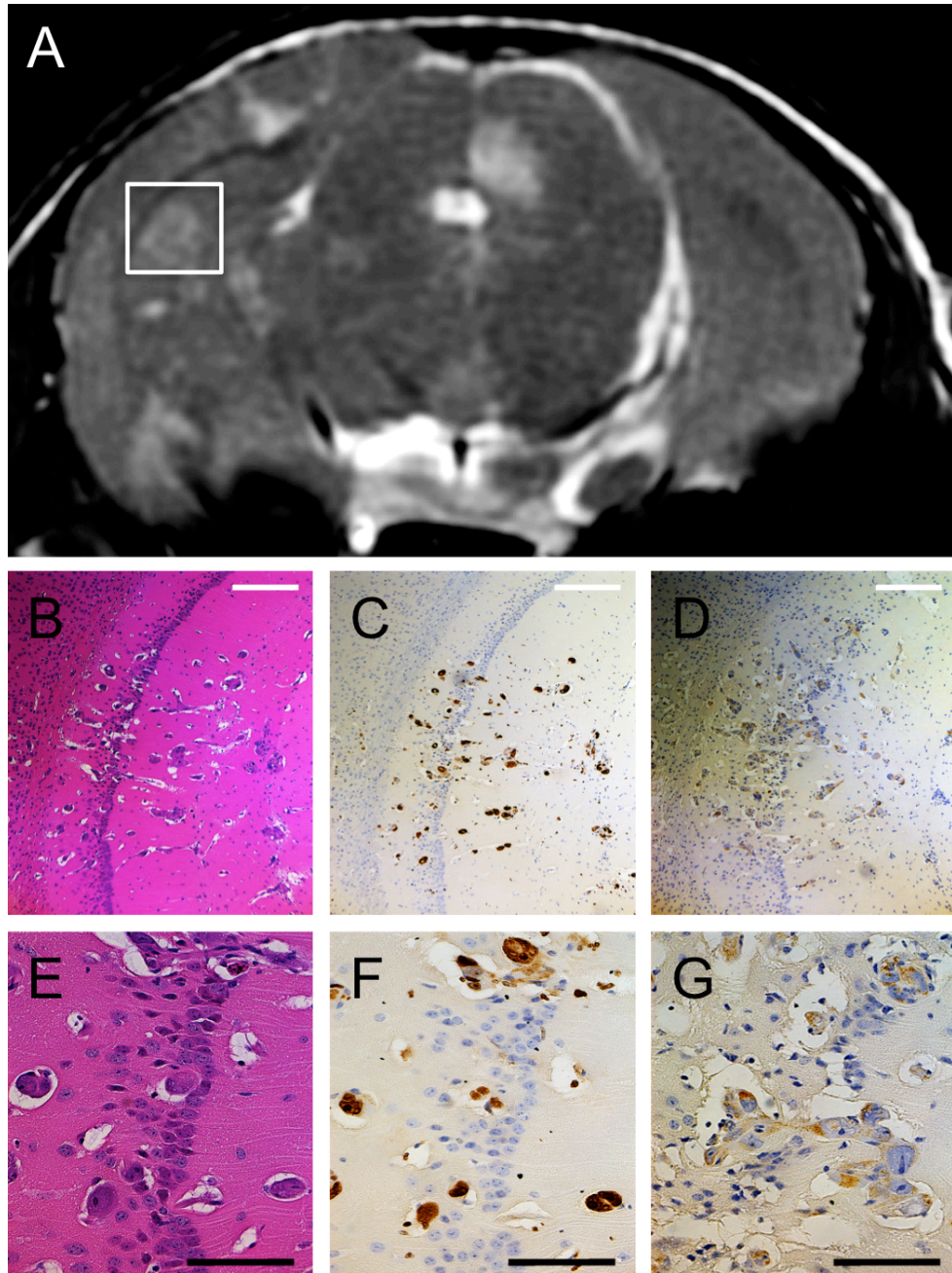


Figure 3.3: Representative MRI with correlative histology and immunohistochemistry of metastases in the MDA-MB-231-BR-HER2 brain metastasis model. Staining for H&E (B, E), Ki67 (C, F), and human mitochondria (D, G) at 10x magnification (B-D, white scale bar = 250 μ m) and 40x magnification (E-G, black scale bar = 100 μ m) supports the imaging data and confirmed MRI-detected lesions were proliferative cancerous tumors of human origin.

3.3.2 WBRT Experiment

Next, the micro-CT/RT system was used to deliver WBRT (20Gy/2) to nude mice with brain metastatic breast cancer. Treatment was delivered when mice developed small MRI-detectable brain tumors (day 24 and 25 post-cell injection); this timing mimics the usual treatment following diagnosis that occurs in the clinic. Three dimensional, high-resolution anatomical bSSFP MRI was used to detect and monitor tumor progression over time. Radiological findings correspond well with tumor burden in whole brain histology sections (Figure 3.4).

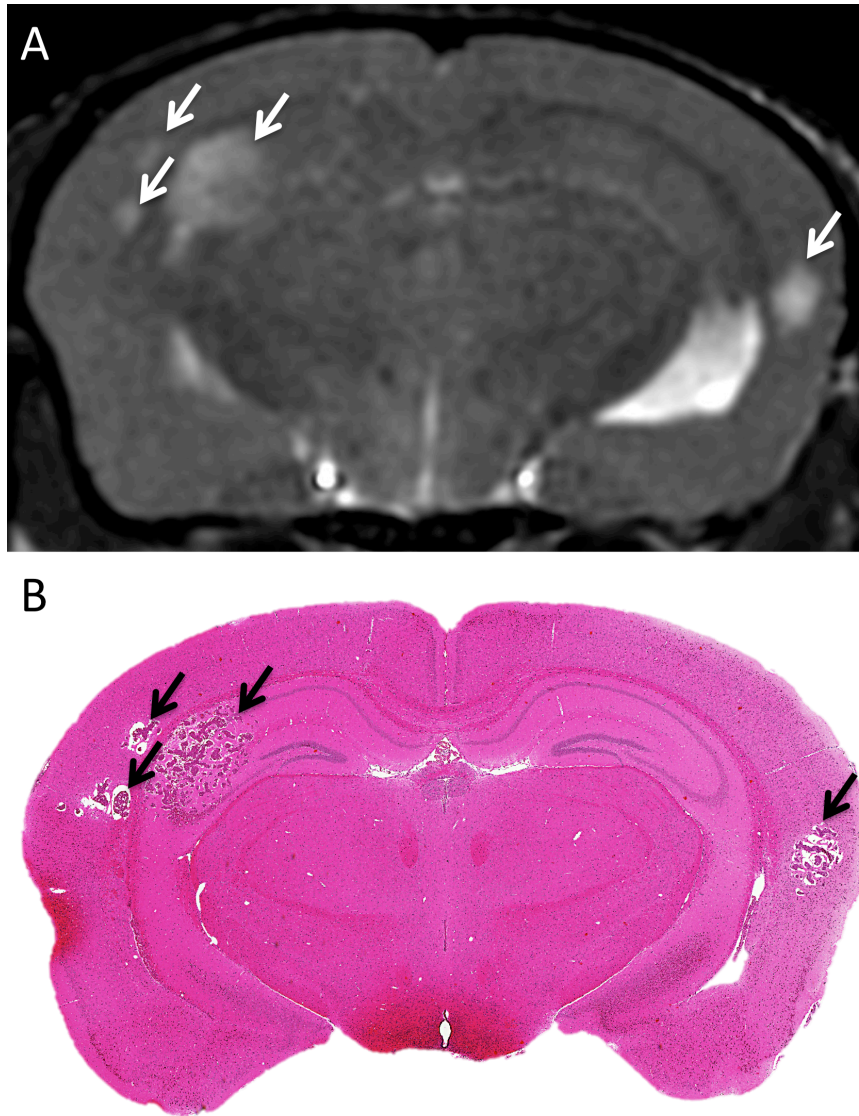


Figure 3.4: Representative images of metastases due to MDA-MB-231-BR-HER2 human brain metastatic breast cancer on day 36. bSSFP MRI illustrated metastasis burden by the appearance of hyperintensities (A) and this corresponded with tumor detection in H&E stained sections (B).

The number of tumors, total tumor volume, and mean tumor volume over time (day 23, 32, 36) were quantified in bSSFP images and these data are presented in Table 3.1. WBRT did not have an effect on the number of tumors, nor total tumor volume over time, however, it did have an effect on the mean volume of a tumor over time ($p < 0.01$); *post hoc* analysis found mean tumor volume was significantly less in WBRT-treated mice than untreated ($p < 0.001$).

Table 3.1: Quantification tumor incidence, burden, and mean tumor volume from MRI in the traditional WBRT experiment. The number of tumors and total tumor volume in the mouse brain increased over time from day 23 to 36, but there was no difference between treatment groups for these measurements. Traditional WBRT had a significant effect on mean tumor volume over time; *post hoc* analysis between groups indicated that by day 36, on average, tumors were smaller in treated mice compared to untreated. Data are presented as mean \pm SD. N=6 for each group.

Analysis	Day 23		Day 32		Day 36		Main effect
	<i>untreated</i>	<i>WBRT</i>	<i>untreated</i>	<i>WBRT</i>	<i>untreated</i>	<i>WBRT</i>	
Number of Tumors	7.0 \pm 11	25 \pm 29	17 \pm 19	34 \pm 33	18 \pm 19	34 \pm 33	time $p < 0.0001$
Total Tumor Volume (mm ³)	0.26 \pm 0.41	0.98 \pm 1.4	4.9 \pm 5.8	8.3 \pm 9.8	9.8 \pm 11	8.4 \pm 9.3	time $p < 0.01$
Mean Tumor Volume (mm ³)	0.030 \pm 0.022	0.035 \pm 0.014	0.33 \pm 0.18	0.23 \pm 0.067	0.67 \pm 0.40	0.23 \pm 0.059	interaction between time and treatment $p < 0.01$

Substantial variability was observed in tumor response after WBRT. The changes in volume of 209 treated tumors were analyzed between 7 and 11 days post-treatment (day 32 and 36). A paired two-tailed t-test found no significant difference between the fraction of tumors that decreased in volume after WBRT compared to the fraction that increased (Figure 3.5A). Furthermore, despite the same treatment plan, some mice had more tumors that decreased in volume after radiotherapy than others. For example, as shown in Figure 3.5B, 85% of the brain tumors in mouse B had a decreased volume after WBRT whereas only 15% of the tumors in mouse E had a decreased volume after WBRT.

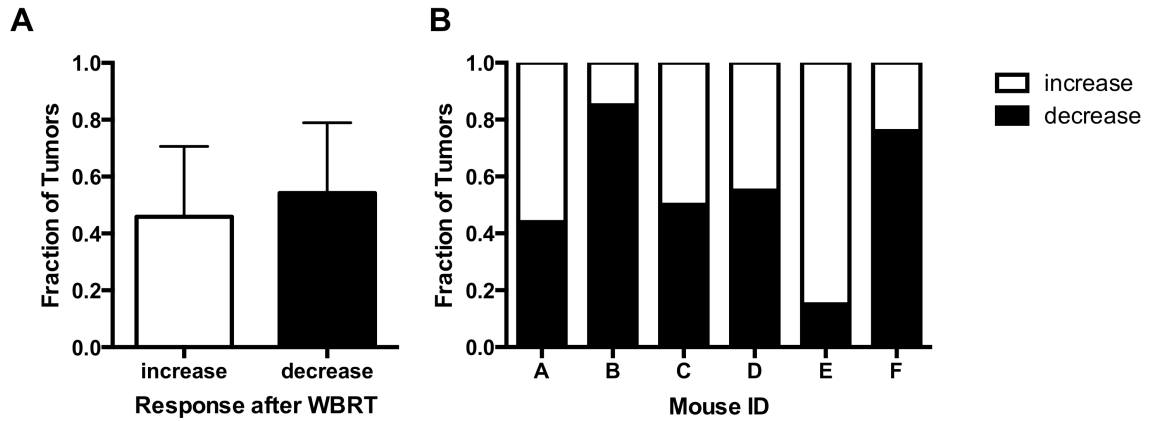


Figure 3.5: Treatment response was heterogeneous after traditional WBRT. There was no significant difference between the fraction of tumors that decreased in volume after traditional WBRT and the fraction that continued to increase (A). In addition, the response to therapy was markedly different for each mouse, ranging from 15 - 85% of the tumors in a mouse brain being reduced in tumor volume following treatment (B). Error bars are standard deviation.

Next, BBB integrity was evaluated by determining the ability for Gd to accumulate within tumors and cause increased signal intensity (enhancement). Analysis of BBB permeability by enhancement in T1w SE post-Gd images was performed as previously described and representative MR image slices of the same mouse brain are shown in Figure 3.6A,B [17, 19]. The enhancing fraction over time is shown in Figure 3.6C. Over time, a higher proportion of enhancing metastases are detectable in both groups ($p < 0.0001$). Of the non-enhancing tumors present in untreated mice (black bars) on day 32, 29% (9 of 31) changed to enhancing by day 36. Similarly, 26% (6 of 23) of non-enhancing tumors in WBRT mice (white bars) changed to enhancing in the same time frame. WBRT did not increase the fraction of enhancing tumors.

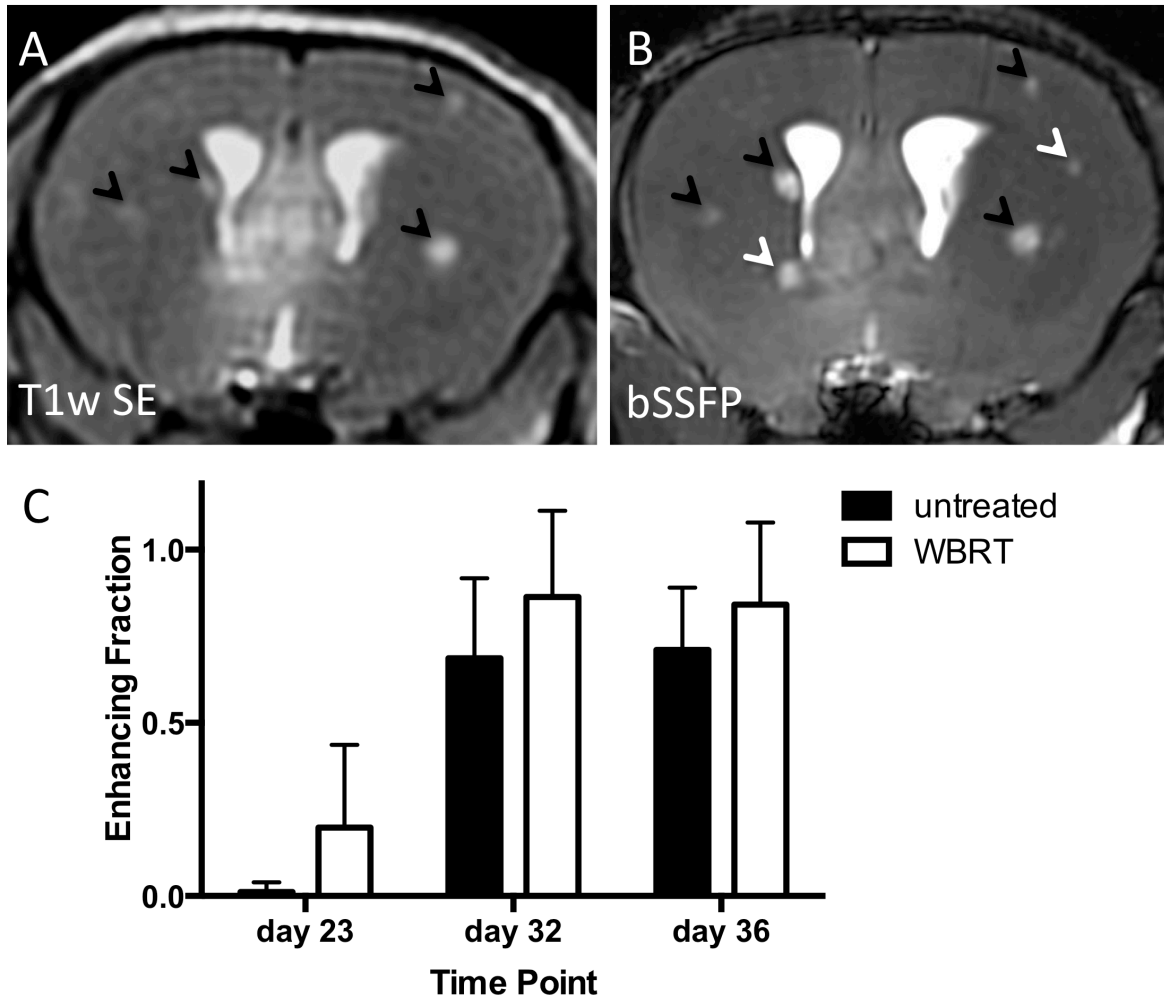


Figure 3.6: Tumor permeability visualized and quantified over time by contrast-enhanced MRI. Enhancing fraction (representing Gd-permeable tumors) was quantified as the number of enhancing tumors relative to total tumor burden by assessment of T1w SE post-Gd (A) and bSSFP images (B). Black arrows indicate metastases that were detected in both the T1w SE and the bSSFP sequences; these were considered ‘enhancing’. White arrows indicate metastases that were detected in the bSSFP image but were absent in the corresponding post-Gd T1w SE image; these were considered ‘non-enhancing’. Over time, the enhancing fraction increased in both groups; treatment did not have any significant effect ($p > 0.05$) (C). Error bars represent standard deviation.

Temporal analysis of enhancement status and mean tumor volume (Figure 3.7) found enhancing tumors grow larger than non-enhancing tumors over time in both untreated and WBRT-treated groups ($p < 0.001$, $p < 0.01$ respectively). *Post hoc* analysis found that enhancing tumors are significantly larger than non-enhancing on day 32 and 36 in both groups (untreated: $\bullet\bullet p < 0.05$, $\bullet p < 0.0001$. WBRT: $\circ\circ p < 0.0001$, $\circ p < 0.0001$). Radiotherapy affected the growth of enhancing and non-enhancing tumors differently (Figure 3.7, striped vs. solid bars). Over time, WBRT had an increased effect on the size of enhancing tumors ($p < 0.01$); *post hoc* analysis between treatment groups showed that the mean volume of enhancing tumors is significantly less in WBRT treated mice compared to untreated on day 36 ($*p < 0.0001$). Contrarily, time and treatment group did not affect the volume of non-enhancing tumors.

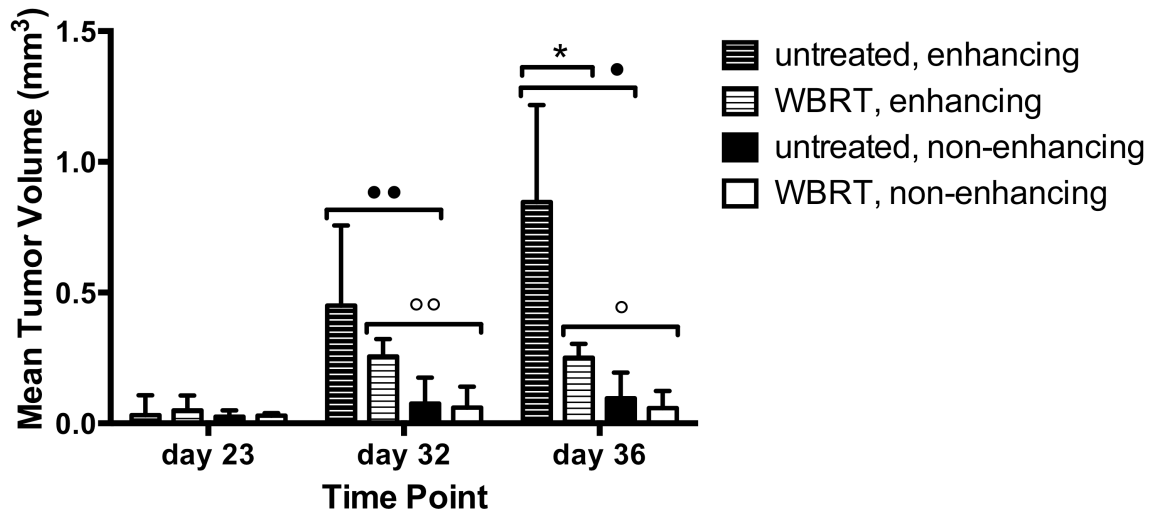


Figure 3.7: Enhancing and non-enhancing tumors respond differently to WBRT. In both untreated and WBRT-treated mice, enhancing tumors were larger than non-enhancing tumors at day 32 and at day 36 (statistical significance indicated by ••, •, °°, °). By day 36, the mean volume of an enhancing tumor in a treated mouse was significantly less than untreated (*); however, there was no difference between groups in the volume of non-enhancing tumors. Error bars represent standard deviation.

3.4 Discussion

This research used high-resolution anatomical and contrast-enhanced MRI in a murine model of breast cancer brain metastasis to monitor tumor development and permeability *in vivo*. This was combined with novel image-guided micro-irradiation technology to provide insight into the responses of tumors and alternations in BBB integrity in a clinically relevant model of breast cancer brain metastasis and WBRT.

A micro-CT/RT system with asymmetrical computerized jaws was successfully applied to deliver mouse whole brain irradiation. These are the first experiments where such a system has been used to demonstrate the effects of WBRT on brain metastatic development. This technology has the capacity to target and deliver conformal irradiation to the mouse brain via onboard image-guided collimation. Post-irradiation, γ -H2AX staining confirmed response to radiation-induced DNA DSB was present and was uniform across the whole mouse brain. Dose rate was low compared to other preclinical irradiators; however, doses up to 20 Gy per fraction can be delivered in one session, and increased dose can compensate for the lower dose rate [25, 26]. Here, we chose 20 Gy/2 to keep side effects at a minimum while delivering biological effective doses that are relevant for WBRT.

Using this small animal irradiation system, traditional WBRT was given after MRI detected tumors; this sequence, where treatment follows diagnosis, is the usual order of events in the clinic. WBRT was able to mitigate tumor growth, though it could not eliminate the tumor burden. Similar results were reported by Smart and colleagues who observed that fractionated (3 Gy x 10 fractions, starting on day 14 post-injection) or single dose (15 Gy x 1 fraction on day 14) radiotherapy could reduce, but not eliminate, the number of large and micrometastases in the 231-BR experimental brain metastasis model [27]. In our study, the largest contributor to the drop in mean tumor volume of treated animals was a decrease in the mean volume of enhancing tumors. On the contrary, non-enhancing tumor volumes, though significantly less by comparison, were not different between treatment groups. Increased BBB permeability with tumor size, in addition to innate BBB heterogeneity, has been reported by several groups and

investigated for its impact on systemic drug delivery [8, 17, 18, 28, 29]. However, to the best of our knowledge, this is the first report indicating that impermeable tumors may not respond to radiotherapy in the same way as their permeable counterparts.

Increased vascular permeability and BBB disruption after irradiation have been well documented [10, 11, 30]. This stimulated the idea that radiotherapy may be a useful mechanism to improve chemotherapeutic efficacy by increasing drug uptake through breakdown of the BBB, which is usually prohibitively exclusive to anti-cancer drugs. Yet, clinical studies investigating combinations of chemo- and radiotherapy remain inconclusive [31–33]. Previous studies may have offered poor insight due to limitations by their *in vitro* or *ex vivo* nature, non-translational animal models, and irradiation doses that are not clinically relevant [10, 11]. Moreover, no study has looked at these effects in the context of brain metastasis. Our study addresses all of these limitations; we used MRI tumor enhancement post-Gd administration to assess tumor permeability *in vivo* and found that the fraction of enhancing tumors was not different between treated and untreated mice at any time point. Furthermore, the percent of tumors that change from non-enhancing to enhancing was similar after WBRT compared to untreated. Notably, tumor enhancement post-Gd administration reflects sufficient BBB permeability to allow the 590 Da Gd-based contrast agent to cross; this is approximately the same molecular weight as lapatinib (581 Da), a dual tyrosine kinase inhibitor used in combination therapy for HER2+ metastatic breast cancer patients. Taskar and colleagues previously reported limited BBB permeability in the vast majority of brain metastases contributed to poor therapeutic efficacy for this drug [28]. Our study, using Gd as a permeability marker, did not find a suitable mechanism to increase tumor permeability. Our results suggest that increased BBB permeability due to clinically relevant radiotherapy, as measured by enhancement post-Gd administration, is not present at one week, or 11 days post-WBRT as was previously hypothesized [12]. Moreover, the idea that radiotherapy can increase BBB permeability and thereby improve drug delivery is not feasible in this model.

In summary, this research developed technology for image-guided mouse WBRT and used it with high resolution anatomical and contrast-enhanced MRI to investigate tumor

and BBB response after radiotherapy in a mouse model of breast cancer brain metastasis. Contrary to previous hypotheses, increased tumor permeability after radiotherapy was not found, although enhancing tumors decreased in volume after radiotherapy and non-enhancing tumors did not.

3.5 References

1. Siegel R, Ma J, Zou Z, Jemal A. Cancer Statistics, 2014. *CA Cancer J Clin* 2014;64:9–29.
2. Clayton AJ, Danson S, Jolly S, Ryder WDJ, Burt PA, Stewart AL, *et al.* Incidence of cerebral metastases in patients treated with trastuzumab for metastatic breast cancer. *Br J Cancer* 2004;91:639–43.
3. Bendell JC, Domchek SM, Burstein HJ, Harris L, Younger J, Kuter I, *et al.* Central nervous system metastases in women who receive trastuzumab-based therapy for metastatic breast carcinoma. *Cancer* 2003;97:2972–7.
4. Lai R, Dang CT, Malkin MG, Abrey LE. The risk of central nervous system metastases after trastuzumab therapy in patients with breast carcinoma. *Cancer* 2004;101:810–6.
5. Lin NU, Amiri-Kordestani L, Palmieri D, Liewehr DJ, Steeg PS. CNS Metastases in Breast Cancer: Old Challenge, New Frontiers. *Clin Cancer Res* 2013;19:6404–18.
6. Brastianos PK, Carter SL, Santagata S, Cahill DP, Jones RT, Van Allen EM. Genomic Characterization of Brain Metastases Reveals Branched Evolution and Potential Therapeutic Targets. *Cancer Discov* 2015;5:1164–77.
7. Stemmler H-J, Schmitt M, Willems A, Bernhard H, Harbeck N, Heinemann V. Ratio of trastuzumab levels in serum and cerebrospinal fluid is altered in HER2-positive breast cancer patients with brain metastases and impairment of blood-brain barrier. *Anticancer Drugs* 2007;18:23–8.
8. Lockman PR, Mittapalli RK, Taskar KS, Rudraraju V, Gril B, Bohn KA, *et al.* Heterogeneous blood-tumor barrier permeability determines drug efficacy in experimental brain metastases of breast cancer. *Clin Cancer Res* 2010;16:5664–78.

9. Hayashi N, Niikura N, Masuda N, Takashima S, Nakamura R, Watanabe K, *et al.* Prognostic factors of HER2-positive breast cancer patients who develop brain metastasis: a multicenter retrospective analysis. *Breast Cancer Res Treat* 2015;149:277–84.
10. Li Y, Chen P, Haimovitz-friedman A, Reilly RM, Wong CS. Endothelial Apoptosis Initiates Acute Blood–Brain Barrier Disruption after Ionizing Radiation. *Cancer Res* 2003; 63:5950–6.
11. Fauquette W, Amourette C, Dehouck M-P, Diserbo M. Radiation-induced blood-brain barrier damages: an in vitro study. *Brain Res* 2012;1433:114–26.
12. van Vulpen M, Kal HB, Taphoorn MJB, El-Sharouni SY. Changes in blood-brain barrier permeability induced by radiotherapy: implications for timing of chemotherapy? *Oncol Rep* 2002;9:683–8.
13. Zhang R, Price JE, Fujimaki T, Bucana CD, Fidler IJ. Differential Permeability of the Blood-Brain Barrier in Experimental Brain Metastases Produced by Human Neoplasms Implanted into Nude Mice. *Am J Pathol* 1992;141:1115–24.
14. Connell JJ, Chatain G, Cornelissen B, Vallis KA, Hamilton A, Seymour L, *et al.* Selective permeabilization of the blood-brain barrier at sites of metastasis. *J Natl Cancer Inst* 2013;105:1634–43.
15. Yen LF, Wei VC, Kuo EY, Lai TW. Distinct Patterns of Cerebral Extravasation by Evans Blue and Sodium Fluorescein in Rats. *PLoS One* 2013;8:1–9.
16. Song H-T, Jordan EK, Lewis BK, Liu W, Ganjei J, Klaunberg B, *et al.* Rat model of metastatic breast cancer monitored by MRI at 3 tesla and bioluminescence imaging with histological correlation. *J Transl Med* 2009;7:88.
17. Percy DB, Ribot EJ, Chen Y, McFadden C, Simeanea C, Steeg PS, *et al.* In vivo characterization of changing blood-tumor barrier permeability in a mouse model

- of breast cancer metastasis: a complementary magnetic resonance imaging approach. *Invest Radiol* 2011;46:718–25.
18. Thorsen F, Fite B, Mahakian LM, Seo JW, Qin S, Harrison V, *et al.* Multimodal imaging enables early detection and characterization of changes in tumor permeability of brain metastases. *J Control Release* 2013;172:812–22.
 19. Murrell DH, Hamilton AM, Mallett CL, van Gorkum R, Chambers AF, Foster PJ. Understanding Heterogeneity and Permeability of Brain Metastases in Murine Models of HER2-Positive Breast Cancer Through Magnetic Resonance Imaging: Implications for Detection and Therapy. *Transl Oncol* 2015;8:176–84.
 20. Yoneda T, Williams PJ, Hiraga T, Niewolna M, Nishimura R. A bone-seeking clone exhibits different biological properties from the MDA-MB-231 parental human breast cancer cells and a brain-seeking clone in vivo and in vitro. *J Bone Miner Res* 2001;16:1486–95.
 21. Palmieri D, Bronder JL, Herring JM, Yoneda T, Weil RJ, Stark AM, *et al.* Her-2 overexpression increases the metastatic outgrowth of breast cancer cells in the brain. *Cancer Res* 2007;67:4190–8.
 22. Jensen MD, Hrinivich WT, Jung JA, Holdsworth DW, Drangova M, Chen J, *et al.* Implementation and commissioning of an integrated micro-CT/RT system with computerized independent jaw collimation. *Med Phys* 2013;40:081706.
 23. Thind K, Jensen MD, Hegarty E, Chen AP, Lim H, Martinez-Santesteban F, *et al.* Mapping metabolic changes associated with early Radiation Induced Lung Injury post conformal radiotherapy using hyperpolarized ¹³C-pyruvate Magnetic Resonance Spectroscopic Imaging. *Radiother Oncol* 2014;110:317–22.
 24. Ford EC, Achanta P, Purger D, Armour M, Reyes J, Fong J, *et al.* Localized CT-Guided Irradiation Inhibits Neurogenesis in Specific Regions of the Adult Mouse Brain. *Radiat Res* 2011;175:774–83.

25. Wong J, Armour E, Kazanzides P, Iordachita I, Tryggestad E, Deng H, *et al.* High-resolution, small animal radiation research platform with x-ray tomographic guidance capabilities. *Int J Radiat Oncol Biol Phys* 2008;71:1591–9.
26. Clarkson R, Lindsay PE, Ansell S, Wilson G, Jelveh S, Hill RP, *et al.* Characterization of image quality and image-guidance performance of a preclinical microirradiator. *Med Phys* 2011;38:845.
27. Smart D, Garcia-Glaessner A, Palmieri D, Wong-Goodrich SJ, Kramp T, Gril B, *et al.* Analysis of radiation therapy in a model of triple-negative breast cancer brain metastasis. *Clin Exp Metastasis* 2015;32:717–27.
28. Taskar KS, Rudraraju V, Mittapalli RK, Samala R, Thorsheim HR, Lockman J, *et al.* Lapatinib distribution in HER2 overexpressing experimental brain metastases of breast cancer. *Pharm Res* 2012;29:770–81.
29. Morikawa A, Peereboom DM, Thorsheim HR, Samala R, Balyan R, Murphy CG, *et al.* Capecitabine and lapatinib uptake in surgically resected brain metastases from metastatic breast cancer patients: a prospective study. *Neuro Oncol* 2014:1–7.
30. Yuan H, Gaber MW, Boyd K, Wilson CM, Kiani MF, Merchant TE. Effects of fractionated radiation on the brain vasculature in a murine model: blood-brain barrier permeability, astrocyte proliferation, and ultrastructural changes. *Int J Radiat Oncol Biol Phys* 2006;66:860–6.
31. Bart J, Groen H, Hendrikse N, van der Graaf W, Vaalburg W, de Vries E. The blood-brain barrier and oncology: new insights into function and modulation. *Cancer Treat Rev* 2000;26:449–62.
32. Madajewicz S, Chowhan N, Tfayli A, Roque C, Meek A, Davis R, *et al.* Therapy for patients with high grade astrocytoma using intraarterial chemotherapy and radiation therapy. *Cancer* 2000;88:2350–6.

33. Stupp R, Hegi ME, Mason WP, van den Bent MJ, Taphoorn MJ, Janzer RC, *et al.* Effects of radiotherapy with concomitant and adjuvant temozolomide versus radiotherapy alone on survival in glioblastoma in a randomised phase III study: 5-year analysis of the EORTC-NCIC trial. *Lancet Oncol* 2009; 10:459-66.

Chapter 4

4 MRI surveillance of cancer cell fate in a brain metastasis model after early radiotherapy

Purpose: Incidence of brain metastasis due to breast cancer is increasing and prognosis is poor. It is thought that disseminated dormant cancer cells persist in metastatic organs and may evade treatments, thereby facilitating a mechanism for recurrence. Radiotherapy is used to treat brain metastases clinically, but assessment has been limited to macroscopic tumor volumes detectable by clinical imaging. Here, we use cellular MRI to understand the concurrent responses of metastases and non-proliferative or slowly-cycling cancer cells to radiotherapy. **Methods:** MRI cell tracking was used to investigate the impact of early cranial irradiation on the fate of individual iron-labeled cancer cells and outgrowth of breast cancer brain metastases in the human MDA-MB-231-BR-HER2 cell model. **Results:** Early whole brain radiotherapy significantly reduced the outgrowth of metastases from individual disseminated cancer cells in treated animals compared to controls. However, the numbers of non-proliferative iron-retaining cancer cells in the brain were not significantly different. **Conclusions:** Radiotherapy, when given early in cancer progression, is effective in preventing the outgrowth of solitary cancer cells to brain metastases. Future studies of the non-proliferative cancer cells' clonogenic potentials are warranted, as their persistence presence suggests that they may have evaded treatment.

4.1 Introduction

When a metastatic breast cancer cell arrives in a distant organ – commonly bone, liver, lung, or brain – it may (1) die, (2) proliferate to form a metastatic tumor, or (3) remain viable, but dormant [1,2]. The complex relationship between these fates and their interplay when responding to treatment is poorly understood. Apparently successful cancer treatment often does not fully eradicate the disease and recurrences can manifest several years, or even decades, after the patient was believed to be disease-free [3]. Late recurrence (years or decades) implies the presence of dormant cancer cells that hide

within the patient until some yet unknown trigger causes them to proliferate and form clinically relevant metastases.

Prophylactic cranial radiation (PCI) decreases the incidence of brain metastases in SCLC patients [4,5]. Brain metastasis is an emerging therapeutic challenge in HER2+ breast cancer as advances in systemic therapy have resulted in improved extra-cranial disease control. Here, we investigate the potential use of PCI for these patients, where likelihood of developing brain metastasis approaches 50%, even when women are responding to systemic treatment [6,7]. Since PCI has a number of dose-dependent risks and side effects, improved understanding of brain metastatic breast cancer and especially solitary cancer cell responses to PCI is needed to determine the potential efficacy of this treatment in breast cancer patients [4,8].

Cellular MRI provides a powerful tool for cancer cell tracking and investigating treatment responses. This technique facilitates detection of iron-labeled cancer cells after initial arrest in an organ and surveillance as they develop into metastatic tumors [9]. Furthermore, non-proliferative cancer cells can be tracked by virtue of their long-term retention of iron particles [9–11].

This study employed cellular MRI to evaluate the concurrent responses of cancer cells and resulting metastases to early radiation treatment in a brain metastatic model of breast cancer. We hypothesized that early radiotherapy would prevent the outgrowth of disseminated cancer cells thereby mitigating tumor burden but the number of non-proliferative cancer cells would not be affected. Herein we demonstrate that cell tracking techniques are critical for a complete understanding of treatment response.

4.2 Methods

4.2.1 Cell Culture

Human brain metastatic breast cancer cells (MDA-MB-231-BR-HER2), previously transduced with enhanced green fluorescent protein (eGFP), were a kind gift from Dr. Patricia Steeg's laboratory at the National Cancer Institute (Bethesda, MA, USA) [12].

Cells were grown in DMEM containing 10% FBS, 1% penicillin and streptomycin, and 0.375 mg/mL zeocin. Culture media and supplements were purchased from Thermo Fisher Scientific (Mississauga, ON). For tracking, cells were labeled with iron oxide nanoparticles (0.9 μm MPIO, 62% magnetite, labeled with Flash Red; Bangs Laboratory, Fishers, IN, USA) as previously described [9]. Cell viability was measured by trypan blue exclusion and was not significantly different from previous experiments using unlabeled cells. Perl's Prussian Blue (PPB) stained cells were analyzed to evaluate iron labeling efficiency. The cell line was tested for mycoplasma contamination using the MycoAlert Mycoplasma Detection Kit (Lonza, Rockland, ME, USA) and was found to be negative.

4.2.2 Animal Preparation

Female nude mice (nu/nu, aged 6-8 weeks from Charles River Laboratories, Wilmington, MA, USA) were housed in a barrier facility. Experiments were approved by the Animal Use Subcommittee of the University Council on Animal Care at the University of Western Ontario. Mice (n=17) were anesthetized with isoflurane and given an intracardiac injection of 175,000 iron-labeled cells suspended in 0.1mL of HBSS (day 0). Mice were euthanized by pentobarbital (Euthanyl) overdose after the final imaging session. Group 1 (n=2, one with cells injected and one without) was euthanized on day 0 for tissue analysis. Group 2 (n=6) was untreated and euthanized on day 32, which is the typical endpoint for this model due to deteriorating health. Group 3 (n=6) was treated with WBRT, as described below, and also euthanized on day 32. Interestingly, Group 3 mice still appeared healthy at the pre-determined endpoint; therefore, an additional group (Group 4, n=4) was added to this study. Group 4 received identical treatment to Group 3, but was not sacrificed until health complications were observed.

4.2.3 Radiotherapy

A radiation treatment plan of 20 Gy total dose in two 10 Gy fractions to the whole mouse brain was delivered on days 1 and 2 post cell injection using a custom micro-irradiation system with on-board image guidance previously developed by our group [13]. This dose fractionation schedule was chosen because it is the equivalent biological effective dose (BED) to tumor (assuming $\alpha/\beta=10$ Gy) of a typical 30Gy/10 clinical WBRT plan and is

feasible in the animal model with the micro-CT/RT system. Mice were anesthetized with isoflurane and aligned using set up lasers in the feet first prone position on the rodent couch for CT imaging. The skull was identified using on-board fluoroscopy and custom-built computerized collimators were positioned such that a 10x14 mm (Groups 1-3) or 20x14 mm (Group 4) field encompassed the brain and shielded the remainder of the mouse head and body. The whole brain was irradiated with two equal-weighted parallel-opposed beams for a cumulative dose of 10 Gy per fraction. Mean dose rate was 0.13 ± 0.01 Gy per minute. One mouse in Group 4 was only treated to 10 Gy in one fraction due to equipment problem on day 2.

4.2.4 Magnetic Resonance Imaging

MRI was performed using a 3.0 T GE MR750 clinical scanner (General Electric, Mississauga, ON, Canada), with a custom insertable gradient coil and a custom mouse head radiofrequency coil [14]. Isoflurane anesthesia was used during scans and temperature was maintained with warm saline bags. Images were acquired using bSSFP with the following parameters: spatial resolution = 100x100x200 μm , repetition time = 18 ms, echo time = 9 ms, flip angle = 35° , signal averages = 1, radiofrequency phase cycles = 8, scan time = 32 minutes. A subset of scans on day 32 and later used the following parameters for to optimize contrast for co-detection of voids and tumors: repetition time = 10 ms, echo time = 5 ms, averages = 2, scan time = 35 minutes. ZIP2 and ZIP512 upscaling were applied.

4.2.5 Data Analysis

Image analysis was performed using open-source OsiriX image software (version 3.9.2). Brain metastases were manually counted and segmented in each of the 176 image slices per mouse. The region-of-interest volume tool was used to calculate tumor volume. Signal voids were manually counted in 22 image slices distributed regularly over the image set. The fractional signal loss (FSL) was measured in a subset of voids persisting between day 0 and 32 in one treated and one untreated animal. FSL describes the amount of contrast in a region of signal void by signal intensity (SI) measurements (Equation 1) and can be related to the amount of iron per voxel [15].

$$\text{FSL} = \frac{\bar{S}I_{\text{brain}} - \bar{S}I_{\text{void}}}{\bar{S}I_{\text{brain}}} \quad (\text{Equation 1})$$

Statistical analysis was performed using GraphPad Prism version 6.0 software (GraphPad, San Diego, CA, USA). Two-way unpaired Student's t-tests were used to compare two groups at a single time point. Two-way repeated measures analysis of variance (ANOVA) with *post hoc* Sidak's multiple comparisons tests were used to compare two groups over multiple time points.

4.2.6 Histology and Immunohistochemistry

At endpoint, mice underwent perfusion fixation and brains were either paraffin-embedded or frozen. Brain sections were stained with hematoxylin and eosin (H&E) for morphology or PPB for iron. The presence of micro-metastases (not detected with MRI) was evaluated in 18-28 sections per irradiated mouse brain. Brain sections were imaged on an Axio Imager A1 microscope (Zeiss CANADA, Toronto, ON, Canada) with a Retiga EXi (QImaging Scientific Research Cameras, Surrey, BC, Canada) digital camera. GFP and Texas Red filters were applied as necessary for fluorescence microscopy. Whole brain histology images were acquired using the TISSUEscope 4000 (Huron Digital Pathology, Waterloo, ON, Canada).

4.3 Results

The mouse brain was imaged using bSSFP to co-detect both iron-retaining cancer cells (signal voids) and tumors (hyperintensities) over time. Figure 4.1A illustrates a representative *in vivo* image slice through the brain of a control mouse that did not receive cancer cells or treatment. Cancer cells readily took up MPIO and a labeling efficiency of nearly 100% was achieved without affecting viability (Figure 4.1B). After intracardiac injection (day 0) and initial arrest in the brain, approximately 1% of iron-labeled cancer cells were detected as regions of signal void (Figure 4.1C); this delivery is in agreement with other studies [9,16]. Regions of discrete signal void in MRI were correlated optically to areas of both GFP and Flash Red fluorescence for the first time,

indicating the presence of live, MPIO-labeled MDA-MB-231-BR-HER2 cells (Figure 4.1D-G).

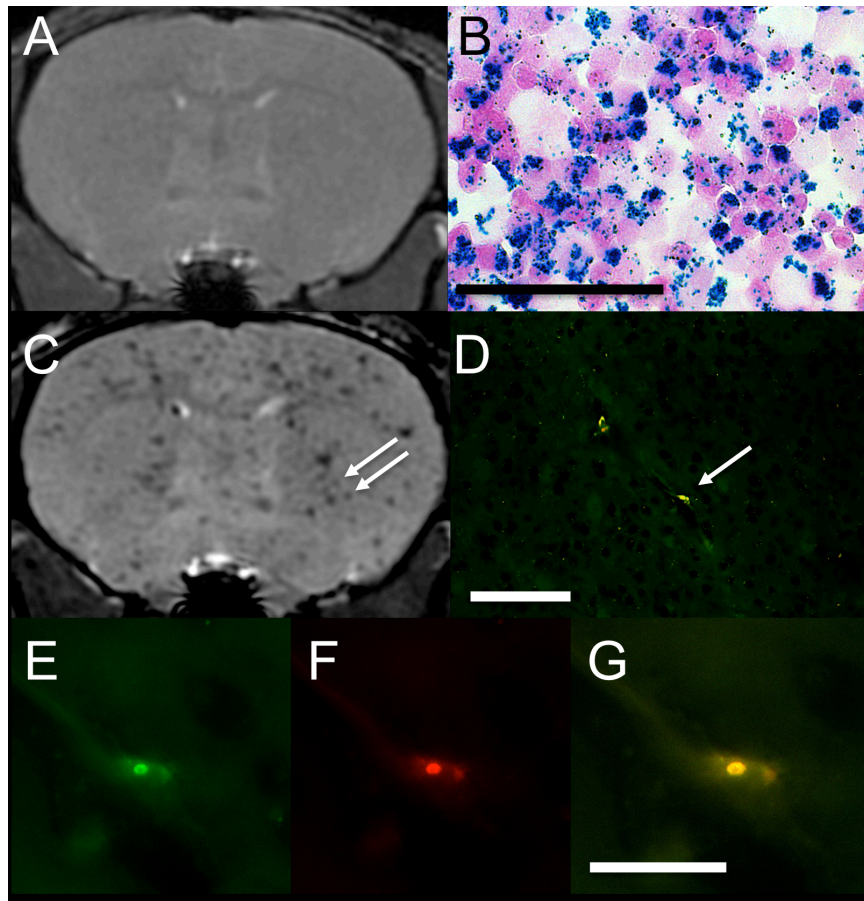


Figure 4.1: Visualization of iron-labeled cancer cell delivery with cellular MRI. bSSFP MRI illustrates the appearance of normal mouse brain prior to cell injection (A). *In vitro*, intracellular iron (blue, PPB) was detected within MDA-MB-231-BR-HER2 cells (pink, Nuclear Fast Red) labeled with MPIO (B). Successful delivery of iron-labeled cells to the brain was visualized as discrete regions of signal void in day 0 bSSFP MRI (C). Two signal voids detected on MRI (indicated by white arrows in C) were optically matched to regions that were both green and red fluorescent (D, co-localization appears yellow in the merged image). The green fluorescence results from the GFP⁺ cancer cells and the red fluorescence comes from the MPIO. The region indicated by the white arrow in D was viewed under 100x magnification (E-G) and validates that signal voids in MRI represent live, iron-labeled cancer cells. Data is from Group 1 mice euthanized on day 0. Scale bars are 100 μm (B, D) and 20 μm (E-G).

As cancer cells divide the iron label was diluted, thus rendering proliferative cancer cells undetectable over time. By day 32, tumors were detectable in bSSFP images as hyperintense regions due to the dominating effect of pathology-induced changes to local relaxation rates (Figure 4.2, white arrow). A subset of non-proliferative cancer cells retained the iron label and remained detectable long-term alongside metastases (Figure 4.2 top row, white arrowheads). Of particular interest is the observation that cancer cells, when treated with radiotherapy soon after arrest in the brain, rarely developed into tumors (Figure 4.2, bottom row). Of the few tumors that did form in WBRT-treated mice, all were found at the edge of the irradiation treatment field in the hindbrain. Furthermore, residual signal voids were consistently observed in the brain after early WBRT, despite prevention of the tumor burden (Figure 4.2 bottom row, white arrowheads).

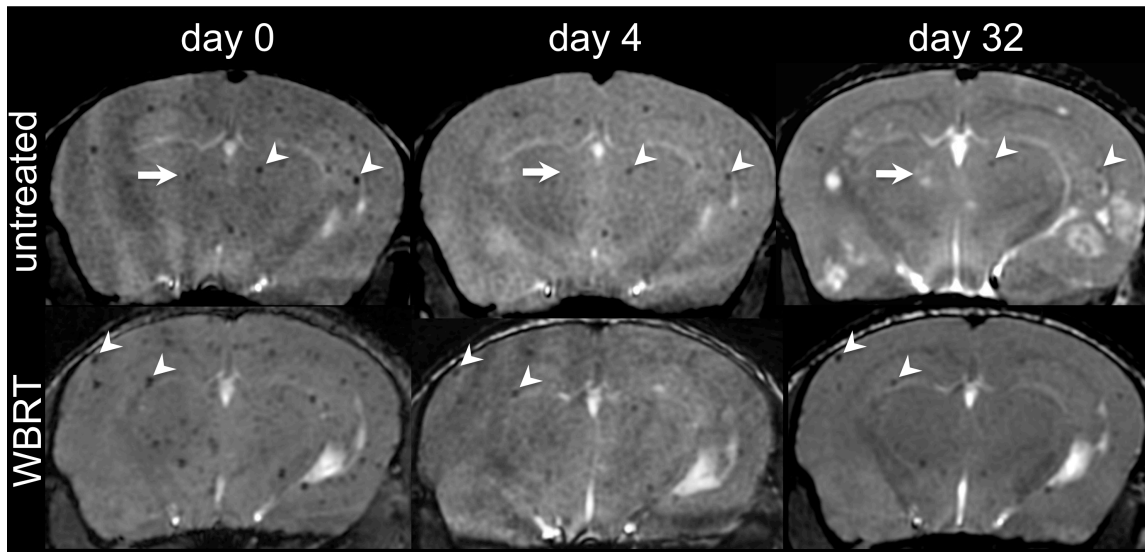


Figure 4.2: Monitoring cancer cell fate over time by dilution or retention of the iron oxide label. Balanced steady state free precession MR imaging can co-detect signal voids and developing tumors within the same mouse brain. The white arrow indicates a proliferative cancer cell. On day 0 it is present as a signal void; however the iron label is diluted as it proliferates and cannot be detected by day 4. On day 32 a tumor is visible in its place. Several other tumors are also visible in the brain and each arose from signal voids that were present in the same location on day 0 (note: the above figure displays single image slices only from a 3D image set and some visible tumors resulted from signal voids that were seen in neighboring slices on day 0). The white arrowheads indicate non-proliferative cells that retain their iron and remain as signal voids over time.

Representative image slices of mouse brain at endpoint (day 32) with corresponding whole brain H&E are shown in Figure 4.3. Metastases developed throughout the entire brain of untreated mice as seen in MRI and verified by histology (Figure 4.3, top rows). In comparison, MRI of treated mouse brain was largely free of macroscopic lesions. H&E stained brain sections from WBRT-treated mice were analyzed to determine if micro-metastases were present below the threshold for MRI detection and none were found (Figure 4.3, bottom rows). This suggests early WBRT was able to nearly eradicate all metastatic lesions throughout the whole mouse brain.

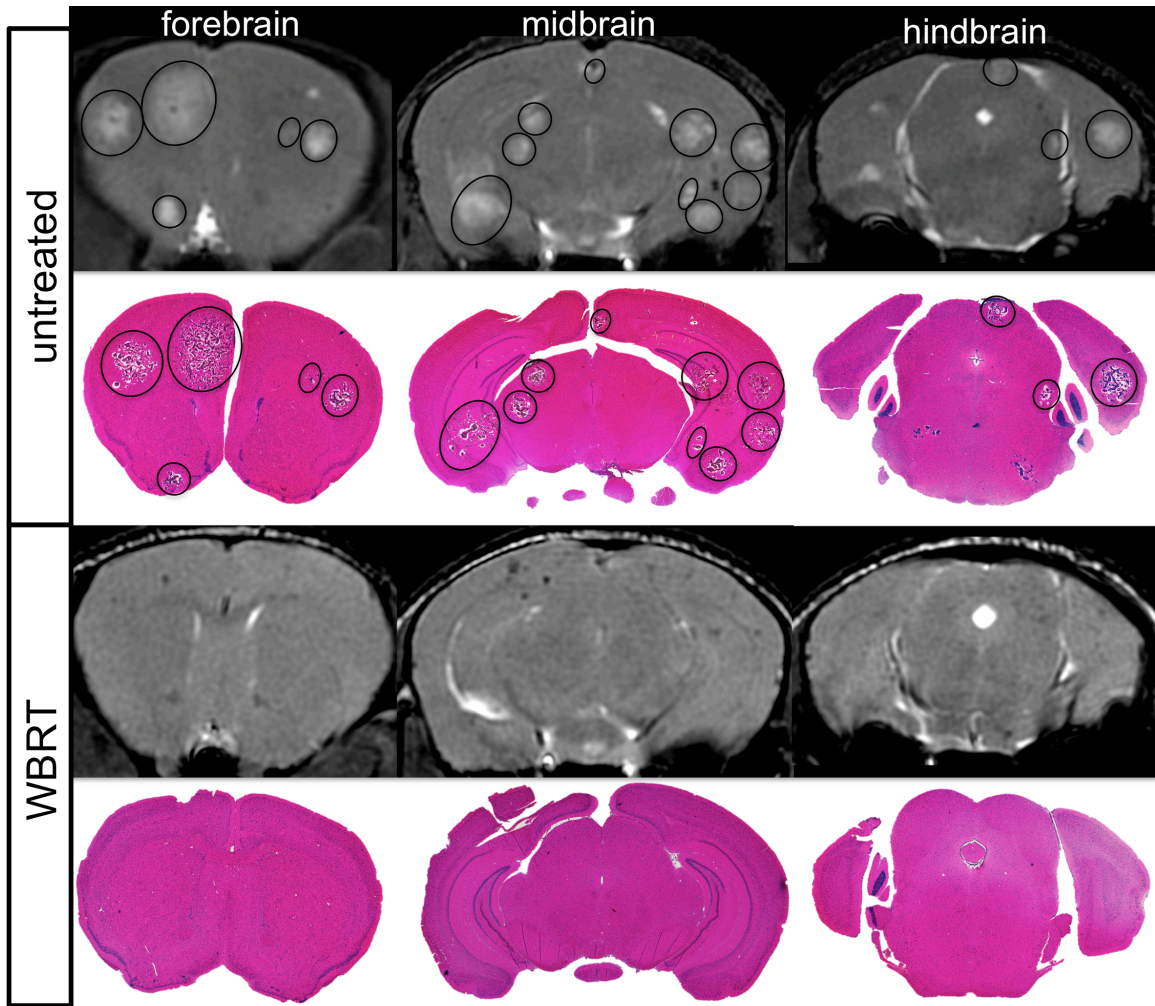


Figure 4.3: Representative images of forebrain, midbrain, and hindbrain at endpoint. bSSFP images with correlative histology are shown of an untreated mouse (top) and a mouse treated with early WBRT (bottom) at day 32 post cell injection. Metastases developed throughout the whole brain in untreated mice and are circled in black. Metastases were not detected in either MRI or histology for mice treated with early WBRT.

The number of metastases, total tumor volume and percentage of voids remaining were quantified in the whole mouse brain (Figure 4.4). On day 32, the number of metastases and the total MRI-detectable tumor volume in treated mice were significantly less than untreated ($p < 0.01$, $p < 0.05$) (Figure 4.4A,B). The percentage of signal voids, relative to day 0, remaining in the brain decreased over time in both groups, as expected ($p < 0.001$). However, there was no difference in the number of signal voids in WBRT treated versus untreated mice at either day 4 or day 32 ($p = \text{ns}$) (Figure 4.4C).

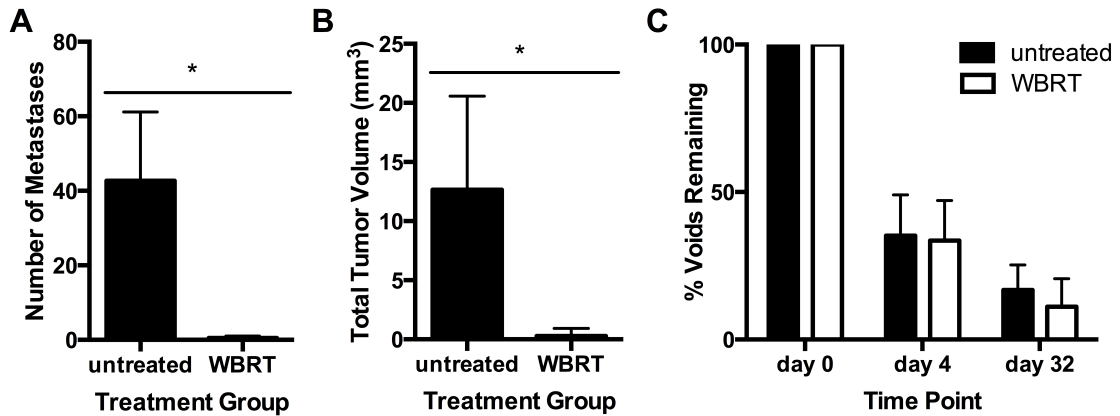


Figure 4.4: Early WBRT was able to prevent the growth of tumors. Both the number of tumors (A) and total tumor volume (B) were significantly less in treated mice compared to untreated mice by day 32. The number of signal voids in the brain decreased over time, but were not affected by treatment (C). Error bars represent standard deviation.

The FSL of signal voids is a surrogate measure for the amount of iron within cancer cells and was employed as an *in vivo* MRI indicator of the proliferative status of iron-labeled cancer cells within the void over time (Figure 4.5A,B). PPB staining for iron confirmed regions of signal void in MR images at endpoint corresponded to iron-positive cells (Figure 4.5C, image taken at 40x magnification). FSL did not change over time between day 0 and 32 ($p=ns$) and WBRT also had no effect on FSL ($p=ns$) (Figure 4.5D). A constant FSL suggests that iron content did not decrease within the cancer cells, as it would have if the cells were dividing; this indicates that the tracked voids represent non-proliferative cancer cells.

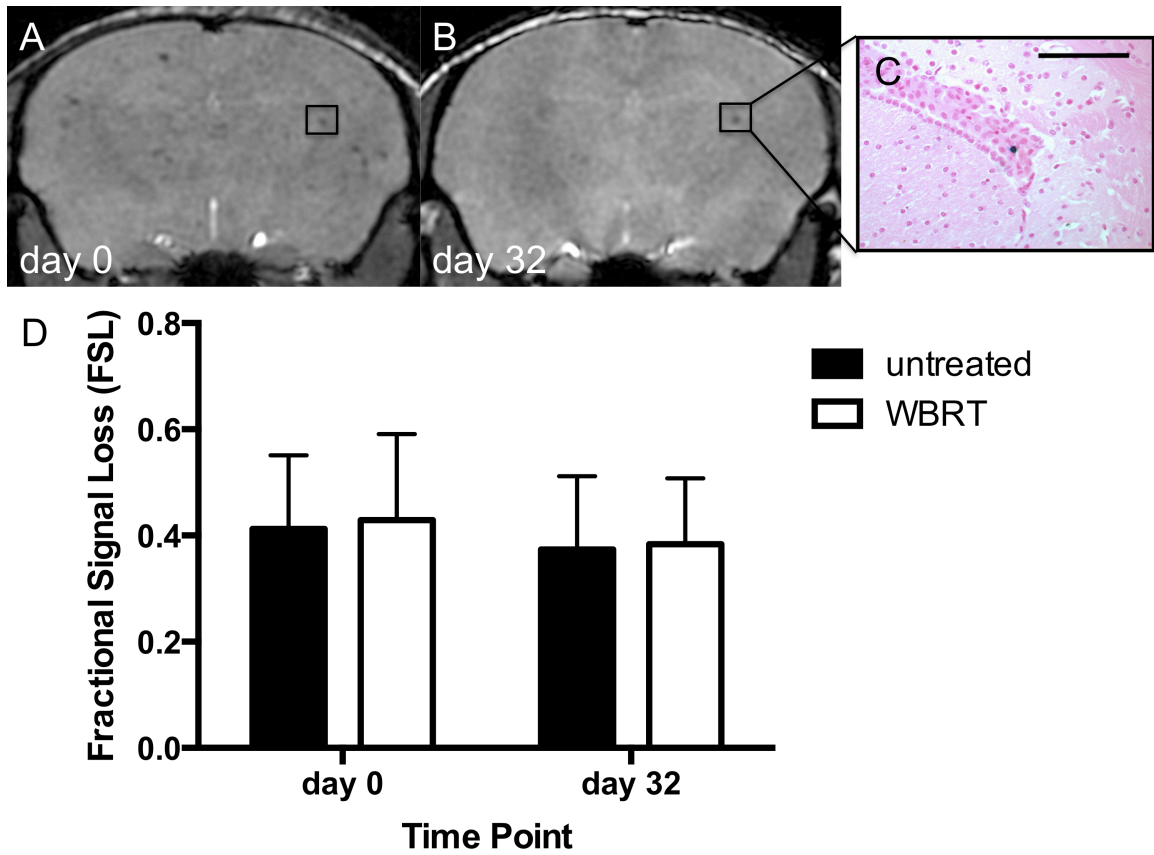


Figure 4.5: Signal void analysis suggests non-proliferative cancer cells persist after early WBRT. Representative MR images illustrate a region of signal void that persists from day 0 (A) to day 32 (B). PPB staining for iron presence indicated iron-containing cells in the mouse brain (blue) that corresponded to discrete regions of signal void (C). FSL of the signal void over time was measured using Equation 1 as an imaging marker for iron content within cancer cells. FSL did not change over time, or with treatment (D). This indicates that the iron content in the signal voids was not changing over time and supports our view that these voids represent non-proliferative cells that were able to persist in the brain after WBRT. Error bars represent standard deviation. Scale bar is 100 μ m.

An additional cohort treated with early WBRT was kept past the normal one-month endpoint for the MDA-MB-231-BR-HER2 model to determine the long-term fate of the observed non-proliferative cells. This proved challenging because the hematogenous delivery of cancer cells in this model led to extra-cranial relapse at later time points. Still, signal voids that were observed on day 32 remained as signal voids over time. Interestingly, one mouse that received half of the prescribed dose (first 10 Gy fraction only due to equipment failure on day 2) lived to day 100 without developing tumors in the brain (Figure 4.6).

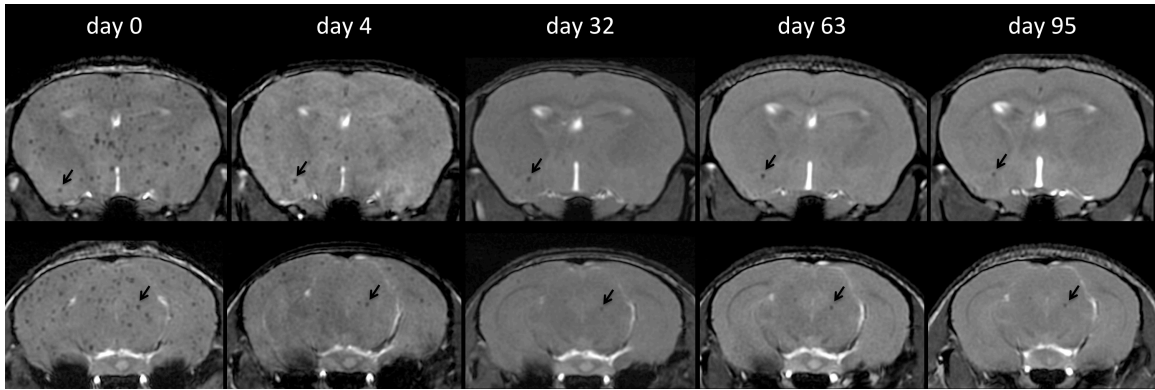


Figure 4.6: Long-term surveillance of outcome after early radiotherapy. Low dose (10 Gy in 1 fraction) whole brain irradiation was sufficient to prevent metastatic growth for over 100 days in the MDA-MB-231-BR-HER2 model. Black arrows indicate discrete signal voids that persisted from day 0 to day 95, indicating that non-proliferative cancer cells are still present.

4.4 Discussion

Overall, early WBRT was effective and prevented almost all tumor growth in the brain. Similarly, other groups have also found that metastatic tumor prevention is achievable with early treatment in SCLC or treatment with lapatinib in a brain metastasis model [4,5,17]. Considering these results, our preclinical study corroborates the suggestion that PCI may be a feasible metastasis prevention mechanism in patients with HER2+ breast cancer where the risk of brain metastasis is high [6,7]. Furthermore, the observation that a single 10 Gy dose prevented brain metastatic growth and extended survival three-fold suggests that lower than conventional WBRT irradiation doses may be effective for preventative treatment if delivered early enough in metastatic development when the disease is more sensitive to radiation.

Cellular MRI also illustrated the persistence of discrete signal voids due to iron-retaining cancer cells, alongside metastases, in the brain over time. This observation has previously been described in other metastasis models and is thought to represent a subpopulation of dormant cancer cells [9–11]. Importantly, no difference was observed in the number of voids between treatment groups at any time point. This demonstrates, for the first time, that irradiation does not alter the size of the non-proliferative cancer cell population.

These results suggest that non-proliferative cancer cells may be able to persist in the brain, even when radiotherapy is delivered early in metastatic progression and prevents initial tumor growth. This is in line with other preclinical studies that suggest quiescent cells are not responsive to cancer chemotherapies as they are designed to target proliferating cells [11]. While the mechanism of DNA damage delivery is different between radiotherapy and chemotherapy, the sub-population of non-proliferative cancer cells described here, if viable and if clonogenic, present a substantial therapeutic challenge. It is thought that some poorly understood trigger could prompt these cells to escape from dormancy and grow into clinically relevant metastases some time later. In women who have had breast cancer, recurrences can manifest years or even decades after the women are thought to be cured of cancer [3]. Further research is warranted to understand the disseminated dormant cell population and determine if these cells are able

to awaken and re-colonize the brain or other organs. To date, 're-awakening' of individual dormant cancer cells has not been directly observed *in vivo*; however, the MRI cell tracking technology described here offers a possible strategy to look for this phenomenon.

4.5 References

1. Chambers AF, Groom AC, MacDonald IC. Dissemination and growth of cancer cells in metastatic sites. *Nat Rev Cancer* 2002;2:563–72.
2. Goss PE, Chambers AF. Does tumour dormancy offer a therapeutic target? *Nat Rev Cancer* 2010;10:871–7.
3. Aguirre-Ghiso JA. Models, mechanisms and clinical evidence for cancer dormancy. *Nat Rev Cancer* 2007;7:834–46.
4. Auperin A, Arriagada R, Pignon J-P, Le Pechoux C, Gregor A, Stephens RJ, *et al.* Prophylactic cranial irradiation for patients with small-cell lung cancer in complete remission. *N Engl J Med* 1999;341:476–84.
5. Slotman B, Faivre-Finn C, Kramer G, Rankin E, Snee M, Hatton M, *et al.* Prophylactic cranial irradiation in extensive small-cell lung cancer. *N Engl J Med* 2007;357:664–72.
6. Lai R, Dang CT, Malkin MG, Abrey LE. The risk of central nervous system metastases after trastuzumab therapy in patients with breast carcinoma. *Cancer* 2004;101:810–6.
7. Clayton AJ, Danson S, Jolly S, Ryder WDJ, Burt PA, Stewart AL, *et al.* Incidence of cerebral metastases in patients treated with trastuzumab for metastatic breast cancer. *Br J Cancer* 2004;91:639–43.
8. Huang F, Alrefae M, Langleben A, Roberge D. Prophylactic Cranial Irradiation in Advanced Breast Cancer: A Case for Caution. *Int J Radiat Oncol* 2009;73:752–8.
9. Heyn C, Ronald JA, Ramadan SS, Snir JA, Barry AM, MacKenzie LT, *et al.* In vivo MRI of cancer cell fate at the single-cell level in a mouse model of breast cancer metastasis to the brain. *Magn Reson Med* 2006;56:1001–10.
10. Economopoulos V, Chen Y, McFadden C, Foster PJ. MRI Detection of

Nonproliferative Tumor Cells in Lymph Node Metastases Using Iron Oxide Particles in a Mouse Model of Breast Cancer. *Transl Oncol* 2013;6:347–54.

11. Townson JL, Ramadan SS, Simeanea C, Rutt BK, MacDonald IC, Foster PJ, *et al.* Three-dimensional imaging and quantification of both solitary cells and metastases in whole mouse liver by magnetic resonance imaging. *Cancer Res* 2009;69:8326–31.
12. Palmieri D, Bronder JL, Herring JM, Yoneda T, Weil RJ, Stark AM, *et al.* Her-2 overexpression increases the metastatic outgrowth of breast cancer cells in the brain. *Cancer Res* 2007;67:4190–8.
13. Jensen MD, Hrinivich WT, Jung JA, Holdsworth DW, Drangova M, Chen J, *et al.* Implementation and commissioning of an integrated micro-CT/RT system with computerized independent jaw collimation. *Med Phys* 2013;40:081706.
14. Ramadan SS, Heyn C, Mackenzie LT, Chambers AF, Rutt BK, Foster PJ. Ex-vivo cellular MRI with b-SSFP: quantitative benefits of 3T over 1.5T. *Magn Reson Mater Phys* 2008;21:251–9.
15. Heyn C, Bowen CV, Rutt BK, Foster PJ. Detection threshold of single SPIO-labeled cells with FIESTA. *Magn Reson Med* 2005;53:312–20.
16. Basse P, Hockland P, Heron I, Hokland M. Fate of Tumor Cells Injected Into Left Ventricle of Heart in BALB/c Mice: Role of Natural Killer Cells. *J Natl Cancer Inst* 1988;80:657–65.
17. Gril B, Palmieri D, Bronder JL, Herring JM, Vega-Valle E, Feigenbaum L, *et al.* Effect of lapatinib on the outgrowth of metastatic breast cancer cells to the brain. *J Natl Cancer Inst* 2008;100:1092–103.

Chapter 5

5 Summary and Future Work

This is the first characterization of tumor permeability using contrast-enhanced MRI in the SUM-190-BR3, JIMT-1-BR3, and MDA-MB-231-BR-HER2 models; further, it is the first investigation of the impact of radiotherapy on brain metastasis permeability *in vivo*. This is also the first study to prevent brain metastasis growth by giving early WBRT and the first to track cancer cells *in vivo* after radiation treatment.

5.1 Discussion and Conclusions

The brain is emerging as a sanctuary site for the growth of breast cancer metastasis. This thesis employed experimental imaging techniques to monitor brain metastatic tumor growth, BBB integrity, and cancer cell dormancy. In addition, a clinically relevant mouse whole brain radiation treatment plan was developed using novel micro-irradiation technology and used to investigate the impact of radiation treatment on metastases and disseminated cancer cells in the brain.

5.1.1 Chapter 2 – HER2+ Breast Cancer Brain Metastasis Models

In Chapter 2, three models of HER2+ breast cancer brain metastasis were characterized by high resolution anatomical and contrast-enhanced MRI with correlative histology and immunohistochemistry. We were the first to describe differences in tumor appearance, number, volume, and permeability across the models, despite each model representing HER2+ breast cancer. The main findings were:

1. Brain metastases in the SUM-190-BR3, JIMT-1-BR3, and MDA-MB-231-BR-HER2 models had different tumor morphology reflected by different MRI contrast in bSSFP images.
2. The duration of each model and the mean tumor volume at endpoint was significantly different in each model. The endpoints were day 28, 36, and 64 for the JIMT-1-BR3, MDA-MB-231-BR-HER2, and SUM-190-BR3

models respectively. Brain metastases in the MDA-MB-231-BR-HER2 model were significantly larger than tumors in the other two models.

3. The average fraction of Gd-permeable tumors was significantly different between models. All SUM-190-BR3 and most JIMT-1-BR-3 tumors took up contrast agent, whereas only 63.6% of tumors in the MDA-MB-231-BR-HER2 model displayed Gd-permeability.

These findings reflect substantial heterogeneity present in the disease and suggest several preclinical models may be required to adequately recapitulate human cancer development as well as to address possible differences in treatment response. Our goal for the following experiments was to investigate differences in BBB permeability after radiotherapy; therefore, based on these studies, we chose to use the MDA-MB-231-BR-HER2 model due to the higher proportion of impermeable tumors. Overall, understanding the heterogeneity present in the models, especially as it relates to tumor permeability, is important for improvements in brain metastasis detection and in general for systemic treatment delivery.

5.1.2 Chapter 3 – Brain Metastasis Response to Radiotherapy

In Chapter 3, we successfully implemented micro-irradiation technology that can deliver WBRT to mice and used this system to deliver radiation treatment in the MDA-MB-231-BR-HER2 murine model. We were the first to report that radiotherapy delivered after MRI-detectable tumors had developed in the brain could mitigate, but not eliminate, tumor growth and that radiation did not affect BBB permeability associated with tumors. The main findings were:

1. Fluoroscopy-guided collimation of the mouse brain allowed for precise delivery of 10 Gy per fraction WBRT. The treatment plan was designed using a Monte Carlo dose calculation and adequate whole brain coverage was confirmed by immunohistochemistry.

2. By 11 days post-WBRT, tumor volume was significantly less in treated mice compared to untreated mice; however, though smaller in volume, many metastases still remained in treated mice.
3. Over time, the fraction of Gd-permeable metastases increased in both groups. Radiotherapy did not change the fraction of metastases that were Gd-permeable at the time points studied (7 or 11 days post-treatment).

These findings indicate that WBRT of 20 Gy in 2 fractions was not curative in the MDA-MB-231-BR-HER2 model and suggest treatment should be delivered earlier in tumor progression for improved response. Moreover, this dose of radiotherapy was not sufficient to increase BBB permeability associated with tumors such that it could be used as a method to increase systemic drug uptake in brain metastasis.

5.1.3 Chapter 4 – Cell Tracking and Impact of Early Radiotherapy

In Chapter 4, we aimed to improve tumor control by delivering radiation treatment earlier in the MDA-MB-231-BR-HER2 model. We tested whether early radiotherapy could halt the transition to growth from disseminated solitary cancer cells and reduce tumor burden compared to treatment delivered after MRI-detectable metastasis; moreover, we investigated if early radiotherapy could alter the number of non-proliferative cancer cells that persist in the brain. We were the first to report that early WBRT significantly reduced metastatic tumor burden, though persisting non-proliferative cancer cells were observed. The main findings of this study were:

1. The number of brain metastases and the total MRI-detectable tumor volume was significantly less in treated mice compared to untreated. No additional micro-metastases were seen in histology of treated mice.
2. The percentage of signal voids relative to day 0 decreased over time in both groups and was not different between treated and untreated mice at any time point studied (day 0, 4, 32).

3. The FSL of voids persisting from day 0 to 32 was not significantly different between time points or between treatment groups.

These findings suggest early WBRT could be an effective preventative treatment by inhibiting the outgrowth of solitary cancer cells to brain metastasis in the MDA-MB-231-BR-HER2 model. Notably, cellular MRI revealed the persistence of non-proliferative iron-retaining cancer cells in the brain, which may represent a mechanism for recurrence if they are found to be viable and clonogenic.

5.2 Limitations

The experimental results presented in this thesis are based on observation in animal models that are intrinsically limited. First, the nude mouse (nu/nu) used in the brain metastasis models is immune-compromised; it lacks a thymus and is T-cell deficient [1]. The potential effects of host immunity on tumor growth, tumor permeability, cancer cell dormancy, and response to radiation were not fully accounted for due to the limited immune response in this animal. Regardless, the nude mouse is the strain of choice for these studies because it cannot reject the human cancer cell lines, yet it is resilient enough to withstand repeated removal from the barrier facility and exposure to the MRI and micro-CT suites. Secondly, the duration of the animal models is relatively short due to the many metastatic tumors that develop in the brain and CNS. This forces hypofractionation of radiotherapy treatment plans and limits the potential for dormant cancer cells to re-awaken. The timeline may be extended by injecting fewer cells, different cell lines with slower growth *in vivo*, or by employing intra-arterial injections to reduce extra-cranial tumor growth [2, 3]. Accordingly, the conclusions in this thesis should be interpreted within the context of preclinical models of HER2+ breast cancer metastasis to the brain; specifically, Chapter 2 investigates the SUM-190-BR3, JIMT-1-BR3, and MDA-MB-231-BR-HER2 models and Chapter 3 and 4 are limited to MDA-MB-231-BR-HER2 only.

The analysis of tumor permeability was qualitative in nature and was constrained to the extravasation of Gd-based contrast agent at endpoint (Chapter 2) or two time points post-

radiotherapy (Chapter 3). DCE-MRI could be employed for a quantitative assessment of vascular permeability and tumor perfusion, which may be more sensitive to changes in tumor permeability than contrast-enhanced T1-weighted images alone [4]. Gd was selected as a contrast agent for these studies because it allowed for investigation of BBB integrity *in vivo*. The use of additional contrast agents, with different sizes and compositions, may more fully characterize the extent of BBB disruption [5]. Moreover, imaging at additional time points, though expensive, may provide insight into the dynamic nature of BBB permeability during metastatic tumor growth.

MRI cell tracking of cancer cells with iron oxide nanoparticles is limited by its inability to discern cell viability, potential for bystander labeling, and challenges regarding cell quantification. It is impossible to know with certainty that the signal voids observed in Chapter 4 represent live dormant cancer cells. Validation of imaging data is relatively straightforward with PPB staining or fluorescence microscopy at early time points when there are many iron-labeled cells; however, it is extremely challenging at late time points when dormant cells are a rare cell population. We believe at least some of the signal voids discussed in Chapter 4 are live dormant cancer cells based on previous work by Heyn and colleagues who also described a subpopulation of iron-labeled non-proliferative cancer cells in the brain, as well as results presented by Magnitsky and colleagues who found iron-labeled cancer cells alongside some bystander labeled macrophages *in vivo* [6, 7]. In addition, our lab recently demonstrated the ability to recover cells that are both iron-positive GFP-positive - indicating iron-labeled cancer cells - from the mouse brain, as characterized by flow cytometry (*in press, Hamilton et al. Tomography*). Moreover, in our experience, dead cells and iron-labeled immune cells tend to move within an organ and clear over time. Future work aimed at recovering dormant cancer cells would be valuable. Complimentary strategies to determine viability would also be useful and are further discussed in “Future Work.” Finally, accounting for cell and tumor burden is challenging using cellular MRI because cell quantification within a signal void is not possible and micro-metastatic burden is not detected in bSSFP images at 100x100x200 μm resolution. In this thesis, the number of signal voids was manually quantified as a surrogate measure for solitary cancer cells and micro-metastases

were evaluated in histology. A semi-automated approach for void quantification, such as percent black pixels or signal void volume, would be more efficient and is in development. Fluorine-19 is an alternative imaging agent for quantitative cell tracking that may be more accurate than iron-labeled techniques; however it does not have sufficient sensitivity for single cell detection [8]. Higher resolution bSSFP imaging would visualize smaller tumors, but is not desirable for our purposes due to the increased scan time and cost.

5.3 Future Work

Future work will translate the bSSFP tumor imaging technique used in our preclinical experiments from mouse to human brain imaging in the clinic. In addition, future research that expands on tracking and characterizing non-proliferative cancer cells after treatment would provide invaluable insight into cancer dormancy.

5.3.1 Clinical Translation of bSSFP for Tumor Detection

The preclinical results described in Chapters 2 and 3 demonstrate that contrast-enhanced MRI underestimates brain metastatic burden in mice due to heterogeneity in BBB integrity associated with tumors. This finding, along with previous research by Percy *et al.* suggests bSSFP MRI is advantageous for detecting small, Gd-impermeable tumors; moreover, this method can often detect tumors before they become visible in contrast-enhanced MRI [9]. Importantly, it has not yet been studied if this result is consistent in humans and further investigation of this imaging technique in patients is warranted. Our group recently translated the preclinical bSSFP imaging technique to a small clinical study to evaluate the utility of bSSFP imaging for visualizing additional Gd-impermeable tumors in brain metastatic breast cancer patients. Future work could explore the relationship between tumor contrast in bSSFP images and cancer subtype or histopathological features. Radiomic analysis may also be useful to quantify brain metastasis features in bSSFP and other clinically relevant sequences (T1 pre- and post-Gd, T2), which could be used to predict patient outcomes and treatment response.

5.3.2 Bioluminescence Imaging

Bioluminescence imaging (BLI) may be useful as a complementary imaging technique to provide information about cell viability in future experiments, since cellular MRI is unable to differentiate between live and dead iron-labeled cells. This imaging modality detects visible light that is emitted during luciferase-mediated oxidation of a luciferin substrate and requires ATP as a co-factor; therefore, it can be inferred that all detected light must have been produced from live cells [10]. Engineering the MDA-MB-231-BR-HER2 cell line with a BLI reporter, such as firefly luciferase, would allow for quantitative BLI imaging of viable cancer cell burden in parallel with MRI-based cell tracking and concurrent tumor imaging. Characterization of the new luc⁺ cell line would be required to confirm that its proliferation, metastatic efficiency, and non-proliferative cell population is not significantly different from the luc⁻ cell line studied in this thesis. Experiments should be performed to develop an optimal BLI protocol for brain metastasis imaging and confirm that labeling cells with iron oxide nanoparticles will not affect detection or quantification of brain tumor burden using BLI. It would also be interesting to explore the detection threshold for disseminated luc⁺ iron-labeled cells in the mouse brain with the ultimate goal of discerning whether residual voids observed in the brain after early radiotherapy are alive or not.

5.3.3 Ex Vivo Brain Metastasis Assay

Discerning if non-proliferative cancer cells are clonogenic is important to understand the potential for future tumor recurrence. The cellular MRI results presented in Chapter 4 suggest non-proliferative cancer cells persist for extended periods of time; however, the metastatic nature of the MDA-MB-231-BR-HER2 model hinders investigation of clonogenicity in the long-term because development of extra-cranial disease ultimately limits the duration of study in this model. Naumov and colleagues previously recovered dormant cancer cells from the mouse liver and found that they were proliferative *in vitro* [11]. This strategy has been unsuccessful thus far in the brain metastatic model because there are few dormant cancer cells to recover and rare cell populations are challenging to isolate and expand *in vitro*. An *ex vivo* brain metastasis assay would be useful to extend

observation of non-proliferative cells and could provide a mechanism for interventions that may prompt dormant cells to re-awaken. Mendoza and colleagues created such a model, the pulmonary metastasis assay (PuMA), for studying metastasis formation and treatment in the lung; it may be possible that this strategy could be adapted for brain [12]. Preliminary studies would require optimizing perfusion and culture media for brain tissue survival, in order to preserve the brain architecture *in vitro* for 3-4 weeks or more. Following this, pilot studies using mouse brain with seeded cancer cells would be required to confirm the brain slices can host metastatic growth *in vitro*. Depending on the cell engineering, this growth could be quantified by histopathology, fluorescence microscopy, or BLI. Ultimately, this *ex vivo* assay could be initiated to extend observation in any brain metastasis model when extracranial disease requires euthanization of the animal. In particular, excising the brain at necropsy and maintaining it in culture using this assay would facilitate prolonged observation of non-proliferative cancer cells in the early radiotherapy model (Ch. 4). The increased study time may provide an opportunity for the non-proliferative cells to ‘re-awaken’ naturally or with growth supplements in order to determine their clonogenic potential.

5.4 References

1. Charles River Laboratories, Inc. Oncology Animal Models, 2011. Accessed from: http://www.criver.com/files/pdfs/rms/rm_rm_d_oncology_models.aspx
2. Perera M, Ribot EJ, Percy DB, McFadden C, Simeadra C, Palmieri D, *et al.* In Vivo Magnetic Resonance Imaging for Investigating the Development and Distribution of Experimental Brain Metastases due to Breast Cancer. *Transl Oncol* 2012;5:217–25.
3. Schackert G, Price J, Bucana C, Fidler I. Unique patterns of brain metastasis produced by different human carcinomas in athymic nude mice. *Int J Cancer* 1989;44:892–7.
4. Budde MD, Gold E, Jordan EK, Frank J a. Differential microstructure and physiology of brain and bone metastases in a rat breast cancer model by diffusion and dynamic contrast enhanced MRI. *Clin Exp Metastasis* 2012;29:51–62.
5. Sorensen A. Science to Practice: Blood-Brain Barrier Leakage—One Size Does Not Fit All. *Radiology* 2010;257:303–4.
6. Heyn C, Ronald JA, Ramadan SS, Snir JA, Barry AM, MacKenzie LT, *et al.* In vivo MRI of cancer cell fate at the single-cell level in a mouse model of breast cancer metastasis to the brain. *Magn Reson Med* 2006;56:1001–10.
7. Magnitsky S, Roesch A, Herlyn M, Glickson JD. In Vivo and Ex Vivo MR Imaging of Slowly Cycling Melanoma Cells. *Magn Reson Med* 2011;1373:1362–73.
8. Gaudet JM, Ribot EJ, Chen Y, Gilbert KM, Foster PJ. Tracking the Fate of Stem Cell Implants with Fluorine-19 MRI. *PLoS One* 2015;10:e0118544.
9. Percy DB, Ribot EJ, Chen Y, McFadden C, Simeadrea C, Steeg PS, *et al.* In vivo characterization of changing blood-tumor barrier permeability in a mouse model

of breast cancer metastasis: a complementary magnetic resonance imaging approach. *Invest Radiol* 2011;46:718–25.

10. Kemper EM, Leenders W, Kusters B, Lyons S, Buckle T, Heerschap A, *et al.* Development of luciferase tagged brain tumour models in mice for chemotherapy intervention studies. *Eur J Cancer* 2006;42:3294–303.
11. Naumov GN, Macdonald IC, Weinmeister PM, Kerkvliet N, Nadkarni K V, Wilson SM, *et al.* Persistence of Solitary Mammary Carcinoma Cells in a Secondary Site: A Possible Contributor to Dormancy. *Cancer Res* 2002; 62:2162–8.
12. Mendoza A, Hong S, Osborne T, Khan MA, Campbell K, Briggs J, *et al.* Modeling metastasis biology and therapy in real time in the mouse lung. *J Clin Invest* 2010;120:2979–88

Appendices

Appendix A: Permissions

Dear Donna,

As an Elsevier journal author, you retain various rights including Inclusion of the article in a thesis or dissertation whether in part or *in toto*; see <http://www.elsevier.com/about/company-information/policies/copyright#Author%20rights> for more information. As this is a retained right, no written permission is necessary provided that proper acknowledgement is given.

This extends to the online version of your thesis and would include any version of the article including the final published version provided that it is not available as an individual download but only embedded within the thesis itself.

If the article would be available as an individual download, only the preprint or (subject to the journal-specific embargo date) Accepted Author Manuscript version, but not the final published version, may be made available; see <http://www.elsevier.com/journal-authors/sharing-your-article> for more information. For more information regarding embargo dates, please see: http://www.elsevier.com/_data/assets/pdf_file/0018/121293/external-embargo-list.pdf.

If I may be of further assistance, please let me know.

Best of luck with your PhD thesis and best regards,

Laura

Laura Stingelin
Permissions Helpdesk Associate
Elsevier



01_03

PERMISSION LETTER

May 5, 2016

Springer reference**Journal of Molecular Medicine**

January 2014, Volume 92, Issue 1, pp 5-12

First online: 05 December 2013

Brain metastases from breast cancer: lessons from experimental magnetic resonance imaging studies and clinical implications

© Springer-Verlag Berlin Heidelberg 2013

Donna H. Murrell, Paula J. Foster, Ann F. Chambers

DOI 10.1007/s00109-013-1108-z

Print ISSN 0946-2716

Online ISSN 1432-1440

Journal number: 00109

Material to be used: Full text**Your project****Requestor:** Donna Murrell**University:** University of Western Ontario**Purpose:** Dissertation/Thesis

With reference to your request to reuse material in which Springer controls the copyright, our permission is granted free of charge under the following conditions:

Springer material

- represents original material which does not carry references to other sources (if material in question refers with a credit to another source, authorization from that source is required as well);
- requires full credit (Springer book/journal title, chapter/article title, volume, year of publication, page, name(s) of author(s), original copyright notice) to the publication in which the material was originally published by adding: "With permission of Springer";
- may not be altered in any manner. Abbreviations, additions, deletions and/or any other alterations shall be made only with prior written authorization of the author;
- **Springer does not supply original artwork or content.**

This permission

- is non-exclusive;
- is valid for one-time use only for the purpose of defending your thesis and with a maximum of 100 extra copies in paper. If the thesis is going to be published, permission needs to be reobtained.
- includes use in an electronic form, provided it is an author-created version of the thesis on his/her own website and his/her university's repository, including UMI (according to the definition on the Sherpa website: <http://www.sherpa.ac.uk/romeo/>);
- is subject to courtesy information to the co-author or corresponding author;
- is personal to you and may not be sublicensed, assigned, or transferred by you to any other person without Springer's written permission;
- is only valid if no personal rights, trademarks, or competitive products are infringed.

This license is valid only when the conditions noted above are met.



Dear Donna Murrell

We hereby grant you permission to reproduce the material detailed below at no charge **in your thesis, in print and on UWO library** and subject to the following conditions:

1. If any part of the material to be used (for example, figures) has appeared in our publication with credit or acknowledgement to another source, permission must also be sought from that source. If such permission is not obtained then that material may not be included in your publication/copies.
2. Suitable acknowledgment to the source must be made, either as a footnote or in a reference list at the end of your publication, as follows:

“This article was published in Publication title, Vol number, Author(s), Title of article, Page Nos, Copyright Elsevier (or appropriate Society name) (Year).”
3. Your thesis may be submitted to your institution in either print or electronic form.
4. Reproduction of this material is confined to the purpose for which permission is hereby given.
5. This permission is granted for non-exclusive world **English** rights only. For other languages please reapply separately for each one required. Permission excludes use in an electronic form other than as specified above. Should you have a specific electronic project in mind please reapply for permission.
6. This includes permission for the Library and Archives of Canada to supply single copies, on demand, of the complete thesis. This includes permission for UMI to supply single copies, on demand, of the complete thesis. Should your thesis be published commercially, please reapply for permission.

Type of Publication: Book

Book Title: Introduction to Cancer Metastasis, 1st edition

Book ISBN: N/A

Book Author: edited by Aamir Ahmad, chapter authors are DH Murrell, F Perera, AF Chambers, and PJ Foster

Book Year: N/A

Book Pages: N/A to N/A

Book Chapter number: 19: Brain Metastatic Cancers

Book Chapter title: Brain metastasis: basic biology, clinical management, and insight from experimental model systems

I would like to use: Full article/chapter

Quantity of material:

Excerpts:

Are you the author of the Elsevier material? Yes

If not, is the Elsevier author involved? Yes

If yes, please provide details of how the Elsevier author is involved: I am first author of this work.

In what format will you use the material? Print and Electronic

Will you be translating the material? No

If yes, specify language:

Information about proposed use: Reuse in a thesis/dissertation

Proposed use text: -thesis available in full text online through UWO library -Library and

From: Todd Hanson
Subject: RE: request for permission to use material in doctoral thesis
Date: June 10, 2016 at 2:00 PM
To: Donna Murrell

Yes, you have our permission as outlined below. Good luck.

Todd Hanson
Editor
Medical Physics Publishing, Inc.

-----Original Message-----

From: Donna Murrell
Sent: Friday, June 10, 2016 8:29 AM
To:
Subject: request for permission to use material in doctoral thesis

Good morning,

I am a University of Western Ontario graduate student completing my doctoral thesis and I am the second author for an upcoming chapter in the Advances in Medical Physics textbook. I wrote a subsection entitled "Magnetic Resonance Imaging" in the chapter "Small Animal Radiotherapy and Imaging" (Senior author is Eugene Wong).

I was wondering if I may please have permission to allow inclusion of this work in my thesis? I will only use excerpts from the subsection that I wrote and the material would be attributed to the book chapter in press through a citation.

Thank you for your time,
Donna

Donna Murrell
PhD candidate
Medical Biophysics
Western University

Appendix B: Animal Use Protocol



AUP Number: 2009-080

PI Name: Chambers, Ann

AUP Title: Non-invasive Imaging Of Metastasis: Detection, Monitoring And Intervention

Approval Date: 10/30/2013

Official Notice of Animal Use Subcommittee (AUS) Approval: Your new Animal Use Protocol (AUP) entitled "Non-invasive Imaging Of Metastasis: Detection, Monitoring And Intervention

" has been APPROVED by the Animal Use Subcommittee of the University Council on Animal Care. This approval, although valid for four years, and is subject to annual Protocol Renewal.2009-080::5

1. This AUP number must be indicated when ordering animals for this project.
2. Animals for other projects may not be ordered under this AUP number.
3. Purchases of animals other than through this system must be cleared through the ACVS office. Health certificates will be required.

The holder of this Animal Use Protocol is responsible to ensure that all associated safety components (biosafety, radiation safety, general laboratory safety) comply with institutional safety standards and have received all necessary approvals. Please consult directly with your institutional safety officers.

Submitted by: Copeman, Laura
on behalf of the Animal Use Subcommittee
University Council on Animal Care

Curriculum Vitae

Donna Helen Murrell

EDUCATION:

- 09/12 – 08/16 PhD Medical Biophysics (Molecular Imaging)
University of Western Ontario, London, Ontario, Canada
- 09/14 – 08/16 MSc Clinical Medical Biophysics (CAMPEP accredited)
University of Western Ontario, London, Ontario, Canada
- 09/07 – 04/12 BSc (Hons) Medical Physics and Medical Biophysics
University of Western Ontario, London, Ontario, Canada

SCHOLARSHIPS & AWARDS:

- 03/16 Cum Laude Abstract Award
Imaging Network of Ontario
- 03/16 CIHR-ICS Travel Award (\$1,000)
CIHR – Institute of Cancer Research
- 03/16 Travel Award (\$2,000)
Canadian Cancer Society
- 10/15 Expanding Horizons Travel Grant (\$1,000; declined)
American Association of Physicists in Medicine
- 04/15 Dr. Alfred Jay Medical Biophysics Award for Translational
Research (\$2,000)
Department of Medical Biophysics, Western University
- 01/15 Schulich Scholarship for Medical Research (\$2,000)
Schulich School of Medicine and Dentistry, Western University
- 09/14 – 08/17 Fellowship (\$35,000 per year)
Canadian Breast Cancer Foundation – Ontario Region
- 09/14 – 08/17 Western Graduate Research Scholarship (\$7,800 per year)
Department of Medical Biophysics, Western University
- 04/14 CIHR-ICS Travel Award (\$1,000)
CIHR – Institute of Cancer Research
- 09/13 Student Travel Stipend Award (\$650)

	World Molecular Imaging Congress – top rated abstract
09/13	Molecular Imaging Travel Award (\$500) Molecular Imaging Collaborative Graduate Program
09/12 – 08/16	CaRTT Scholar CIHR-STP Cancer Research and Technology Transfer (CaRTT) MSc award 09/12 – 08/14 (\$25,700 per year) PhD award 09/4 – 08/16 (no funding requested)
09/12 – 08/16	Translational Breast Cancer Studentship London Regional Cancer Program and the Breast Cancer Society of Canada MSc award 09/12 – 08/14 (\$17,000 per year) PhD award 09/14 – 08/16 (no funding requested)
09/12 – 08/14	Western Graduate Research Scholarship (\$4,500 per year) Department of Medical Biophysics, Western University

PEER REVIEWED JOURNAL ARTICLES:

1. Zarghami N, Murrell DH, Jensen MD, Dick FA, Chambers AF, Foster PJ, Wong E. “Evaluation of radiation-induced DNA double-stranded breaks and tumor response in a breast cancer brain metastasis model.” *Submitted to Radiation Oncology, June 14, 2016*. Ms. Ref. No. RAON-D-16-00281
2. Hamilton AM, Parkins KM, Murrell DH, Ronald JA, Foster PJ. “Investigating the Impact of a Primary Tumor on Metastasis and Dormancy Using MRI: New Insights into the Mechanism of Concomitant Tumor Resistance” *in press, Tomography, June 3, 2016*.
3. Makela AV*, Murrell DH*, Parkins KM, Kara J, Gaudet JM, Foster PJ. “Cellular Imaging with MRI” *Under review at Topics in Magnetic Resonance Imaging April 26, 2016* (* denotes co-first authors).
4. Murrell DH, Zarghami N, Jensen MD, Dickson F, Chambers AF, Wong E, Foster PJ. “MRI surveillance of cancer cell fate in a brain metastasis model after early radiotherapy” *Under review at Magnetic Resonance in Medicine, July 5, 2016*. Ms. Ref. No. MRM-16-17144
5. Murrell DH, Zarghami N, Jensen MD, Chambers AF, Wong E, Foster PJ (2016) “Evaluating changes to blood-brain barrier integrity in brain metastasis over time and after radiation treatment,” *Translational Oncology* 9(3): 219-227.
6. Haedicke IE, Li T, Martinez F, Hamilton AM, Murrell DH, Nofiele J, Ling H, Cheng M, Scholl T, Foster PJ, Zhang X (2016) “An Enzyme Activatable and Cell Permeable

- Mn^{III}-Porphyrin as a Highly Efficient T₁ MRI Contrast Agent for Cell Labeling”
Chemical Science 7:4308-17.
7. Murrell DH, Hamilton AM, Mallett CL, van Gorkum R, Chambers AF, Foster PJ (2015) "Understanding Heterogeneity and Permeability of Brain Metastases in Murine Models of HER2-positive Breast Cancer through Magnetic Resonance Imaging: Implications for Detection and Therapy," *Translational Oncology* 8(3): 176-184.
 8. Murrell DH, Foster PJ, Chambers AF (2014) "Brain Metastases from Breast Cancer: Lessons from Experimental Magnetic Resonance Imaging Studies and Clinical Implications," *Journal of Molecular Medicine* 92(1): 5-12.
 9. Murrell, Donna and Dragunas, Andrew (2013) "A Comparison of Two Swimming Start Techniques from the Omega OSB11 Starting Block," *WURJ: Health and Natural Sciences*: Vol.3: Iss.1, Article 1.

BOOK CHAPTERS:

1. Murrell DH, Perera F, Chambers AF, Foster PJ. "Brain metastasis: basic biology, clinical management, and insight from experimental model systems" in Introduction to Cancer Research, 1st ed, edited by Aamir Ahmad; *Elsevier, accepted April 1, 2016, scheduled for publication April 2017.*
2. Bazalova-Carter M, Murrell DH, Parkins K, Ronald J, Foster PJ, Graves E, Granton P, Wong E. "Small Animal Radiotherapy and Imaging" in Advances in Medical Physics, edited by Shiva Das and Jacob Van Dyk; *Medical Physics Publishing, in press March 17, 2016.*

PEER-REVIEWED PRESENTATIONS:

1. Murrell DH, Tay KY, Wong E, Chambers AF, Perera F, Foster PJ. Fast Imaging Employing Steady-State Acquisition of Brain Metastasis: from mouse to woman. *International Society for Magnetic Resonance in Medicine Annual Meeting 2016 in Singapore. Poster Presentation.*
2. Murrell DH, Zarghami N, Jensen MD, Chambers AF, Wong E, Foster PJ. Longitudinal MRI evaluation of whole brain radiotherapy on brain metastasis development and dormancy in a mouse model. *World Congress on Medical Physics and Biomedical Engineering 2015 in Toronto, ON, CAN. Oral Presentation.*
3. Murrell DH, Dickson F, Hamilton AM, Foster PJ. Iron Retention in Nonproliferative Cancer Cells Allows for Tracking by MRI: An In Vivo Assay for Studying Cancer Cell Dormancy. *International Society for Magnetic Resonance in Medicine Annual Meeting 2015 in Toronto, ON, CAN. Poster Presentation.*

4. Murrell DH, Gaudet J, Makela A, Foster PJ. Towards Balanced Steady State Free Precession Imaging for Breast Cancer Brain Metastasis. *International Society for Magnetic Resonance in Medicine: MR in Cancer Workshop 2014 in Austin, TX, USA*. **Poster Presentation.**
5. Murrell DH, van Gorkum R, Hamilton A, Mallett C, Gril B, Chambers A, Steeg P, Foster PJ. Understanding the Heterogeneity of Brain Metastases from Breast Cancer: Lessons from New Models and Experimental Magnetic Resonance Imaging. *International Society for Magnetic Resonance in Medicine Annual Meeting 2014 in Milan, Italy*. **E-poster Presentation.**
6. Murrell DH, Hamilton A, Jensen MD, Zarghami N, Chambers AF, Wong E, Foster PJ. In Vivo MRI Characterization of Tumour Response to Radiotherapy in a Mouse Model of Brain Metastasis. *Canadian Cancer Research Conference 2013 in Toronto, ON, CAN*. **Rated top abstract in category - Oral Presentation.**
7. Murrell DH, Hamilton A, Jensen M, Zarghami N, Chambers AF, Wong E, Foster PJ. MRI Characterization of the Responses of Brain Metastatic Breast Cancer Cells to Whole Brain Micro-irradiation in Mice. *World Molecular Imaging Congress 2013 in Savannah, GA, USA*. **Poster Presentation.**

WORK EXPERIENCE:

- | | |
|---------------|--|
| 09/15 – 04/16 | Teaching Assistant, BIOPHYS 9700
Department of Medical Biophysics, Western University |
| 09/15 – 12/15 | Linear Accelerator Quality Assurance Internship
London Regional Cancer Program, London, Ontario, Canada |
| 02/14 – 11/14 | Graduate Research Assistant
Robarts Research Institute, London, Ontario, Canada |